CHAPTER 1

Introduction

1.1 Light-Emitting Diodes

Light-emitting diodes (LEDs) are a typical *p-n* junction device used under a forward bias. The basic operating mechanisms are based on the electrical and optical properties of *p-n* junction and of semiconductor materials. Depending on the semiconductor material used in light emitting layer (active layer), the wavelength of the emitted light can be anywhere within the range from visible to infrared. Most commercially available LEDs are made from III-V compound semiconductors. Some II-VI compound semiconductors such as ZnS and ZnSe are used in a few LEDs emitting visible light, through these materials are not used frequently because of the difficulty of *p-n* junction formation. [1]

LEDs have been widely used in various kinds of equipments and systems. LEDs composed of a combination of InGaAsP and InP cover the wavelengths from the 1300 to 1550 nm band and are the ones usually used in optical fiber communication systems. A combination of GaAs and AlGaAs or a combination of different compositions of AlGaAs has been used to make LEDs emitting in the 780 to 900 nm band, and those LEDs have been used in optical fiber communication systems, data links, remote controllers, and so forth. For display and indicator applications, LEDs emitting from blue to red light are usually applied. [1]

LEDs could be considered the ultimate general source of continuous light due to its high luminescence efficiency, quick response time, and long lifetime. Much research has been done on high brightness LEDs. Currently the AlInGaP system is employed for yellow, red, and orange LEDs, with efficiency superior to unfiltered incandescent lamps. [2] Typical visible

LEDs now have efficiencies above 10 lumens W^{-1}, extremely good lifetimes (>5 years), rapid response times. This makes them the light source of choice for applications ranging from color outdoor displays and signs, interior automotive lighting, exterior running lights on trucks and traffic lights.

The availability of the primary colors raises the possibility of white light sources. There are two basic options: the first is color conversion through use of a phosphor or organic dye inside the package to convert the blue light from a GaN LED into white light. The second method would be color mixing through integration of red, blue, and green LEDs in the same package. Nichia produced white light LED products based on combining a blue GaN LED with an yttrium-aluminum-garnet (YAG) fluorescent layer. The efficiency of this approach is less than that of the color-mixing technique since the phosphor efficiency is less than 100 %, but it has substantial savings in terms of cost. There is also a program underway to develop this technology for fluorescent tubes for lighting applications, because of the much longer lifetime and reduced energy consumption relative to incandescent and conventional fluorescent lamps. The energy savings and cost efficiency of LEDs relative to tungsten filament incandescent lamps has been the main impetus behind their success.

In fact, the only significant problem which previously prevented the widespread application of colored LEDs has been the lack of high intensity blue and green LEDs. As blue is one of the three primary colors (red, green and blue) LEDs are required to reproduce the full color spectrum and achieve pure white light. If high brightness blue and green LEDs were available, white LED lamps with high reliability and low energy consumption could be used for many kinds of lights sources by mixing the three primary color LEDs instead of conventional light bulbs or fluorescent lamps.

1.2 III-V Nitride Based LEDs

Much research has been done on high brightness blue LEDs for use in full color displays, full color indications and light sources for lamps with the characteristics of high efficiency, high reliability and high speed. For these purposes, II-VI materials such as ZnSe [3], SiC [4] and III-V nitride semiconductions such as GaN [5] have been investigated intensively for a long time. However, it was impossible to obtain high brightness blue LEDs with a brightness over 1 cd. The short lifetimes prevent II-VI based devices from commercialization at present. It is generally thought that the short lifetime of these II-VI baesd devices is caused by crystal defects with a density of 10^5 cm^{-2}. One crystal defect causes the propagation of other defects leading to failure of the devices. SiC is another wide bandgap material for blue LEDs. The brightness of SiC blue LEDs is only between 10 mcd and 20 mcd because of the indirect bandgap of this material. Despite of this poor performance, 6H-SiC blue LEDs have been commercialized for a long time because there have been no blue light emitting devices without SiC LEDs. [6] GaN and related materials such as AlGaInN are III-V nitride compound semiconductors with the wurtzite crystal structure and the energy band structures of direct interband transition, which is suitable for light emitting devices.

Figure 1-1 shows the bandgap energy of various materials as a function of the lattice constant. Conventionally, AlGaAs material has been used for high brightness red LEDs and infrared laser diodes (LDs). The lattice constant of AlGaAs almost equals to that of GaAs in whole compositions. Therefore, GaAs substrate is suitable for AlGaAs growth. AlInGaP material has been used for red, yellow and green LEDs and red LDs. This system is also lattice-matched with GaAs substrate when the composition of AlInGaP is adjusted. The bandgap energy of AlGaInN varies between 6.2 and 1.95 eV depending on its composition at room temperature, as shown in Fig. 1-1. Therefore, these III-V nitride semiconductors are useful for light emitting devices especially in the short wavelength region. Among AlGaInN system, GaN has been most intensively studied. GaN has a bandgap energy of 3.4 eV at room temperature. Previous research on III-V nitrides has paved the way for the realization of high

quality crystals of GaN, AlGaN and InGaN, and of *p*-type conduction in GaN and AlGaN. [7, 8] The mechanism of the acceptor compensation that prevents obtaining low resistivity *p*-type GaN and AlGaN has been elucidated. [9-12] In Mg-doped *p*-type GaN, Mg acceptors are deactivated by atomic hydrogen that is produced from NH_3 gas used for N source during GaN growth. High brightness blue LEDs have been fabricated on the basis of these results, and luminous intensities over 1 cd have been achieved. [13, 14] These LEDs are now commercially available. Also, high brightness single quantum well (SQW) blue, green and yellow InGaN LEDs with a luminous intensity above 10 cd for green LEDs have been achieved and commercialized. [15-17] By combining these high power and high brightness blue InGaN SQW LED, green InGaN SQW LED and red AlGaAs LED, many kinds of applications, such as LED full color displays and LED white lamps for use in place of light bulbs or fluorescent lamps, are now possible with characteristics of high reliability, high durability and low energy consumption.

Figure 1-2 shows a chromaticity diagram where blue InGaN/AlGaN LEDs and blue-green InGaN/AlGaN are shown. [18, 19] Commercially available green GaP LEDs and red AlGaAs LEDs are also shown. From this figure, only blue-green InGaN/AlGaN LEDs are within the applicable regions for roadway signals and railway signals. Therefore, InGaN/AlGaN LEDs blue-green LEDs can be used for those applications from the viewpoint of color. Fig. 1-3 is a chromaticity diagram in which blue and green InGaN SQW LEDs are shown. Commercially available green GaP LEDs, green AlInGaP LEDs and red AlGaAs LEDs are also shown. The color range of light emitted by a full color LED lamp in the chromaticity diagram is shown as region inside each triangle that is drawn by connecting the positions of three primary color LED lamps in the diagram. Three color range (triangles) are shown for differences only in green LEDs (green InGaN, green GaP and green AlInGaP LEDs). In this figure, the color range of lamps composed of three primary color LEDs, namely, a blue InGaN SQW LED, green InGaN SQW LED and red GaAlAs LED, it the

widest compared with other color ranges obtained using a different green LED, such as green GaP LED and green AlInGaP LED. This means that the InGaN blue and green SQW LEDs show much better color and color purity in comparison with other blue and green LEDs.

1.3 History of Gallium Nitride

Attempts to synthesize GaN were made by Juza and Hahn [20] in 1938. Small needles of GaN could be synthesized by passing ammonia over hot gallium. Grimmeiss *et al.* [21] used the same method and obtained small crystals of GaN in 1959. They measured the photoluminescence (PL) spectra of the small GaN crystals. Maruska and Tietjen [22] deposited the first large area GaN layers on sapphire in 1969. They used the chemical vapor deposition method. In all the early samples the concentration of electrons due to background doping was very large. Several centers were proposed that could give rise to background *n*-type conductivity. It was shown that a center consisting of a nitrogen vacancy surrounded by four gallium atoms could act as an efficient donor. [23] Residual impurities like oxygen and Si were also considered as possible donors. Many groups published papers supporting one model or the other. There is no consensus even today as to which centers give rise to large electron concentration in the as fabricated samples.

The availability of large area samples [22] gave impetus to GaN research. Pankove *et al.* [23, 24] were successful in fabricating the first blue GaN LED, as shown in Fig. 1-4. It was a metal/insulating GaN: Zn/*n*-GaN (*m*-*i*-*n* or MIS) diode. The *n*-GaN layers contained different concentrations of Zn. The wavelength of the emitted light depended on the Zn concentration. The wavelength could be blue-shifted by decreasing Zn concentration. Blue and green color could be easily obtained. An Mg-doped electroluminescent diodes emitting in the violet region was also fabricated. [25] Other important research of that period includes [26-38] study of negative electron affinity [26], surface acoustic wave generation [27], and solar blind UV

detectors. [23] Stimulated emission from small GaN crystals was first observed at 2 K in 1971 by Dingle *et al.*. [39] The difficulties in *p* doping and making good ohmic contacts persisted. Until the late 1970s the quality of GaN was not very good. The results of optical and electrical measurements were not reproducible. [40] This hampered the progress of research on the III-nitrides. A more detailed account of the early work is given in the reviews of Pankove [23] and Monemar. [40]

The beginning of the growth of good quality epilayers was made by Yoshida *et al.*. [28] They were the first to use the two-step method of growth. They showed in 1983 that if an AlN buffer layer is grown between the GaN film and the sapphire substrate, the quality of the layers improves. The two-step method was investigated and perfected by Akasaki, Amano and co-workers in 1988/1989. [29, 30] In the first step a thin buffer layer of AlN is grown on the sapphire substrate at a low temperature of ~500 °C. The GaN layer is grown on the buffer layer. The temperature at which the GaN layer is grown is much higher.

The two-step method is described in detail later in this article. Amano *et al.* [29] were also the first to obtain *p*-type conductivity in GaN. As grown Mg-doped GaN layers have a very high resistance. Amano *et al.* [29] were interested in studying cathodoluminescence (CL) of Mg-doped GaN. They observed that electron irradiation has two effects on the behavior of GaN: Mg. First, it increases the efficiency of the luminescence by up to 2 orders of magnitude. Second, the sample becomes conducting and *p* type. Only the top part of the sample in which the electrons penetrate became conducting. This showed that the low energy electron beam irradiation (LEEBI) was responsible for the *p*-type conduction. Akasaki *et al.* [31] also showed that Mg is an acceptor with energy of activation equal to 160 meV. In 1992 van Vechten *et al.* [32] suggested that Mg-H complexes are formed in the as grown Mg-doped GaN and therefore hydrogen passivates the Mg acceptors. It is known that hydrogen passivates acceptors in Si. Hydrogen is dissociated from Mg and diffuses out during the electron beam irradiation. [23] Later it was found that annealing the Mg-doped GaN layers at

>750 °C in nitrogen or vacuum also activates the Mg acceptors. [33] First $In_xGa_{1-x}N$ films over sapphire over the whole range $0<x<1$ of composition were grown by Matsuoka *et al.* [34] GaN films were grown at the usual high temperature of 1000 °C. For $x>0$, InGaN films were grown at 500-600 °C depending on the In concentration. The V/III ratio used was high, 1.6×10^4 to 2×10^6.

As mentioned earlier the heterostructure technology is most important for fabricating LEDs, laser diodes (LDs), and FETs. The heterostructures need an AlGaN barrier or cladding layers. AlGaN layered structures were grown firstly by Khan *et al.* [35] in 1990 and by Itoh *et al.* [36] in 1991. InGaN/GaN layered structures were grown firstly by Nakamura *et al.* [37] in 1993. Electron microscopy studies showed that the concentration of defects in the best GaN epilayers was very large, $\sim10^{10}$ cm^{-2}. [38] Photoconductivity experiments showed a large absorption tail, an abrupt Urbach edge was not observed. This showed that a large density of states in the bandgap was produced by the defects.

By middle 1990s so much knowledge and experience in technology had accumulated that the progress in designing and fabricating devices became very rapid. Akasaki and co-workers [30, 41-43] had already made the first *p-n* junction GaN LED in 1989. Room temperature stimulated emission and lasing action were demonstrated at about the same time. Nakamura and his colleagues at Nichia Laboratories brought the blue and green LEDs to level so that they could be commercialized [44,45] in the middle’ 1990s. Nakamura and coworkers published several reviews on the GaN-based LEDs and LDs. [46-50] Khan *et al.* [51] reported the surface mode emission from GaN. Kim *et al.* [52] measured the optical gain. A large number of reports on the fabrication of the optically pumped lasers with improved performance followed. [53-55] Song and Shan [56] have reviewed the subject and have given an extensive list of references. The evolution of thresholds of stimulated and lasing emission has been plotted by these authors in chronological order from 1994 to March 1997.

1.4 Major Issues of Gallium Nitride

There were three major difficulties on fabrication of GaN based devices. First, it is not easy to find suitable substrates so as to produce high quality crystalline layer. Second, it is difficult to obtain high hole concentrations of *p*-type GaN. And third, it is difficult to achieve ohmic contact on *p*-type GaN at lower alloying temperature.

1.4.1 Issues of GaN substrates

GaN films have been fabricated on a number of substrates such as Si, GaAs, $MgAl_2O_4$ (spinel), 6H-SiC, $LiGaO_2$ (LGO) and ZnO, as well as various crystallographic orientations of sapphire. Recently, many improvements have been made in the high quality of GaN by the pre-deposition of a thin AlN or GaN buffer layer. Because of its high quality, large size, and low cost, silicon is viewed as one of the most promising substrates for the growth of GaN. However, due to the large differences in lattice constant, crystal structure, and thermal expansion coefficient, it is rather difficult to grow epitaxial GaN on Si, as shown in Table 1-1. Spinel has a 9.5 % lattice mismatch with respect to GaN while SiC substrates have a 3.5 % mismatch. SiC has good electrical conductivity. A substrate bias can be applied to reduce the ion energy while using nitrogen ions for the growth for the nitrides. But the expensive cost of SiC has restricted its usage. LGO has just a 0.19 % lattice mismatch with GaN but it can’t withstand high temperature and is easily damped and eroded by acid. ZnO has a 2.19 % mismatch with GaN but ZnO is not easily obtained.

Sapphire (Al_2O_3) was the most extensively used substrate for growth of GaN because of its relatively low cost and stability at high temperature. Sapphire has the biggest lattice mismatch of 13.6 % but Akasaki and Amano used a sequence of buffer layers grown at different temperatures to successfully obtain high quality GaN crystalline films. [29-31] The

properties of the GaN epilayer are strongly influenced by the thickness and growth temperature of the buffer layer. Crystal orientations of sapphire and GaN (grown on c-plane [0001] sapphire) were parallel but the unit cell of GaN was rotated by 30° about the c-axis with respect to the sapphire unit cell. The usual method to grow GaN was using metalorganic chemical vapor deposition (MOCVD) on sapphire substrate to form the wurtzite structure. The large lattice mismatch between GaN and sapphire leads to the possibility of high dislocation densities in epilayers. These dislocations may degrade the device performances.

1.4.2 Issues of *p*-type GaN

Doping GaN with acceptors to obtain a high concentration of holes has been a difficult problem. Attempts to dope GaN with Mg acceptors were not so successful in 1970s and early 1980s because Mg was always compensated by the background *n*-type defects or was passivated with hydrogen atoms. It was discovered in the late 1980s by Amano *et al.* [30] that Mg-doped GaN could be converted into *p*-type GaN by LEEBI. They performed experiments on samples grown by MOCVD on AlN buffer layers and sapphire substrates. The layers were doped with 10^{20} Mg atoms/cm^3. The LEEBI was performed with 10 kV electrons with a beam current of 60 μA. After the LEEBI the layer resistivity decreased to 35 Ω-cm. Hall measurements were made and it was found that this resistivity corresponds to a hole concentration of 2×10^{16} cm^{-3} and a mobility of μ=8 cm^2/Vs. These results give an activation ratio of 2×10^{-4} of the Mg atoms, a rather low value. A high activation ratio was obtained by Nakamura *et al.* [57] with GaN layers deposited on GaN buffer layers. The as grown layers were *p* type with a hole concentration = 2×10^{15} cm^{-3}, the hole mobility = 9 cm^2/Vs, and the resistivity = 320 Ω-cm. After LEEBI treatment, the hole concentration became 3×10^{18} cm^{-3}, and the resistivity became 0.2 Ω-cm. The mobility remained unaffected. In subsequent publications Nakamura *et al.* [33, 58] showed that the effect of LEEBI is in fact to heat the

layers and probably to dissociate hydrogen atoms that form complexes with Mg. They found that thermal annealing in vacuum or in nitrogen atmosphere also activates the Mg acceptors without the LEEBI treatment. Thermal annealing of the metalorganic vapor phase epitaxy (MOVPE) grown Mg-doped layers increases the conductivity by up to 6 orders of magnitude than as grown. A hole concentration $>10^{18}$ cm^{-3} is easily obtained at room temperature by the thermal treatment. The effect of thermal treatment is reversible. By heating the activated layers in hydrogen atmosphere, the Mg atoms are deactivated. More recently Gőtz *et al.* [59] have made extensive Hall measurements on Mg-doped GaN epilayers grown by MOCVD on sapphire substrates. They also activated the Mg impurity by thermal annealing and confirmed that on thermal annealing the resistivity decreases by more than 6 orders of magnitude.

Recent experiments by Miyachi *et al.* suggest that the presence of minority carrier electrons helps the activation process. [60] Miyachi *et al.* fabricated the GaN *p-n* diode using Si and Mg dopants. The layers were grown by MOVPE. As-deposited Mg-doped layers were insulating. Different diodes were annealed under different biasing conditions. Under forward bias of 8 V, the resistance of the Mg-doped layer begins to decrease at 300 °C, and saturates at a value five orders of magnitude smaller at 400 °C. Since the device had metal coatings, hydrogen did not diffuse out. It was confirmed by secondary ion mass spectroscopy (SIMS) experiments that the hydrogen profile did not change after annealing. Mg atoms are deactivated by the diodes annealing at 350 °C. If Mg atoms are activated at higher temperatures and without the presence of electrons, as was the case in the experiments [58, 59] discussed above, hydrogen ambient and higher temperatures are necessary for deactivation. Infrared (IR) measurements and theoretical calculations show that in Mg-doped GaN layers grown by MOVPE in hydrogen rich environments, Mg-H complexes are formed. [60] A model to explain the result of activation and deactivation of the GaN diodes in the presence of electrons can now be constructed. [60] The complexes dissociate at the low temperature of about 300 °C. H^+ ions capture electrons and become H^0 atoms. This prevents the back

reaction, i.e., the formation of the Mg-H complex. However, since hydrogen stays in the layer, annealing the diode in the absence of the bias results in ionization of the hydrogen atoms, formation of the complexes at lower temperatures, and deactivation of Mg atoms. Obviously external hydrogen ambient is not necessary in this case. The behavior of the diode annealed under open circuit configuration was different. Practically no activation of Mg was observed even at 600 °C. This result is also different from the earlier result of Nakamura *et al.* [58] who observed activation of Mg at 500 °C. As mentioned earlier, because of the metal coating on both sides of the sample, hydrogen does not diffuse out. This suppresses the activation of Mg in these experiments. [60]

1.4.3 Issues of *p*-type ohmic contact

Metallization are fundaments components to all semiconductor devices and integrated circuits. The essential roles of metallization system are providing the desired electrical paths between the active regions of the semiconductor and the external circuits through the metal contacts and interconnections. High quality and uniform ohmic contact is one of the controlling factors to reduce the parasitic resistance, as well as to improve the yield of good devices performance. The GaN based semiconductors have been applied to optoelectronic devices such as LEDs. Thus ohmic contact to *p*-type GaN is very important. The performance of GaN based LEDs such as operating voltage is strongly influenced by the contact resistance. And one of the factors affecting the lifetime is the *p*-type contact resistance of the devices that generates ohmic heating thus preventing the devices from long life operation. In some research reports, various metal contacts were applied to *p*-type GaN, such as Ni/Au [61, 62], Pd/Au [63], Ni/Pt/Au [64], Pd/Pt/Au [65], Ni/Pd/Au [66], Ni/AuBe [67], Ni/ZnO [68], and Ni-Mg (La or Zn) solid solution/Au series. [69-71] The Ni, Pd, or Pt is the metal in direct contact with the GaN, and the structure is annealed at 400-750 °C. These reported specific

contact resistance (ρ_c) are in the range from 10^{-2} to 10^{-6} Ω-cm^2. But these values are too high for high performance devices. Due to the relatively poor specific contact resistance (ρ_c) achievable, the metallization will heat-up as current flows across the *p-n* junction, leading to metal migration down threading dislocations and eventual shorting of the junction. [72] There are a number of contributing factors to the high ρ_c values for contacts on *p*-type GaN, including:

(i) The absence of a metal with a sufficiently high work function (ϕ_M): the bandgap (Eg) of GaN is 3.4 eV, and the electron affinity (χ) is 4.1 eV, but metal work functions (ϕ_M) are typically ≤5 eV.

(ii) The relatively low hole concentrations in *p*-type GaN due to the deep ionization level of the Mg acceptor (~170 meV).

(iii) The tendency for the preferential loss of nitrogen from the GaN surface during processing, which may produce surface conversion to *n*-type conductivity.

Low contact resistance to *p*-type GaN is difficult to obtain because of the difficulty to achieve high hole concentrations in *p*-type GaN and lack of metals with high work function (ϕ) compared the bandgap and electronegativity of GaN. Work functions and electronegativity of some elements as show in Table 1-2. In a GaN baesd LED, Ni/Au are commonly used as ohmic contact on *p*-type GaN top layer. But the low doping level of the *p*-type GaN layer may result in a non-ohmic contact and high contact resistance, thereby degrading the performance of devices. For higher temperatures severe degradation in contact morphology is observed, usually resulting from the formation of the metal gallides.

In addition, the current coming from the electrode cannot be spread effectively through the entire chip due to high resistivity of the *p*-type GaN. One way to avoid this so-called current crowding problem, thereby obtaining high efficiency and uniform light emission from the device, is to design the pattern of the top electrode to be interdigitated finger shape. However, this type of electrode reduces the emitted light output. Thus, a low resistance

p-electrode with high transparency is an important issue for fabrication of GaN based LED although well known transparent conducting films such as indium tin oxide (ITO) and cadmium tin oxide (CTO) have been used as electrode of LEDs. [73, 74] However, ITO transparent conducting film on *p*-type GaN shows Schottky contact characteristics after thermal annealing. If the carrier concentration of GaN increases to the order of larger than 10^{18} cm^{-3}, the formation of ITO ohmic contact on GaN may be possible.

1.5 Overview of This Dissertation

This dissertation contains eight chapters. In chapter 1, we introduce to history of GaN material, GaN based LEDs, semiconductor materials of light emitting devices, evolution of LEDs' performance, and several key issues for fabricated the III-V nitride LEDs.

In chapter 2, we review the theory and background of this dissertation. The principles of ohmic contacts, metal-semiconductor junctions, current-voltage (*I-V*) characteristics, degradation and reliability for LEDs, and threading dislocations (TDs) have been detailed.

In chapter 3, we detail the experiments and analysis methods. The structures of epitaxial wafers and devices have been depicted. We also show the flow chart of GaN based LEDs process. The circular transmission line model (CTLM) is used to measure the specific contact resistance (ρ_c). The depth profile of carrier concentration is generally measured by *C-V* method. Scanning electron microscopy (SEM), transmission electron microscope (TEM), photoluminescence (PL) and Hall effect measurement have been introduced briefly.

In chapter 4, the influences of thermal annealing on Ni/*p*-type GaN have been investigated. The electrical and optical properties were analyzed with Hall effect and photoluminescence (PL) measurements. The material analyses were qualified by x-ray diffraction (XRD).

In chapter 5, we have fabricated GaN based LEDs using transparent Ni/Au and indium

tin oxide (ITO) for *p*-type contacts. The effect of thermal annealing on *I-V* properties of GaN LEDs has been studied. According to TEM, SEM, and energy-dispersive X-ray spectrometer analyses (EDS), this chapter provides the direct evidence that metals in-diffusion along the TDs cause the degradation of the LEDs characteristics.

In chapter 6, we have fabricated GaN LEDs using transparent ITO-based *p* contacts. The contact properties of ITO-based contact metals have been obtained with thermal treated. The *I-V* characteristics and life tests of GaN based LEDs have been studied. According to TEM, SEM, and EDS analyses, we have understood the influences of contact interfaces between the ITO-based layer and GaN LEDs.

In chapter 7, GaN based LEDs with naturally textured surface have been grown by metal organic chemical vapor deposition (MOCVD) on c-plane sapphire substrate. The *I-V* characteristics, light output intensity-current (*L-I*) characteristics and life tests of GaN based LEDs have been studied. Using SEM and TEM analyses, we observed the structure of truncated pyramid on LED with Mg treatment *p*-GaN layer obviously.

Finally, we summarized the overall results of our studies and discussed future works in chapter 8.

1.6 References

[1] M. Fukuda, "Optical Semiconductor Devices", John Wiley & Sons, Inc., (1999).

[2] F. A. Ponce and D. P. Bour, Nature (London) **386**, 351 (1997).

[3] W. Xie, D. C. Grillo, R. L. Gunshor, M. Kobayashi, H. Jeon, J. Ding, A. V. Nurmikko, G. C. Has and N. Otsuka, Appl. Phys. Lett. **60**, 1999 (1992).

[4] J. Edmond, H. Kong and V. Dmitrieve, Inst. Phys. Conf. Ser. **137**, 515 (1994).

[5] J. I. Pankove, E. A. Miller and J. E. Berkeyheiser, RCA Review **32**, 283 (1971).

[6] K. Koga and T. Yamaguchi, Pro. Crystal Growth and Charact. **23**, 127 (1991).

[7] S. Strite and H. Morkoc, J. Vac. Sci. Technol. **B10**, 1237 (1992).

[8] H. Morkoc, S. Strite, G. B. Gao, M. E. Lin, B. Sverdlov and M. Burns, J. Appl. Phys. **76**, 1363 (1994).

[9] S. Nakamura, N. Iwasa, M. Senoh and T. Mukai, Jpn. J. Appl. Phys. **31,** 1258 (1992).

[10] M. Rubin, N. Newman, J. S. Chan, T. C. Fu and J. T. Ross, Appl. Phys. Lett. **64**, 64 (1994).

[11] M. S. Brandt, N. M. Johnson, R. J. Molnar, R. Singh and T. D. Moustakas, Appl. Phys. Lett. **64**, 2264 (1994).

[12] J. M. Zavada, R. G. Wilson, C. R. Abernathy and S. J. Pearton, Appl. Phys. Lett. **64**, 2724 (1994).

[13] S. Nakamura, Nikkei Electronics Asia **6**, 65 (1994).

[14] S. Nakamura, T. Mukai and M. Senoh, Appl. Phys. Lett. **64**, 1687 (1994).

[15] S. Nakamura, M. Senoh, N. Iwasa and S. Nagahama, Jpn. J. Appl. Phys. **34,** 1797 (1995).

[16] S. Nakamura, M. Senoh, N. Iwasa and S. Nagahama, Appl. Phys. Lett. **67**, 1868 (1995).

[17] S. Nakamura, M. Senoh, N. Iwasa, S. Nagahama, T. Tamada and T. Mukai, Jpn. J. Appl. Phys. **34,** L1332 (1995).

[18] S. Nakamura, J. Vac. Sci Technol. **A10**, 705 (1995).

[19] S. Nakamura, T. Mukai and M. Senoh, J. Appl. Phys. **76,** 8189 (1994).

[20] R. Juza and H. Hahn, Z. Anorg. Allg. Chem. **234**, 282 (1938); and **244**, 133 (1940).

[21] H. Grimmeiss and Z. H. Koelmans, Nature (London) **14a**, 264 (1959).

[22] H. P. Maruska and J. J. Tietjen, Appl. Phys. Lett. **15**, 327 (1969).

[23] J. I. Pankove, in "GaN and Related Materials", edited by S. J. Pearton, Gordon and Breach Science Publishers, 1 (1997).

[24] J. I. Pankove, E. A. Miller and J. E. Berkeyheiser, J. Lumin. **5**, 84 (1972); J. I. Pankove, M. T. Duffy, E. A. Miller and J. E. Berkeyheiser, J. Lumin. **8**, 89 (1972).

[25] H. P. Maruska, W. C. Rhines and D. A. Stevenson, Mater. Res. Bull. **7**, 777 (1972).

[26] J. I. Pankove and H. E. P. Schade, Appl. Phys. Lett. **25**, 53 (1974).

[27] M. T. Duffy, C. C. Wang, G. D. O'Clock, S. H. McFarlane and P. Z. Zanzucchi, J. Electron. Mater. **2**, 359 (1973).

[28] S. Yoshida, S. Misawa and S. Gonda, Appl. Phys. Lett. **42**, 427 (1983).

[29] H. Amano, I. Akasaki, T. Kozawa, K. Hiramatsu, N. Sawak, K. Ikeda and Y. Ishi, J. Lumin. **40-41**, 121 (1988).

[30] H. Amano, N. Sawaki, I. Akasaki and Y. Toyoda, Appl. Phys. Lett. **48**, 353 (1986); H. Amano, I. Akasaki, T. Kozawa, K. Hiramatsu, N. Sawaki, K. Ikeda and Y. Ishii, J. Lumin. **40-41**, 121 (1988); H. Amano, M. Kito, K. Hiramatsu and I. Akasaki, Jpn. J. Appl. Phys. **28**, L2112 (1989).

[31] I. Akasaki, H. Amano, M. Kito and K. Hiramatsu, J. Lumin. **48-49**, 666 (1991).

[32] J. A. Vechten, J. D. Zook and R. D. Horning, Jpn. J. Appl. Phys. **31**, 3662 (1992).

[33] S. Nakamura, N. Iwasa, M. Senoh and T. Mukai, Jpn. J. Appl. Phys. **31**, 1258 (1992).

[34] T. Matsuoka, H. Tanaka, T. Sasaki and A. Katsui, Inst. Phys. Conf. Ser. **106**, 141 (1990).

[35] M. A. Khan, R. A. Skogman and J. M. Van Hove, Appl. Phys. Lett. **56**, 257 (1990).

[36] K. Itoh, T. Kawamoto, H. Amano, K. Hiramatsu and I. Akasaki, Jpn. J. Appl. Phys. **30**, 1924 (1991).

[37] S. Nakamura, T. Mukai and M. Senoh, Jpn. J. Appl. Phys. **32**, L8 (1993).

[38] S. S. Lester, F. A. Ponce, M. G. Craford and D. A. Steigerwald, Appl. Phys. Lett. **66**, 1249 (1995).

[39] R. Dingle, K. L. Shaklee, R. F. Leheny and R. B. Zetterstrom, Appl. Phys. Lett. **19**, 5 (1971).

[40] B. Monemar, The Second International Conference on Nitride Semiconductors, Tokushima, Japan, 6 (1997).

[41] I. Akasaki and H. Amano, Tech. Dig. Int. Electron Devices Meet. **96**, 231 (1996).

[42] I. Akasaki, H. Amano and I. Suemune, Inst. Phys. Conf. Ser. **142**, 7 (1996).

[43] H. Amano, T. Asahi and I. Akasaki, Jpn. J. Appl. Phys. **29**, L205 (1990).

[44] S. Nakamura and G. Fasol, "The Blue Laser Diodes", Springer, Heidelberg, (1997).

[45] S. J. Pearton, J. C. Zolper, R. J. Shul and F. Ren, J. Appl. Phys. **86**, 1 (1999).

[46] S. Nakamura, MRS Bull. **22**, 29 (1997).

[47] S. Nakamura, in "GaN and Related Materials", edited by S. J. Pearton, Gordon and Breach Science Publishers, 471 (1997).

[48] S. Nakamura, in ''Applications of LEDs and LDs'' in GaN, edited by J. Pankove and T. D. Moustakas, Academic, Vol. 1, (1998).

[49] S. Nakamura, Sel. Top. Quantum Electron. **3**, 712 (1997).

[50] S. Nakamura, Science **281**, 956 (1998).

[51] M. A. Khan, D. T. Olsen, J. M. Van Hove and J. N. Kuznia, Appl. Phys. Lett. **58**, 1515 (1990).

[52] S. T. Kim, H. Amano, I. Akasaki and N. Koide, Appl. Phys. Lett. **64**, 1535 (1994).

[53] I. Akasaki, H. Amano, S. Sota, S. Saki, T. Tanaka and M. Koike, Jpn. J. Appl. Phys. **34**, L1517 (1995).

[54] K. Kim, W. R. L. Lambrecht and B. Segall, Phys. Rev. B **50**, 1502 (1994).

[55] T. J. Schmidt, X. H. Yang, W. Shan, J. J. Song, A. Salvador, W. Kim, O. Aktas, A.

Botchkarev and H. Morkoc, Appl. Phys. Lett. **68**, 1820 (1996).

[56] J. J. Song and W. Shan, Group III Nitride Semiconductor Compounds", edited by B. Gil, Clarendon, Oxford, (1998).

[57] S. Nakamura, M. Senoh and T. Mukai, Jpn. J. Appl. Phys. **30**, L1708 (1991).

[58] S. Nakamura, T. Mukai, M. Senoh and N. Iwasa, Jpn. J. Appl. Phys. **31**, L139 (1992).

[59] W. Götz, N. M. Johnson, J. Walker, D. P. Bour and R. A. Street, Appl. Phys. Lett. **68**, 667 (1996).

[60] M. Miyachi, T. Tanaka, Y. Kimura and H. Ota, Appl. Phys. Lett. **72**, 1101 (1998).

[61] J. K. Ho, C. S. Jong, C. C. Chiu, C. N. Huang and K. K. Shih, Appl. Phys. Lett. **74** 1275 (1999).

[62] J. K. Ho, C. S. Jong, C. C. Chiu, C. N. Huang, K. K. Shih, L. C. Chen, F. R. Chen and J. J. Kai, J. Appl. Phys. **86** 4491 (1999).

[63] T. Kim, J. Kim, S. Chae and T. Kim, Mater. Res. Soc. Symp. Proc. **468**, 427 (1997).

[64] J. S. Jang, K. H. Park, H. K. Jang, H. G. Kim and S. J. Park, J. Vac. Sci. Technol. **B16** 3105 (1998).

[65] D. J. King, L. Zhang, J. C. Ramer, S. D. Hersee, and L. F. Lester, Mater. Res. Soc. Symp. Proc. **468**, 421 (1997).

[66] C. F. Chu, C. C. Yu, Y. K. Wang, J. Y. Tsai, F. I. Lai and S. C. Wang, Appl. Phys. Lett. **77** 3423 (2000).

[67] L. C. Chen, C. Y. Hsu, W. H. Lan and S. Y. Teng, Solid-State Electron. **47** 1843 (2003).

[68] J. O Song, K. K. Kim, S. J. Park and T. Y. Seong, Appl. Phys. Lett. **83** 479 (2003).

[69] J. O Song, D. S. Leem and T. Y. Seong, Appl. Phys. Lett. **83** 3513 (2003).

[70] J. O Song, D. S. Leem, J. S. Kwak, S. N. Lee, O. H. Nam, Y. Park and T. Y. Seong, Appl. Phys. Lett. **84** 1504 (2004).

[71] J. O Song, D. S. Leem and T. Y. Seong, Appl. Phys. Lett. **84** 4663 (2004).

[72] S. Nakamura, M. Senoh and T. Mukai, Appl. Phys. Lett. **62**, 2390 (1993).

[73] J. F. Lin, M. C. Wu, M. J. Jou, C. M. Chang, B. J. Lee and Y. T. Tsai, Electron Lett. 30, 1793 (1994).

[74] M. Hagerott, H. Jeon, A. V. Nurmikko, W. Xie, D. C. Grillo, M. Kobayashi and R. L. Gunshor, Appl. Phys. Lett. **60** 2825 (1992).

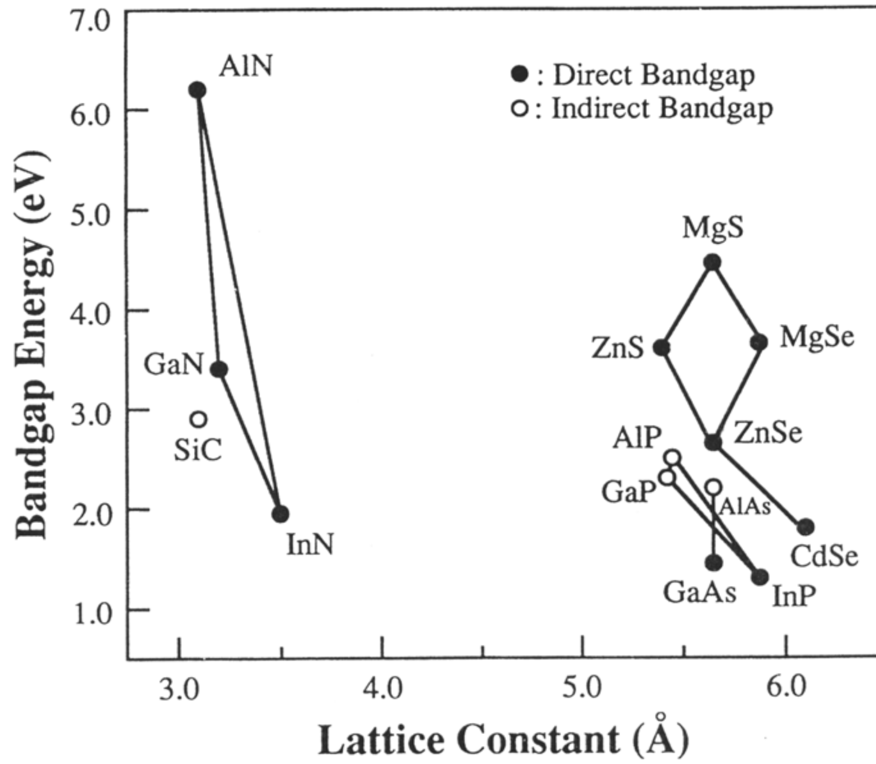

Figure 1-1 Bandgap energy of various materials for visible emission devices as a function of their lattice constant. [47]

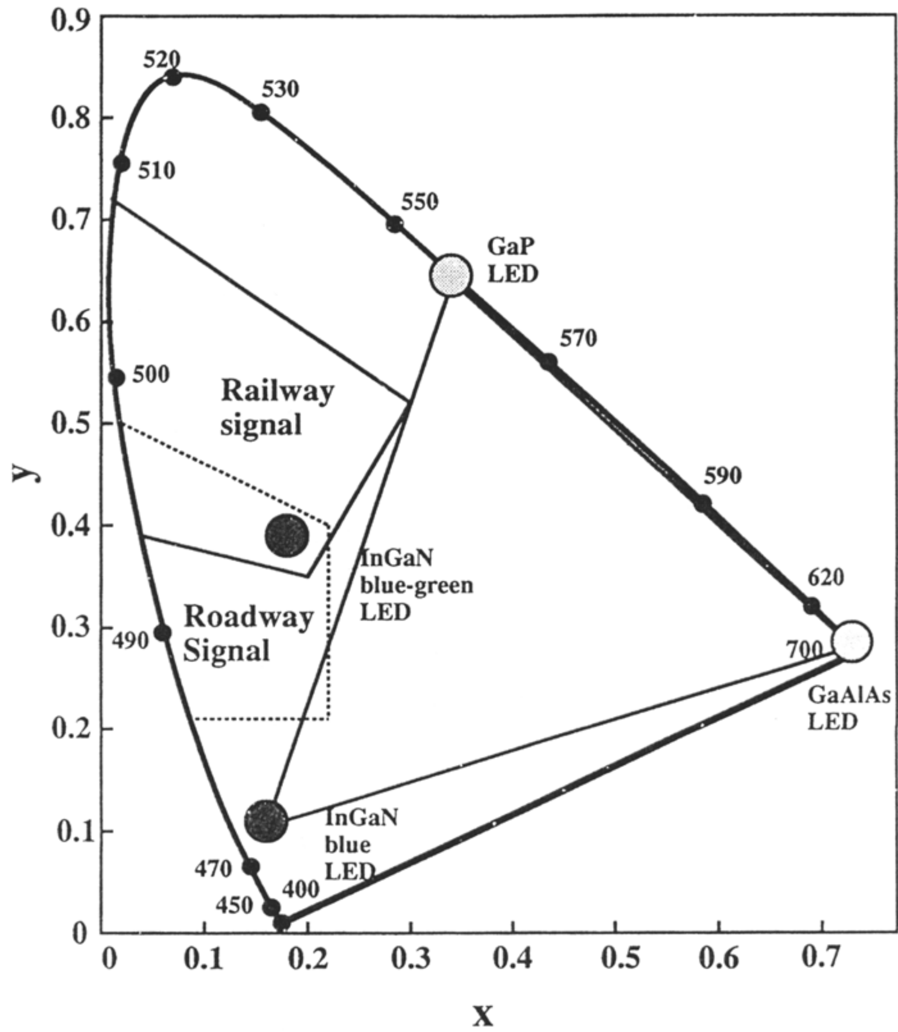

Figure 1-2 Chromaticity diagram where blue InGaN/AlGaN LEDs, blue-green InGaN/AlGaN LEDs, green GaP LEDs and red GaAlAs LEDs are shown. [47]

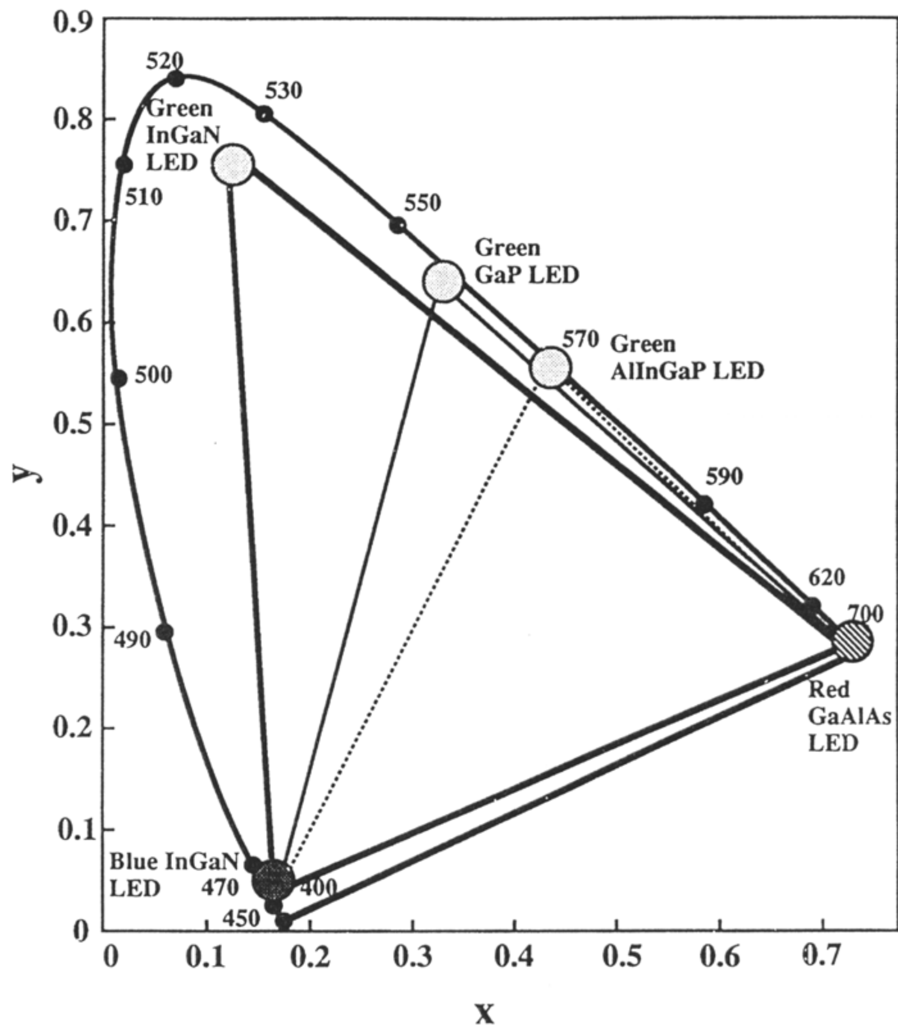

Figure 1-3 Chromaticity diagram in which blue InGaN SQW LED, green InGaN LED, green GaP LED, green AlInGaP LED and red GaAlAs LED are shown. [47]

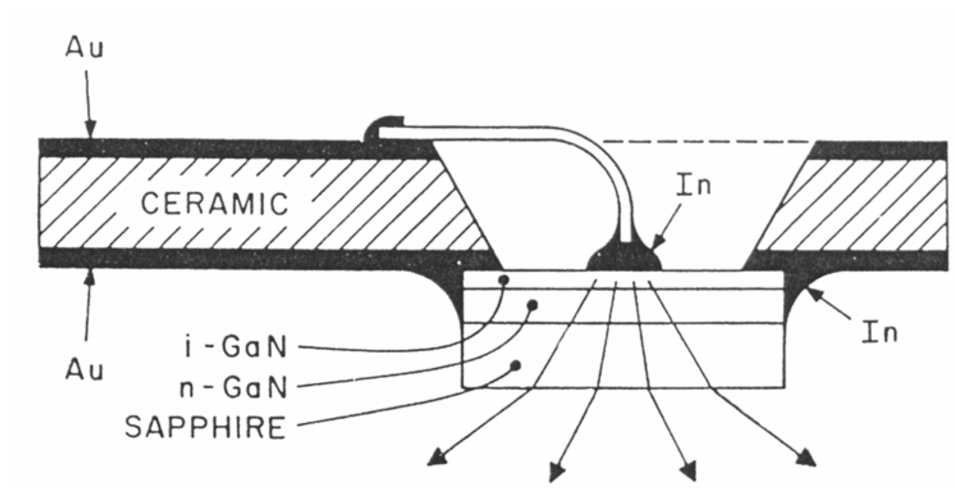

Figure 1-4 Structure of GaN m-i-n LED. [23]

Table 1-1 Properties of GaN substrates

Substrate material	Symmetry	Lattice parameters (Å)	Thermal expansion coefficient (10^{-6}/K)
Wurtzite GaN	Hexagonal	a = 3.189 c = 5.189	5.6 3.2
Wurtzite GaN	Hexagonal	a = 3.112 c = 4.982	4.2 5.3
a-Al_2O_3	Hexagonal	a = 4.758 c = 12.99	7.5 8.5
Si	Cubic	a = 5.430	3.6
GaAs	Cubic	a = 5.563	6.0
6H-SiC	Hexagonal	a = 3.080 c = 15.12	—
3C-SiC	Cubic	a = 3.436	—
InP	Cubic	a = 5.869	4.5
GaP	Cubic	a = 5.451	4.7
MgO	Cubic	a = 4.622	10.5
$LiAlO_2$	Tetragonal	a = 5.169 b = 6.268	7.1 7.5
$LiGaO_2$	Orthorhombic	a = 5.402 b = 6.372 c = 5.007	6.0 9.0 7.0
ZnO	Hexagonal	a = 3.252 c = 5.213	2.9 4.8
$MgAl_2O_4$	Cubic	a = 8.083	7.5

Table 1-2 Work functions and electronegativity of some elements (Unit: eV)

Metal	Work function	Electronegativity
Pt	5.65	2.2
Ni	5.15	1.8
Pd	5.12	2.2
Au	5.10	2.4
Co	5.00	1.8
Cu	4.65	1.9
Mo	4.60	1.8
W	4.55	1.7
Hg	4.50	1.7
Fe	4.52	1.8
Cr	4.50	1.6
Sn	4.42	1.8
Ti	4.33	1.5
Al	4.28	1.5
Ag	4.26	1.9
Ta	4.25	1.5
Ga	4.20	1.6
In	4.12	1.7
Be	3.92	1.6
Mg	3.66	1.2
Ca	2.87	1.0
Ba	2.70	0.9
Cs	2.14	0.7

CHAPTER 2

Theory and Background

2.1 Principles of the Formation of Ohmic Contacts

The metal-semiconductor (MS) contact plays a very important role of all solid-state devices. When metal-semiconductor interfaces are formed, they can provide either rectifying Schottky contacts or ohmic contacts. Schottky contacts exhibit low levels of current at reverse bias, while at forward bias current flows readily across the metal/semiconductor interface. On the other hand, ohmic contacts have linear or quasi-linear current-voltage characteristics at forward and reverse biases or low specific contact resistance, which is the resistance at the interface between the metal and the semiconductor. The energy band diagram is used to describe an ideal MS contact under equilibrium conditions. The surface-included energy band diagrams for the individual, electrically isolated metal and semiconductor components are shown in Fig. 2-1.

In Fig. 2-1, the ledge at the top of the vertical line denotes the minimum energy an electron must possess to completely free itself from the material and is called vacuum level, E_0. The energy difference between the vacuum level and the Fermi energy (E_F) is known as the work function (ϕ) of the material. The metal work function (ϕ_M) is an invariant fundamental property of the specified metal. The semiconductor work function (ϕ_S) is composed of two distinct parts; that is

$$\phi_S = \chi + (E_C - E_F) \quad (2\text{-}1)$$

The electron affinity, $\chi \equiv (E_0 - E_C)|_{surface}$, is an invariant fundamental property of the specified semiconductor.

Suppose now the $\phi_M > \phi_S$ metal and *n*-type semiconductor of Fig. 2-1 is brought

together to form an ideal MS contact. Assuming the contact formation is accomplished almost instantaneously so that there is negligible electron transfer between components during the contacting process. In metal and *p*-type semiconductor contact, the energy band diagram for the contact will be as shown in Fig. 2-2. In this figure the isolated energy band diagrams are vertically aligned to common vacuum reference level and simply abutted at the mutual interface. It should be emphasized that ϕ_M and χ are material constants and remain unaffected by the contacting process. In Fig. 2-2, $\phi_M=q\Phi_M$, $\phi_S=q\Phi_S$, and $\chi=qx$; Φ_M and Φ_S are metal and semiconductor work function potential respectively.

Since $E_{FS}\neq E_{FM}$, the MS contact characterized by Fig. 2-2(a) is obviously not in equilibrium. Under equilibrium conditions the Fermi level in a material or group of materials in intimate contact must be invariant with position. Consequently, a short time after the conceptual contact formation, holes will begin transferring from the semiconductor to the metal given the situation as shown in Fig. 2-2(a). The net loss of holes from the semiconductor creates a surface depletion region and a growing barrier to hole transfer from the semiconductor to the metal. This will continue until the transfer rate across the interface is the same in both directions and E_F is the same throughout the structure. The net result, the equilibrium energy band diagram for an ideal $\Phi_M<\Phi_S$ metal to *p*-type semiconductor contact, is shown in Fig. 2-2(b). In drawing this figure, extraneous lines such as the vacuum reference level and the portion of the vertical surface line above E_C have been removed. Also note that

$$\Phi_B = E_{FM} - E_{V\,|\,interface} \quad \text{-----} \quad \text{ideal } MS_{(p\text{-type})} \text{ contact} \qquad (2\text{-}2)$$

Where Φ_B is the surface potential-energy barrier encountered by holes with $E=E_F$ in the metal. Finally, if the entire argument is repeated for a metal and *p*-type semiconductor where $\Phi_M>\Phi_S$, one obtains the equilibrium energy band diagram shown in Fig. 2-2(d).

The conclusion of ideal MS contact formed from a metal and a *p*-type semiconductor will be a rectifying contact if $\Phi_M<\Phi_S$ and an ohmic-like contact if $\Phi_M>\Phi_S$. Parallel arguments applied to an ideal MS contact formed from a metal and an *n*-type semiconductor

lead to the conclusion that the contact will be rectifying if $\Phi_M > \Phi_S$ and ohmic-like contact if $\Phi_M < \Phi_S$. However, this presents a problem in large bandgap *p*-type semiconductors such as GaN. The sum of Eg and χ can be quite large (the value for GaN is about 7.5 eV), and the highest work function for a metal (Pt) is 5.7 eV. It is difficult to eliminate the barrier in *p*-GaN. Therefore, it is necessary to employ other methods to achieve ohmic behavior.

2.2 Current Flow in Metal-Semiconductor Junctions

In cases when defects are not involved. There are three types of conduction mechanisms for carrier transport across the interface between metals and semiconductors: thermionic emission (TE), thermionic-field emission (TFE), and field emission (FE). [1]

(1) Thermionic emission (TE): for moderately doped semiconductor, $N_d < \sim 10^{17}$ cm^{-3}, the depletion region is relatively wide. It is nearly impossible to tunnel through the barrier unless aided by defects that are considered not to exit in this ideal picture. The electrons, however, can surmount the top of barrier, which should be small for contacts, by thermionic emission (Fig. 2-3(a)). For low-doped or high-barrier semiconductors, on the other hand, the vast majority of electrons would be unable to cross in either direction into the semiconductor; and ohmic contact behavior is not observed.

(2) Thermionic-field emission (TFE): for intermediately doped semiconductors, $\sim 10^{17} < N_d < \sim 10^{18}$ cm^{-3}, the depletion region is not sufficiently thin to allow direct tunneling of carriers that are more or less in equilibrium. But, if the carriers gain a little energy, they may be able to tunnel. Consequently, both thermionic emission and tunneling take place (Fig. 2-3(b)).

(3) Field emission (FE): for heavily doped semiconductors, $N_d > \sim 10^{18}$ cm^{-3}, the depletion region is narrow, and direct electron tunneling from the metal to the semiconductor is allowed (Fig. 2-3(c)). In the absence of a good match between the metal and the

semiconductor work function, which is generally the case that is the best approach to pursue for ohmic contacts.

For *p*-GaN, a metal or compound with a very large work function is required to make an ohmic contact (electron affinity plus bandgap is 4.1 eV + 3.4 eV = 7.5 eV) if TE is the dominant transport mechanism. Since there are no metals or compounds with such a large work function, ohmic contacts must be formed by either highly doping the surface region to enhance field emission [2], by reducing the Schottky barrier height through surface treatment, or by using an intermediate semiconducting layer (ISL). Another limitation in *p*-type GaN is the doping level that can be achieved in *p*-GaN, which also limits formation of ohmic contacts by field emission.

In summary, metal ohmic contacts to *p*-GaN may be achieved in three ways [3]. Figure 2-4 schematically presents these methods for a *p*-type semiconductor. The first method (see Fig. 2-4(a)) is to use a metal that has a large metal work function so that the potential barrier between the metal and semiconductor is minimized. However, it is well known that metals with sufficiently large work functions are lacking. The second method, which is also the most common, is to dope the semiconductor heavily. As a result, the depletion width is reduced, and the tunneling possibility at the contact is then increased. However, it is known that it is hard to dope *p*-type GaN heavily due to the large ionization energy of the dopant Mg. A third technique (see Fig. 2-4(c)) is to decrease the bandgap of the semiconductor by the formation of an intermediate semiconducting layer (ISL) at the metal/semiconductor interface. By increasing the depletion width and separating the barrier height at the metal/semiconductor interface into the barrier heights at the metal/ISL/semiconductor interfaces, the effective barrier height decreases. However, the behavior of the interface is not completely understood at this time, so it is not immediately known how to accomplish these goals.

2.3 Current-Voltage Characteristics of *P-N* Junction Diodes

2.3.1 The case of a forward-biased *p-n* junction

The current I of a *p-n* junction is usually written as a function of the diode Voltage V_d as

$$I = I_0\left(\exp\left(\frac{qV_d}{nkT}\right) - 1\right) \qquad (2\text{-}3)$$

where I_0 is the saturation current and n the diode ideality factor. The diode voltage V_d is voltage across the space-charge region and excludes any voltage drops across the *p* and *n* quasi-neutral region. If both I_0 and n are constant, then a plot of log(I) versus V_d yields a straight line provided $V_d >> nkT / q$.

A semiconductor diode can be represented by the equivalent circuit of Fig. 2-5(a), consisting of an ideal diode in series with resistance r_s. [4] When current flows through the device, the diode terminal voltage V is

$$V = V_d + Ir_s \qquad (2\text{-}4)$$

With series resistance, Eq. (2-3) becomes

$$I = I_0\left(\exp\left(\frac{q(V - Ir_s)}{nkT}\right) - 1\right) \qquad (2\text{-}5)$$

The current in *p-n* junction diodes is due to two components: space-charge region (scr) recombination-generation and quasi-neutral region (qnr) recombination-generation, leading to *I-V* relationship

$$I = I_{0,scr}\left(\exp\left(\frac{q(V - Ir_s)}{nkT}\right) - 1\right) + I_{0,qnr}\left(\exp\left(\frac{q(V - Ir_s)}{nkT}\right) - 1\right) \qquad (2\text{-}6)$$

Equation (2-6) is plotted in Fig. 2-5(b). [4] There are four distinct regions in the figure. For Ir_s << V << nkT / q, the current depends linearly on voltage $\left(\exp(qV/nkT) - 1 \approx qV/nkT\right)$, giving a nonlinear curve on the semilog plot of Fig. 2-5(b). For $V >> nkT / q$ and V >> Ir_s, the current is dominated by scr recombination at low current and by qnr recombination at higher

current. The breakpoint between the two current components occurs at V = 0.3 V in this example. The I-V curve deviates from linearity at high current due to series resistance r_s.

Extrapolating the two linear regions to $V = 0$ gives $I_{0,\,scr}$ and $I_{0,\,qnr}$. The slope is given by

$$S = \frac{d\log(I)}{dV} \tag{2-7}$$

Knowing the slope and sample temperature allows the ideality factor to be determined using the relationship

$$n = \frac{1}{\ln(10)SkT/q} = \frac{1}{2.3SkT/q} \tag{2-8}$$

We will generally use the logarithm to base 10, written as "log," instead of the logarithm to base e, written as "ln," because experimental data are plotted on "log," not "ln," scales.

The deviation of the log(I)-V curve from linearity is $\Delta V = Ir_s$, allowing r_s to be determined according to

$$r_s = \frac{\Delta V}{I} \tag{2-9}$$

Semiconductor device and circuit performance is generally degraded by series resistance. The extent of such degradation depends on the series resistance, on device, on the current flowing through the device, and on a number of other parameters. The series resistance (r_s) depends on the semiconductor resistivity, on the contact resistance, and sometimes on geometrical factors. Series resistance may be very large before causing device degradation for some devices.

2.3.2 The case of a reverse-biased *p-n* junction

The ideal diode theory predicts a small, voltage-independent saturation current I_0, when the junction is sufficiently reverse biased. In junction diodes where the reverse current is dominated by a carrier generation in the space-charge region or surface leakage, current does not saturate but is found to increase with the reverse bias. However, this increase is too small to cause any perceptible change in rectifying properties of the diode. Even in junctions in

which the space-charge region and surface leakage currents are negligible, it is observed that the reverse current increases gradually with the bias until a critical voltage is reached at which the current increases abruptly with the voltage. This phenomenon is known as breakdown of the *p-n* junction.

Figure 2-6 shows the *I-V* characteristic of a typical *p-n* junction diode including the reverse breakdown region. [5] Two features of the breakdown are noteworthy. First, the breakdown is only electrical, and there is no mechanical damage to the diode. Second, the breakdown is reversible and nondestructive as long as the power dissipation at the junction is kept below the value allowed by thermal considerations.

There are two basically different mechanisms of junction breakdown: the Zener mechanism (also known as internal field emission), due to tunneling, and avalanche breakdown. The Zener mechanism involves the direct excitation of electrons from the valence band to the conduction band under the action of the high electric field in the junction depletion region, and it occurs only in *p-n* junctions whose two sides are heavily doped so that the width of the depletion layer is small. Avalanche breakdown is caused by a process known as secondary multiplication, and it occurs in junctions having thicker depletion regions, which makes tunneling less probable. [6]

For a qualitative understanding of the breakdown mechanisms in *p-n* junctions, it is helpful to consider the relationships between the impurity concentration, the depletion region width, and the electric field in junction region. For simplicity, let us consider an abrupt p^+-n junction. Neglecting the depletion width in the p^+-region, the following relations are obtained

$$W^* = \sqrt{\frac{2\varepsilon_s}{qN_d}} \tag{2-10}$$

$$W = W^* \sqrt{(V_i + V_R)} \quad \text{and} \quad |E_m| = \frac{2\sqrt{(V_i + V_R)}}{W^*} \tag{2-11}$$

where $V_R = -V_a$ is the applied reverse voltage, W^* width constant (cm/V$^{1/2}$), W depletion

region width (cm), N_d donor concentrations (cm^{-3}), ε_s semiconductor permittivity (F/cm), E_m the maximum electric field, and V_i built-in voltage (V). It is possible to understand the breakdown mechanisms with the help of these relations.

(1) Zener breakdown (or internal field emission): Breakdown because of internal field emission is called Zener breakdown. Equation (2-11) shows that when N_d is large, W^* is small and E_m is high even for small voltages. Under these conditions, the depletion layer width W is small, and the electrons from the valence band on the p-side of the junction can tunnel into the empty states in the conduction band on the n-side as shown in Fig. 2-7(a). If W^* and V_R are such that E_m exceeds 10^6 V/cm, the tunnel current becomes sufficiently high to cause the junction breakdown.

(2) Avalanche breakdown: As the impurity concentration N_d is decreased, both W^* and W increase, and E_m decreases. A point is reached where E_m has a value smaller than that required for tunneling. In a reverse-biased junction, the thermally generated minority carriers (mainly holes in a p^+-n junction) injected into the space-charge region are accelerated by the field and gain kinetic energy from the field. When the junction voltage is large enough to produce a sufficiently high field, some of the accelerated carriers gain energy higher than the gap energy Eg. A carrier that has energy appreciably higher than Eg can produce a secondary electron-hole pair by knocking out an electron from the covalent bond of a lattice atom in the depletion region, as shown in Fig. 2-7(b). The secondary carriers produced by this process can produce further electron-hole pairs. Avalanche breakdown occurs when the number of carriers produced by this ionization process becomes very large.

For an accelerated carrier, the ionization collision is not the only event by which the gained energy can be lost. A carrier may also lose its energy to the crystal lattice by emitting phonons, as shown in Fig. 2-7(c). This energy loss to phonons obviously does not contribute to the ionization process.

2.3.3 Leakage current

In addition to thermionic emission, thermionic field emission and tunneling current, other current such as defect-assisted tunneling and others that may have an ohmic nature, can be lumped in leakage component and can be expressed as

$$I_r = \frac{V - Ir_s}{R_t} \tag{2-12}$$

where I_r is leakage current, V is the diode terminal voltage, r_s is series resistance, and R_t is considered to be a fitting parameter which represents defects and inhomogeneities at the metal-semiconductor interface.

In fact, the low hole concentration combined with a large hole effective mass preclude direct tunneling in *p*-type GaN. What may be happening in presently utilized a Ni/Au contact is that, Ni/Au chemically modifies the GaN surface and the current conduction mechanism may be dominated by defect-assisted tunneling that we will call "leakage current".

2.4 Basics of Degradation and Reliability for LEDs

The reliability of a device is determined by the weakest part of the device and depends on factors ranging from material properties to processing technologies. Failure modes can be roughly divided into three categories: sudden, rapid, and gradual in corresponding to the degrading part. The failure modes and their causes for laser diodes and LEDs (forward bias devices) are summarized in Fig. 2-8. [7] The main causes of failure and the factors enhancing the failure are summarized in Table 2-1. LEDs and leaser diodes use radiative recombination of the injected carriers, pin-photodiodes and avalanche photodiodes (APDs) detect photocurrent by dividing electrons and holes at the *p-n* junction, and modulators require a

strong electric field at *p-n* junction for normal operation. The degradation mechanisms of such devices can be roughly divided into two categories according to the direction of bias at the *p-n* junction. For devices used under a forward bias, the main factors in degradation are the current flow through the *p-n* junction and the emitted light, whereas for devices used under a reverse bias the main factor is the high electric field at the *p-n* junction.

As summarized in Table 2-1, the degradation of optoelectronic *p-n* junction devices used under forward bias occurs at electrodes (diffusion and reaction), crystals (dislocation and precipitation), and bonding parts. Facet degradation is also a factor in laser diodes, and buried heterointerface (BH) degradation occurs in devices with a buried heterostructure. These degradations are observed in bulk, quantum well (QW), and strained QW devices and they determine device reliability. LEDs are generally used under constant current conditions, so their degradation is usually monitored by measuring the reduction of optical output power. This output power reduction is mainly caused by the dislocation network growth and the electrode degradation (for devices having alloy-type electrodes), both of which are degradation of the inner active region.

2.5 The Role of Threading Dislocations in GaN Based LEDs

Currently, there are still no widely available lattice-matched substrates for the growth of wurzitic GaN. As a result, most materials still have high threading dislocation (TD) densities. The commonly observed extended defects in (0001) oriented GaN grown on sapphire substrates include (0001) stacking faults and stacking disorder and related Shockley and Frank partial dislocations, inversion domains, and TDs. [8] The TDs have typical total densities in the range 10^8-10^{10} cm^{-2}. There are two different predominantly observed TDs: pure edge, with Burgers vectors in the family $\frac{1}{3}\langle\bar{2}110\rangle$ and [0001] line directions; and

mixed character, with Burgers vectors in the family $\frac{1}{3}\langle\bar{2}113\rangle$ and line directions inclined ~10° from [0001] towards the Burgers vector. Pure screw TDs (b = [0001] and line direction [0001]) represent a small fraction (~0.1-1 %) of the total density of TDs [8]. Note that TDs are the only extended defects that grow through to the free surface of the film.

Before reviewing the effects of TDs on the physical properties, we briefly review the important role of TDs in the growth of nitrides, namely the formation of 'V-defects' [9]. Many nitride-based device heterostructures require reduced growth temperature. For example, InGaN layers are typically grown at ~750-800 °C in MOCVD, which is ~300 °C lower than optimal MOCVD growth conditions for GaN - the lower temperature is necessary because of the high volatility of indium. Similarly, the growth temperature for AlGaN is generally limited by reactor or heater considerations. The low growth temperatures facilitate the formation of V-defects that consist of six $\{10\bar{1}1\}$ family planes and form an inverted hexagonal pyramid, as shown schematically in Fig. 2-9. The V-defects always form at TDs, with a higher propensity for formation at mixed character TDs, but they also form at pure edge TDs.

Wu *et al.* attributed the formation of V-defects to a kinetically limited growth process in which the surface depression associated with a TD (as predicted by Frank [10]) assists in the formation of $\{10\bar{1}1\}$ facets [9]. Under kinetically limited growth conditions, the surface morphology will be dominated by the slowest growing planes, and thus in this scenario the $\{10\bar{1}1\}$ planes have a slower growth rate in the [0001] direction. Subsequent high-temperature growth of GaN will cause the V-defects to be filled and there will be no surface morphological evidence for their presence. More recently, Northrup *et al.* have performed first-principle calculations of the energies of (0001) and $\{1011\}$ planes for GaN and InGaN. Northrup has shown that V-defects at energically favorable for InGaN growth and

their formation is driven by a balance of surface energy increase (due to the increased total surface area of the six $\left\{10\bar{1}1\right\}$ planes of the V-defect relative to the area of the (0001) plane) and strain energy reduction due to the open defect volume which would otherwise have a TD. [11]

V-defects are deleterious for the growth of both optoelectronic and electronic device heterostructures. For InGaN/GaN quantum well structures, the V-defects cause the wells to be non-planar and may also lead to changes in the indium composition through a series of wells. As will be discussed later, V-defects are important sources of reverse leakage in diodes, and have been correlated to the very poor electro-static discharge (ESD) in these structures. For laser structures, the V-defects will be light scattering centers. Nitride-based high electron mobility transistor (HEMT) structures consist of AlGaN/ GaN layers. It is quite common for V-defects to form during the growth of the AlGaN cap layer. In the case of HEMT structures, there is no further nitride growth after the AlGaN layer and thus the V-defects can concentrate electric fields both at ohmic source/drain contacts and more importantly at the Schottky gate contact.

In 1997 Rosner *et al.* reported on a cathodoluminescence (CL) study on MOCVD grown n-type GaN on sapphire substrates [12]. This study involved correlated atomic force microscopy (AFM) and CL studies, in which the investigators used a combination of fiducial marks on their samples and a registered specimen stage to ensure imaging of exactly the same region by both techniques. It had been demonstrated in other studies that TDs affect the surface morphology of GaN, namely that mixed character TDs and sometimes edge TDs give rise to surface depressions. Rosner *et al.* found that the ‘pit’ features in the AFM images were strongly correlated with dark regions in the CL images. Rosner *et al.* were able to generate maps of the pit locations, corresponding to the intersection of the TDs with the film-free surface, and then calculate CL images based on known solutions for the minority carrier

concentration from a dislocation, which was assumed to be a line of non-radiative (NR) recombination centers.

Kozodoy *et al.* used the high contrast in TD density in lateral epitaxial overgrowth (LEO) structures to study the effect of TDs on reverse bias leakage currents in *p*-*n* junctions [13]. In this study, *p*-*n* junctions were formed on uncoalesced GaN LEO stripes, where the junctions were placed either over the wing region (TD density < 10^6 cm^{-2}) or over the window region (TD density ~ 10^9 cm^{-2}) on the same LEO stripe. Under reverse bias, the leakage current densities were at least three orders of magnitude higher for the window regions in comparison with the wing region, as shown in Fig. 2-10. In a similar study, Parish *et al.* fabricated AlGaN based *p*-*i*-*n* UV solar detectors on LEO GaN [14]. The diodes on the wing regions typically had six to eight orders of magnitude lower reverse bias leakage current than for diodes grown on conventional (dislocated) GaN. Additionally, the LEO-based diodes had sharper current cutoffs and much more sharply defined spectral response curves in comparison with diodes produced on conventional GaN.

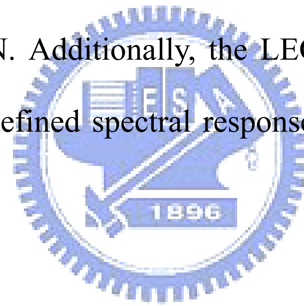

2.6 References

[1] E. H. Rhoderick and R. H. Williams, “Metal-Semiconductor Contacts”, second edition, Claarendon press, Oxford, (1988).

[2] T. Yamamoto and H. K. Yoshida, Jpn. J. Appl. Phys. **36,** L180 (1997).

[3] Q. Z. Liu and S. S. Lau, Solid-State Electron. **42**, 677 (1998).

[4] K. Schroder, “Semiconductor Material and Device Characterization”, second edition, John Wiley & Sons, Inc., (1998).

[5] Geold W. Neudeck, “The PN Junction Diode”, second edition, Addison-Wesley Publishing Company, (1989).

[6] M. S. Tyagi, “Introduction to Semiconductor Materials and Devices”, John Wiley & Sons, Inc., (1991).

[7] M. Fukuda, “Optical Semiconductor Devices”, John Wiley & Sons, Inc., (1999).

[8] X. H. Wu, L. M. Brown, D. Kapolnek, S. Keller, B. Keller, S. P. DenBaars and J. S. Speck, J. Appl. Phys. **80**, 3228 (1996).

[9] X. H. Wu, C. R. Elsass, A. Abare, M. Mack, S. Keller, P. M. Petroff, J. S. Speck and S. J. Rosner, Appl. Phys. Lett. **72** 692 (1998).

[10] F. C. Frank, Acta. Crystallogr. **4** 497 (1951).

[11] J. E. Northrup, L. T. Romano and J. Neugebauer, Appl. Phys. Lett. **74** 2319 (1999).

[12] S. J. Rosner, E. C. Carr, M. J. Ludowise, G. Girolami and H. I. Erikson, Appl. Phys. Lett. **70** 420 (1997).

[13] P. Kozodoy, J. P. Ibbetson, H. Marchand, P. T. Fini, S. Keller, J. S. Speck, S. P. DenBaars and U. K. Mishra, Appl. Phys. Lett. **73** 975 (1998).

[14] G. Parish, S. Keller, P. Kozodoy, J. P. Ibbetson, H. Marchand, P. T. Fini, S. B. Fleischer, S. P. DenBaars and U. K. Mishra, Appl. Phys. Lett. **75** 247 (1999).

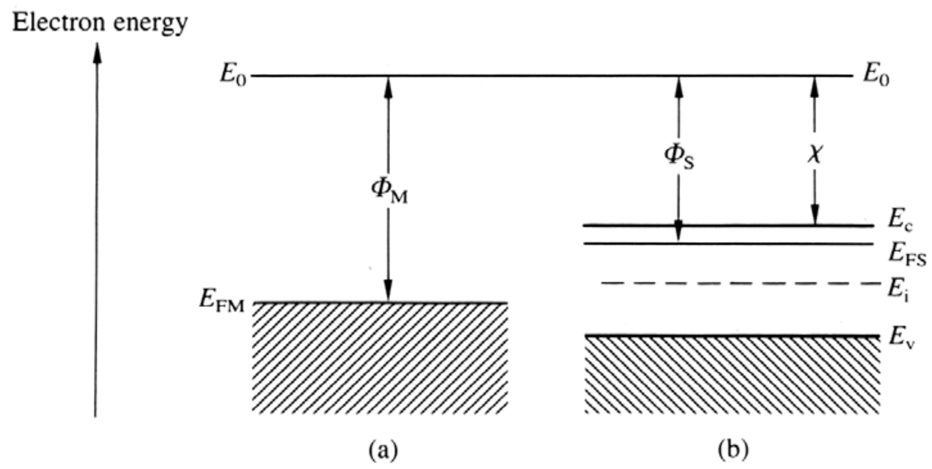

Figure 2-1 Surface-included energy band diagrams for (a) a metal and (b) *n*-type semiconductor. [1]

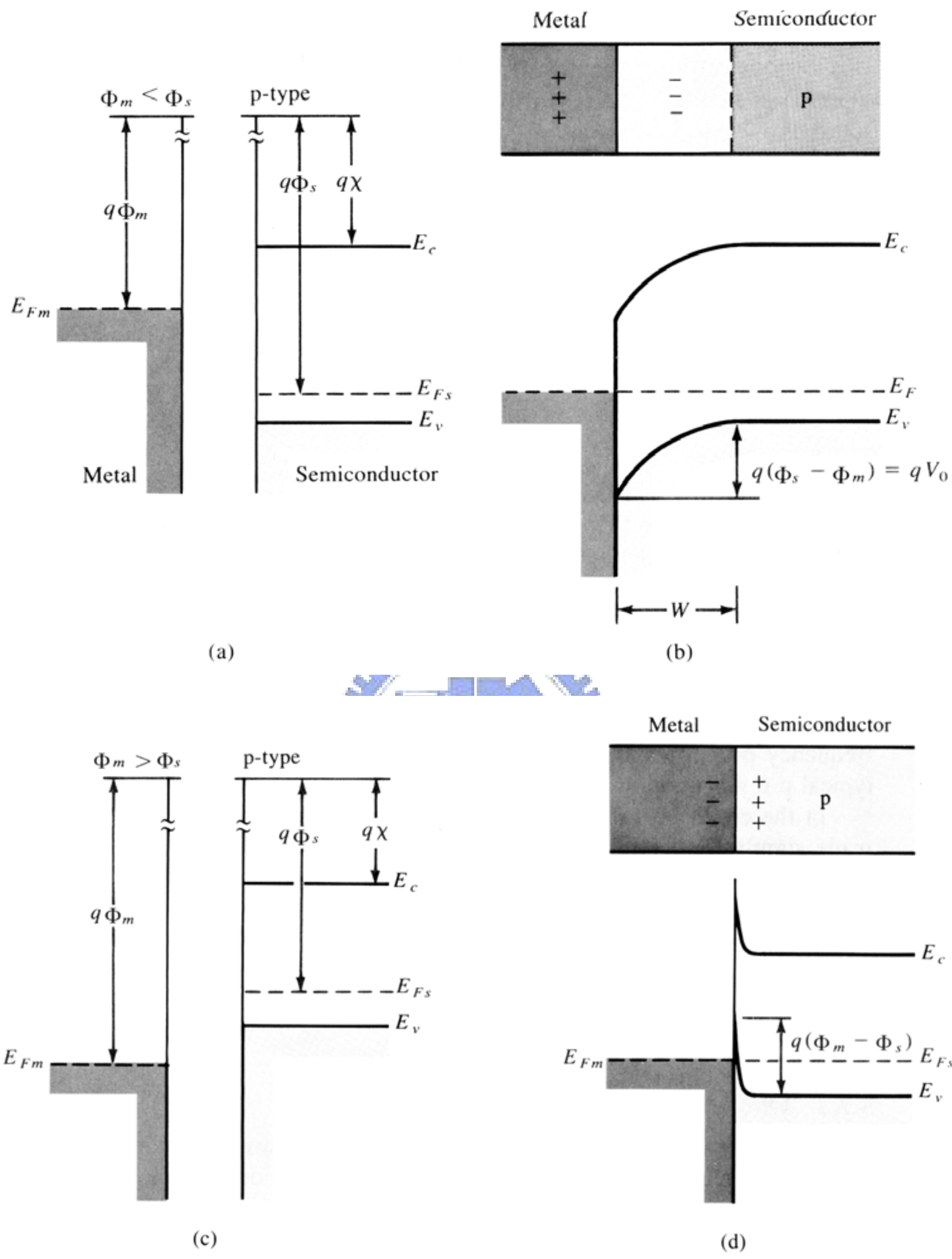

Figure 2-2 Energy band diagrams for ideal MS contacts between a metal and *p*-type semiconductor: $\Phi_M < \Phi_S$ system (a) band diagram before contact (b) under equilibrium condition after contact; $\Phi_M > \Phi_S$ system (c) band diagram before contact (d) under equilibrium condition after contact. [1]

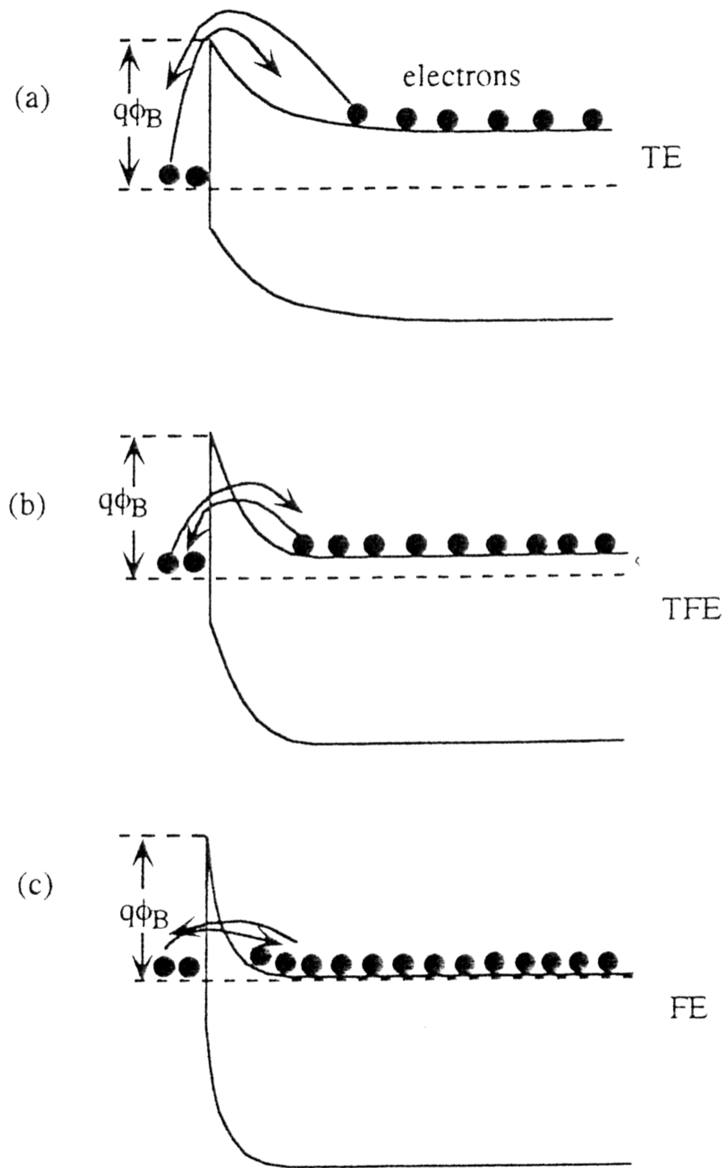

Figure 2-3 Schematic description of (a) the thermionic emission, (b) thermionic field emission, and (c) field emission (tunneling) mechanisms in an n-type semiconductor. [1]

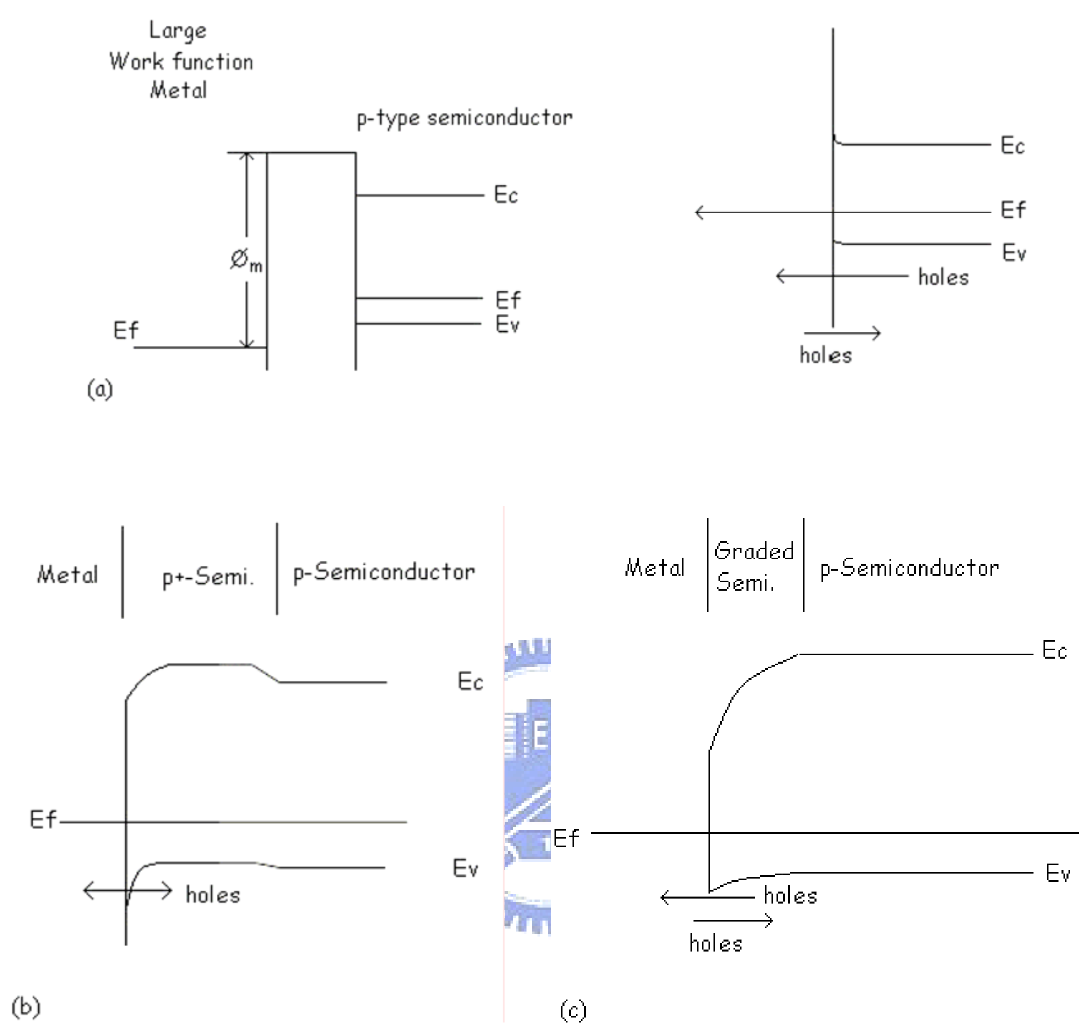

Figure 2-4 Methods of making ohmic contacts to *p*-type semiconductors (a) Use a high work function metal to minimize the Schottky barrier height. (b) Dope the semiconductor heavily to make a tunneling contact. (c) Reduce the bandgap of the semiconductor at the contact by the formation of the interfacial semiconductor layer. [3]

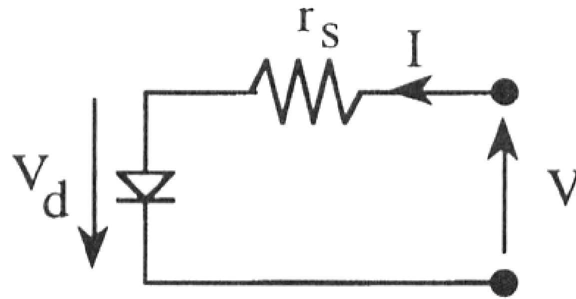

(a)

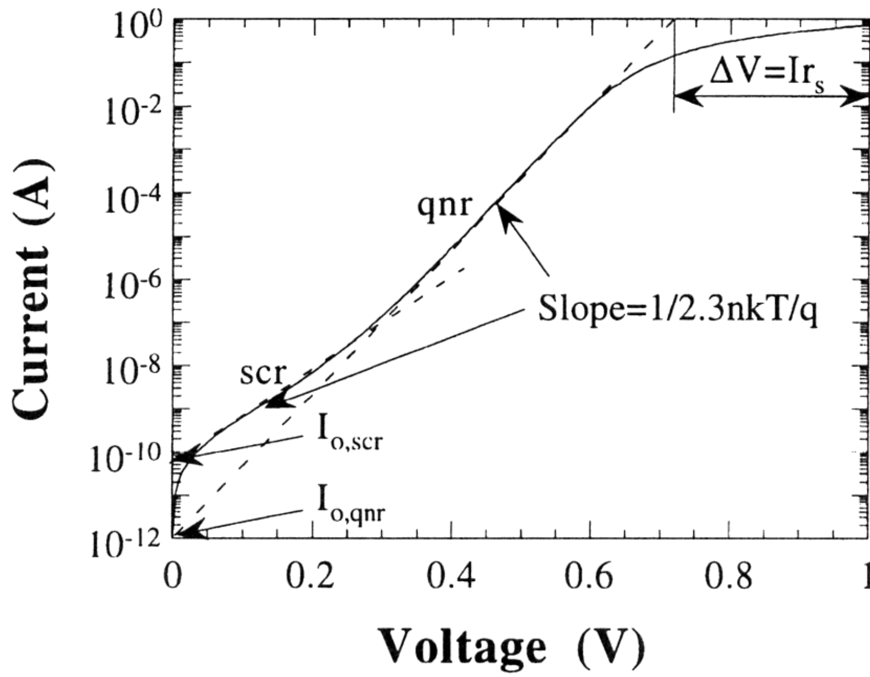

(b)

Figure 2-5 (a) Equivalent circuit of a diode, (b) log(I) versus V for a diode with series resistance, the upper dashed line is for $r_s = 0$. [4]

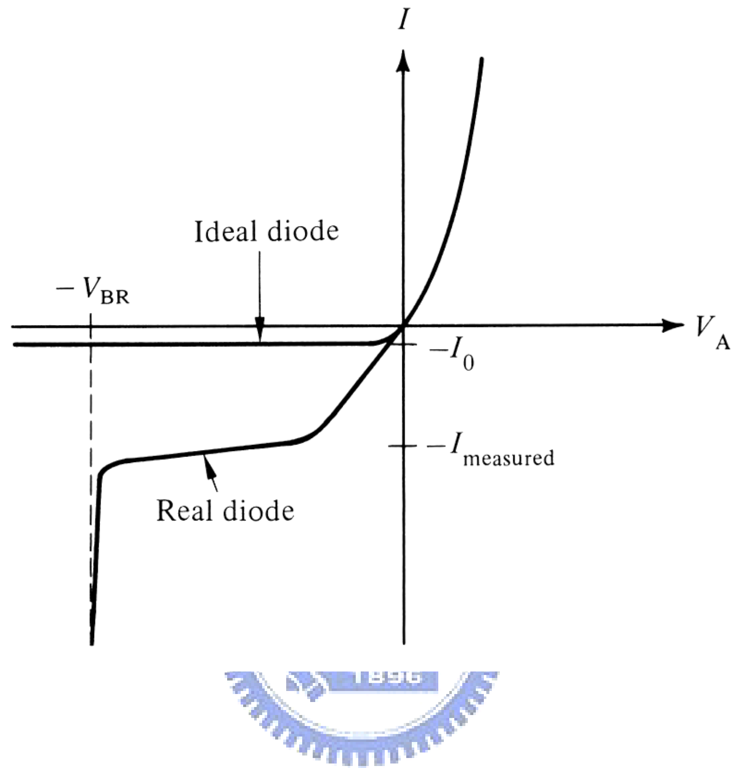

Figure 2-6 Reverse-biased in a *p*-*n* junction. [5]

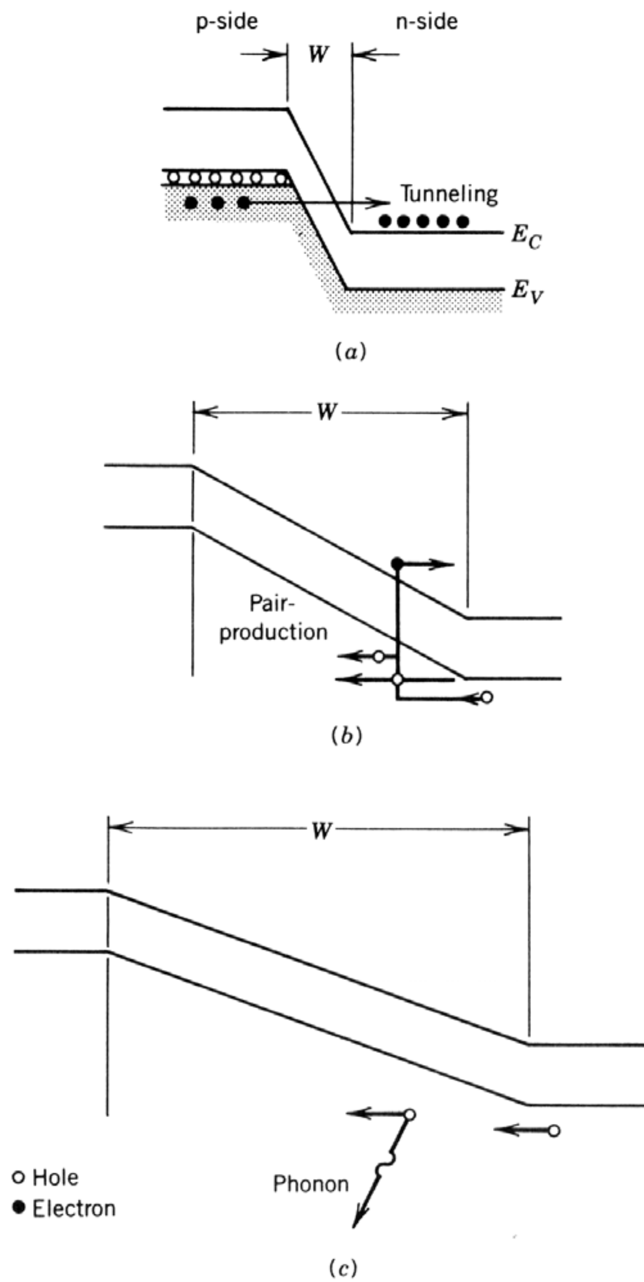

Figure 2-7 Breakdown mechanisms in a *p-n* junction diode (a) tunneling, (b) avalanche multiplication, and (c) carrier lose the gained energy to phonons and remain too cold to ionize. [6]

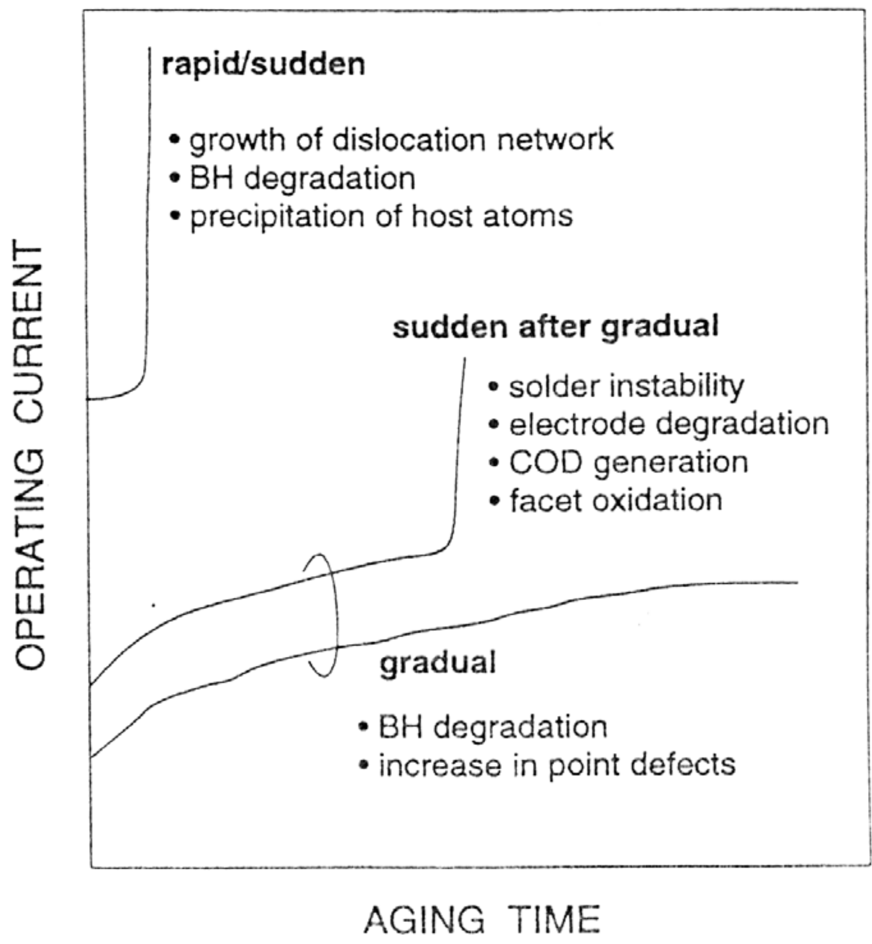

Figure 2-8 Failure modes and causes for laser diodes and LEDs (forward bias devices). [7]

Table 2-1 Main causes of and factors enhancing the failure of laser diodes and LEDs (forward bias devices). [7]

Part	Cause	Enhancement factor
Inner region	Dislocation, precipitation	Ambient temperature (heat and light), current
Facet (surface)	Oxidation	Light, moisture
Electrode	Metal diffusion, alloy reaction	Current, ambient temperature (heat)
Bonding part	Solder instability (reaction and migration)	Current, ambient temperature (heat)
Heat sink	Separation of metal	Current, ambient temperature (heat)
BH interface	Defect at BH interface	Current, ambient temperature (heat)

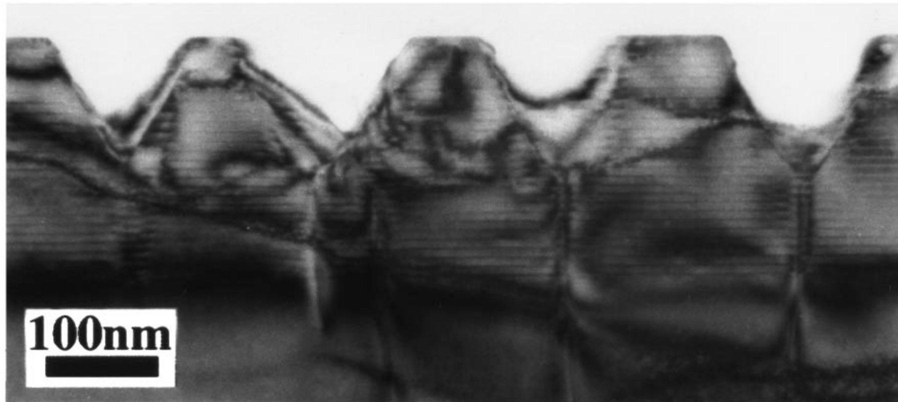

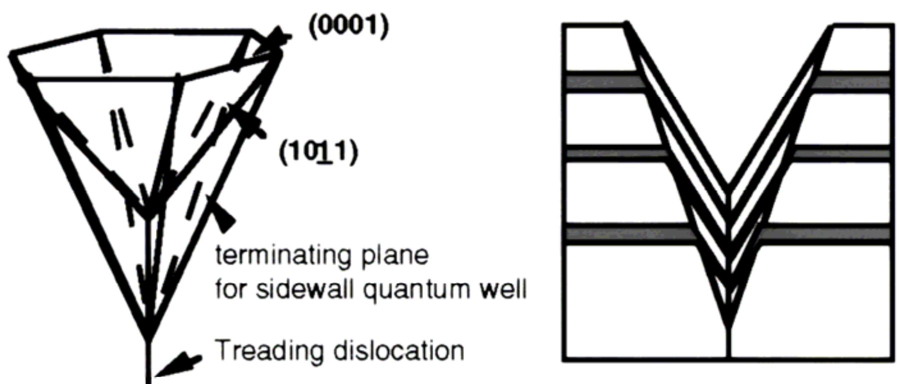

Figure 2-9 Cross-section view of V-defects in InGaN/GaN multiple quantum well structures and schematic structure of the V-defect. [9]

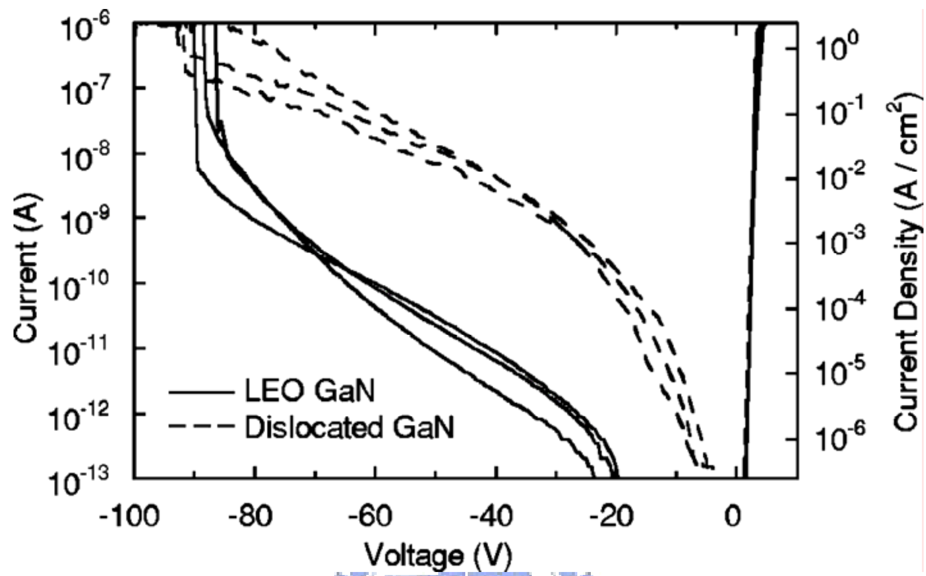

Figure 2-10 $I-V$ characteristics for several diodes on LEO GaN and on the window region (dislocated GaN). [13]

CHAPTER 3

Experiments and Analyses

3.1 Epitaxial Wafers of GaN Based LEDs

The blue GaN-based MQW LEDs wafers were grown by metal organic chemical vapor deposition (MOCVD) on c-plane (0001) sapphire substrate such as shown in Fig. 3-1. Trimethylgallium (TMGa), trimethylindium (TMIn), and ammonia (NH_3) were used as Ga, In, and N precursors respectively. The layer structure consists of a 25 nm GaN buffer layer grown at 520 °C, followed by a 1.5 μm undoped GaN layer grown at 1040 °C, a 3 μm Si-(*n*) doped GaN layer (n~2×10^{18} cm^{-3}) grown at 1040 °C, the active layer, a 0.15 μm thick Mg-(*p*) doped AlGaN cladding layer (p~5×10^{17} cm^{-3}) grown at 920 °C, and a 0.15 μm thick Mg-(*p*) doped GaN contact layer (p~7×10^{17} cm^{-3}) grown at 920 °C. The active region, consisting of several 5 nm/15 nm InGaN/GaN quantum wells grown at 760 °C is embedded in the region between *p*-type and *n*-type layers.

3.2 Processes of GaN Based LEDs

The LEDs were fabricated using standard lithography, metal coating and etching processes. Figure 3-2 shows the flow chart of GaN based LEDs process. In the first process step, the transparent contact layer (TCL) was deposited by e-beam evaporation and defined on the *p*-GaN region. The mask pattern was form by means of photoresist (PR) lithography, and then the TCL was etched by wet etching. A mesa was defined with standard photolithography and etched down into the *n*-type region by inductively coupled plasma reactive ion etching (ICP-RIE) technology. The typical ICP processing parameters were set as 2 mTorr chamber

pressure, 450 W ICP power, 170 W RF power, 40 sccm Cl_2 (or 40 sccm Cl_2 + 5 sccm BCl_3), 25 °C temperature, and a dc bias of -160 V. The ICP power and bias power source with RF frequency were set at 13.56 MHz. After ICP dry etching, the PR was removed with PR dissolvent and acetone. And then TCL metals were annealed at 600 °C in air atmosphere for 15 min. For *n*-type GaN, low resistance ohmic contacts around 10^{-5}~10^{-8} Ω cm^2 range have been obtained using Ti/Al metals series. [1] The Ti/Al/Ti/Au metals for the *n*-contact (10 nm/50 nm/100 nm/150 nm) and bonding pad (10 nm/400 nm/150 nm/800 nm) were deposited with e-beam evaporation and performed the metal lift-off, followed by the annealing process at 300 °C with continuous nitrogen flow for 5 min. All the annealing processes were performed in a furnace. Figure 3-3 shows the typical chip structure of the GaN based LEDs.

3.3 Circular Transmission Line Model (CTLM)

The circular transmission line model (CTLM) was used to measure the specific contact resistance (ρ_c), which is the resistance at the interface between the metal and the semiconductor. [2] The structure is shown in Fig. 3-4. The inner radius of the circle is 100 μm, and the gap spacing from the smallest to the largest are 5, 10, 20, 30, and 40 μm.

For the four probe technique, the two probes apply current and the other two probes measure the voltage drop. According to Marlow and Das [3], the relation between the applied current and the measured potential drop across the separation *d* is:

$$\Delta V = \frac{iR_s}{2\pi}\left[\ln\left(\frac{r_1}{r_1 - d}\right) + L_T\left(\frac{1}{r_1} + \frac{1}{r_1 - d}\right)\right] \qquad (3\text{-}1)$$

where R_s is the sheet resistance, and r_1 is the radii of the outer circle. L_T is the transfer length given by

$$L_T = \sqrt{\frac{\rho_c}{R_s}} \qquad (3\text{-}2)$$

where ρ_c is the specific contact resistance. From Eq. 3-1 we can plot the total resistance as a function of the gap spacing to obtain a non-linear curve due to the logarithm term; we then employ the least squares method to fit of the data to calculate R_s and L_T. The product of ($L_T \times 2\pi$) gives the effective contact area where current flows through. The specific contact resistance then can be extracted.

$$\rho_c = R_c \times L_T \times 2\pi \tag{3-3}$$

where the resistance R_c between contacts is

$$R_c = \frac{R_s}{Z}(d + 2L_T) \tag{3-4}$$

$$Z = 2\pi L \tag{3-5}$$

$$\rho_c = R_s \times L_T^{\ 2} \tag{3-6}$$

where the $2L$ is the radius inner circular contact, and d is the gap spacing.

However, in many of our *I-V* measurement, non-linear *I-V* curves are observed. The non-linear *I-V* curves lead to a change in the measured total resistance, which influences the calculated specific contact resistance as given in Eq. 3-1. In fact, only a linear *I-V* curve allows us to extra a true specific contact resistance using the CTLM approach, and in the strictest sense, the term specific contact resistance applies to the contact's resistance applies to the contact's resistance at zero bias. However, all the calculations in this thesis were performed by using data at 1 mA from the *I-V* curves, and we use the term "effective specific contact resistance".

The circular test structure has one main advantage. It is not necessary to isolate the diffused or implanted layer. In the original method that uses rectangular contacts, current can flow from contact to contact through the region beyond the structure in the linear arrangement (if it is not isolated). In the circular case, current can only flow from the center to the surrounding contact and no other path is possible.

3.4 Measurement of Carrier Concentration by Capacitance-Voltage Method

The capacitance-voltage (*C*-*V*) technique relies on the fact that width of a reverse-biased space-charge region (scr) of a semiconductor junction device depends on applied voltage. This scr width dependence on voltage lies at the heart of the *C*-*V* technique. The *C*-*V* profiling method has been used with Schottky barrier diodes using metal and liquid electrolyte contacts, p-n junction, MOS capacitors, and MOSFETs. The depth profile is generally measured by *C*-*V* method, which was established by Kennedy *et al.*. [4] The measurement of the profile of the interface is troublesome because of the abrupt change of the carrier concentration. For the *C*-*V* measurement, a Schottky electrode is formed on the sample, and correlation between the applied voltage and the capacitance of a depletion layer is measured. The carrier concentration $N(x)$ and the thickness x of the depletion layer are calculated using Eq. 3-7 and 3-8, respectively.

$$N(x) = \frac{2}{qK_s\varepsilon_0 A^2 d(1/C^2)/dV} \tag{3-7}$$

$$x = \frac{K_s\varepsilon_0 A}{C} \tag{3-8}$$

where the charge of an electron is q, the voltage applied to the depletion layer V, the capacitance of the layer C, the area of the electrode A, semiconductor dielectric constant K_s, and permittivity of free space ε_0 (8.854×10^{-14} F/cm).

The capacitance is determined by superimposing a small-amplitude ac voltage v on the dc voltage V. The ac voltage typically varies at frequencies of 10 kHz to 1MHz with amplitude of 10 to 20 mV, but other frequencies and other voltages can be used. In this thesis, the *C*-*V* measurements have been performed at -5 to 5 V, and 100 Hz to 1 MHz.

3.5 Field Emission Scanning Electron Microscopy

Scanning electron microscopy (SEM) is one of the well-known and most widely used surface analytical techniques. Field emission scanning electron microscopy (FESEM) equipped with a field emission cathode in the electron gun of a SEM provides narrower probing beams at low as well as high electron energy, resulting in both improved spatial resolution and minimized sample charging and damage. High-resolution images of surface topography, with excellent depth of field are produced using a highly focused scanning electron beam. The primary electrons enter a surface with the energy of 0.5 ~ 30 keV, and generate many low energy secondary electrons. The intensity of these secondary electrons is largely governed by the surface topography of the sample. An image of the sample surface can thus be constructed by measuring secondary electron intensity as a function of the position of the scanning primary electron beam. We used the FESEM, Hitachi S-4000, to obtain the surface and sidewall morphology.

3.6 Transmission Electron Microscopy

The transmission electron microscope (TEM), developed in the 1932, was originally used for highly magnified sample images. Operating on the basic principles of the optical microscope, the TEM takes advantage of the much shorter wavelengths of electron beams versus light beams, providing resolving powers on the order of 0.2 nm rather than 200nm for the optical microscope. Because the wavelength of electrons is much smaller than that of light, the optimal resolution attainable for TEM images is many orders of magnitude better than that from an optical microscope. For the crystallographer, metallurgist or semiconductor research scientist, thus TEM can reveal the finest details of internal structure. Materials for TEM must be specially prepared to thickness that allow electrons to transmit through the sample. We

utilities TEM (JEOL JEM-2010 microscope operated at 200 kV) for examine the sample structure, defects (dislocations), and dislocations.

3.7 Photoluminescence

Photoluminescence (PL) is one of the most sensitive nondestructive methods of analyzing both intrinsic and extrinsic semiconductor properties. The method is particularly suitable for characterization of the centers that control the electrical properties of the layers. PL has the advantage of the ability to discriminate between species involved in radiative recombination and can provide simultaneous information on many type centers. In particular, basic assessment of a semiconductor usually requires measurements at low temperatures, so the sample must be place in a cryostat. Low temperatures are necessary for two principal reasons. First, specific information about the centers, the donors and acceptors, which promote electrical conductivity, can be obtained only when the electrical carriers are frozen out in these centers. Once the electrical carriers are thermally liberated, the impurities or defects that released them reveal their presence only through some inhibition of carrier mobility. The second advantage of low temperature is the dramatic reduction of spectral broadening due to vibration processes. The PL measurements of GaN thin films were performed by using a He-Cd laser emitting at 325 nm with Bio-Rad rpm2000.

3.8 Hall Effect Measurement

The importance of Hall effect is underscored by need to determine accurately carrier density, electrical resistivity, and the mobility of carriers in semiconductors. The Hall effect provides a relatively simple method for doing this. Because of its simplicity, low cost, and fast turnaround time, it is an indispensable characterization technique in the semiconductor

industry and in research laboratories. The basic physical principle underlying the Hall effect is the Lorentz force. We usually make the Hall effect measurement by two ways (1) Hall bar and (2) van der Pauw technique determined by the sample shape, contact geometry, and measurement method. In our studies the van der Pauw technique is usually used. We can make the room temperature Hall effect measurement with Bio-Rad HL 5500PC.

3.9 References

[1] S. N. Mohammad, J. Appl. Phys. **95**, 7940 (2004).

[2] K. Schroder, "Semiconductor Material and Device Characterization", second edition, John Wiley & Sons, Inc., (1998).

[3] G. S. Marlow and M. B. Das, Solid-State Electron. **25**, 91 (1982).

[4] D. P. Kennedy, P. C. Muriey and W. Kleinfelder, IBM J. Res. Dev., 399 (1968).

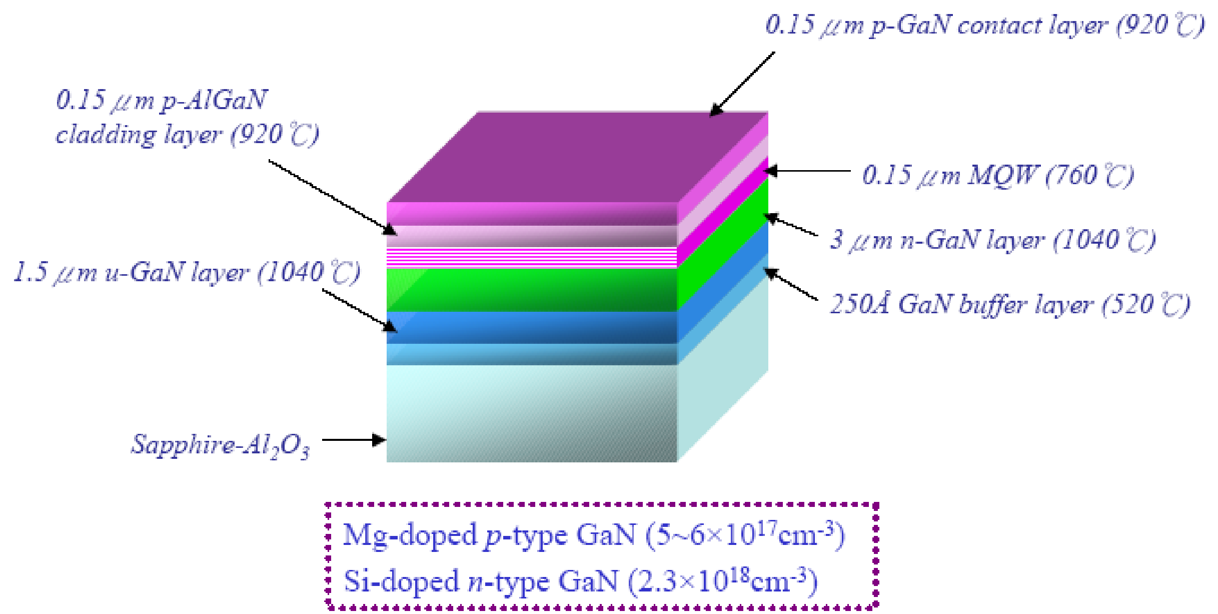

Figure 3-1 The epitaxial structure of the GaN based LEDs.

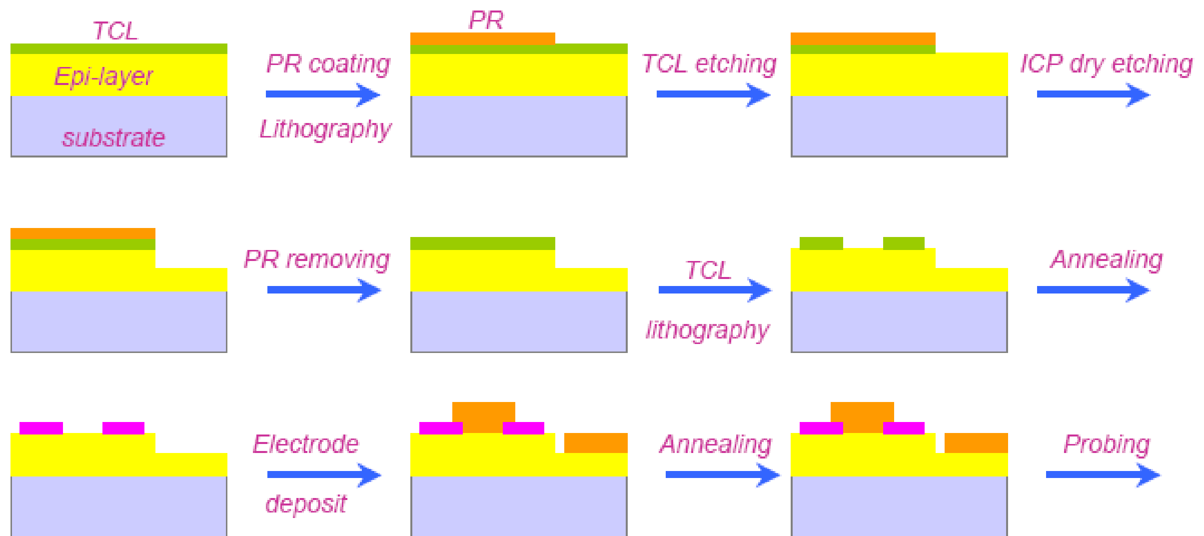

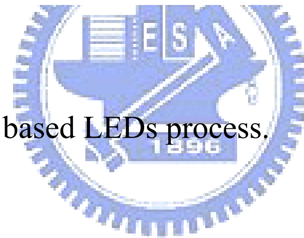

Figure 3-2 The flow chart of GaN based LEDs process.

Electrode pad metals: (by e-beam evaporation)

Ti / Al / Ti / Au (100 Å / 500 Å / 1000 Å / 1500 Å)

Alloy temperature and time:

250℃ / 10min in a furnace flowing N_2

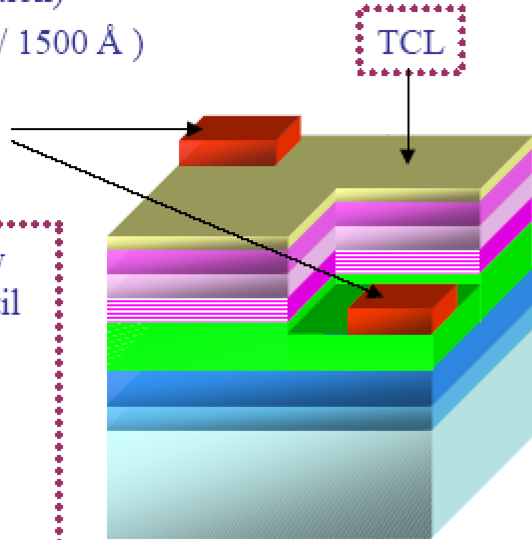

❖ The surface of *p*-GaN layer was few partially etched by ICP dry etching until *n*-GaN layer was exposed.

❖ Cl_2: 40 sccm

Pressure: 2 mT

ICP power: 450 W

RF power: 170 W

Etch time: 2 min

Figure 3-3 The chip structure of the GaN based LEDs.

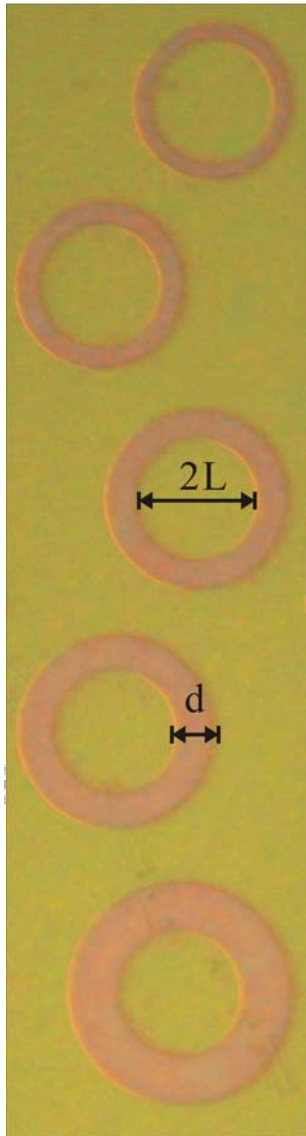

Figure 3-4 Circular transmission line geometry test structure.

CHAPTER 4

Effect of Thermal Annealing on Ni Film/Mg-Doped GaN Layer

4.1 Introduction

GaN-based materials are important wide direct bandgap semiconductors for optoelectronic applications. One of the problems of GaN-based devices is the low hole concentration of Mg-doped GaN, which makes it difficult to obtain a contact resistance lower than 10^{-4} Ω cm^2. To make ohmic contact on *p*-type GaN, high work function metals such as Ni, Pd, and Pt have been applied. A specific contact resistance of around 10^{-2}~10^{-6} Ω cm^2 can be achieved in the Ni/Au [1, 2], Ni/Pt/Au [3], Ni/Pd/Au [4], Ni/AuBe [5], Ni/ZnO [6], and Ni-Mg (La or Zn) solid solution/Au series. [7-9] Many studies concerning Ni have been carried out. Thus, it is important to understand the interfacial reactions between Ni and GaN.

Since Ni has been used for Ni/Au ohmic contact to *p*-type GaN, the metallurgy of the Ni/GaN system has been researched. [10-14] Guo *et al.* reported that the nickel nitrides Ni_3N and Ni_4N were formed at the interface of Ni and *n*-type GaN after annealing above 200 ºC. [10] Chen *et al.* showed that a *p*-type GaN/Ni/Au system after thermal treatment at 500 ºC in air was mainly composed of a mixture of crystalline nickel oxide (NiO), Au, and amorphous Ni-Ga-O phases. A microstructural examination indicated that crystalline NiO and/or the amorphous Ni-Ga-O phases might significantly affect the low resistance ohmic contact to *p*-type GaN. [12] Some researchers reported that Ga atoms diffused out from the GaN substrate and dissolved in the Au-Ni solid solution, leading to generation of Ga vacancies below the contact. They suggested that Ga vacancies play a role in increasing the net hole concentration. [13, 14] Furthermore, Waki *et al.* confirmed that Ni film significantly enhances

hydrogen dissociation and out-diffusion from Mg-doped GaN film. [15-17] Figure 4-1 shows a schematic diagram of the hydrogen desorption process. In this figure, simply four steps are taken into account: (i) dissociation, (ii) diffusion, (iii) recombination, and (iv) desorption. [16] They achieved *p*-type conduction in GaN by annealing in a N_2 ambient at a substrate temperature as low as 200 ºC. The enhancement of hydrogen desorption owing to the Ni was confirmed by secondary ion mass spectroscopy (SIMS) measurements as shown in Fig. 4-2. [15] Thermal desorption spectroscopy (TDS) measurements revealed that the hydrogen desorption rate was considerably increased by the existence of the Ni film at approximately 200 ºC and the low-temperature desorption had an activation energy of 1.3 eV. In addition, they found that the ionization energies of the Mg acceptors in the GaN activated with the Ni layers decreased from 170 to 118 meV as the acceptor concentration increased.

Although there have been many experimental investigations on the Ni/GaN system, the influences of the reaction between Ni and *p*-type GaN need further understanding. In the present study, Mg-doped GaN wafers were activated with and without Ni film, respectively. Then, we investigated the variation of the interface between Ni and *p*-type GaN after thermal activation. The phases of compounds were observed by x-ray diffraction (XRD) analysis. Room temperature capacitance-voltage (*C-V*) and Hall effect measurement results are analyzed to obtain the effective acceptor concentrations. From photoluminescence (PL) measurements, Mg-doped GaN emissions have been observed at 15K.

4.2 Experiments

4.2.1 Preparation of Mg-doped GaN wafers

The Mg-doped GaN wafers were grown on c-plane sapphire substrates by metal organic chemical vapor deposition (MOCVD) with a magnesocene Cp_2Mg solution source. The layer

structure consists of a GaN buffer layer, followed by a 1.5 μm undoped GaN layer, and a 1.5 μm Mg-(*p*)-doped GaN layer.

4.2.2 Activation of Mg-doped GaN wafers

The as-grown wafers were cut into approximately 5 mm square pieces, and then cleaned in organic solvents, rinsed in deionized (DI) water, immersed in 1:1 HCl:DI water solution, and dried in compressed N_2 gas for 5 min, respectively. Some of these as-grown samples were deposited 30 nm Ni film on the *p*-type GaN layer by e-beam evaporation. The samples were activated without Ni film (samples A) and with Ni film (samples B) from 400 to 700 ºC in a quartz tube furnace in an air ambient for 15 min. For comparison, the same Ni film (30 nm thick) was also deposited on glass substrates and the same annealing procedure was performed.

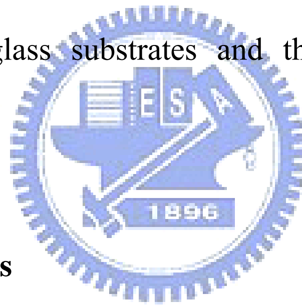

4.2.3 Measurements and analyses

After activation, XRD with Cu K_α radiation was used to study the phases formed by the reactions of Ni and *p*-type GaN during thermal annealing. After XRD analysis, samples B were immersed in aqua regia for 30 min to remove the residual Ni film and certain Ni-containing compounds on the surfaces, for measurements. The electrical and optical properties of the samples were measured by Hall effect (Biorad HL5500PC), *C*-*V* (HP 4284A LCR meter) and PL spectrum (Bio-Rad rpm2000) measurements. The PL measurements were performed at 15K. A He-Cd laser emitting at 325 nm was used as an excitation source. For the Hall effect measurements, Ni/Au (50 nm/80 nm) electrodes were deposited by e-beam evaporation and then annealed at 500 ºC in a rapid thermal annealing (RTA) system for 1 min to obtain ohmic contact. Double Schottky contact electrodes were used to measure *C*-*V*

characteristics at 100 kHz to exclude the influence of temperature during alloying contact metals. The Schottky electrodes Ti/Al/Ti/Au (10 nm/50 nm/100 nm/150 nm) were deposited by e-beam evaporation and masked to form 0.3 mm-diameter circular dots.

4.3 Results and Discussions

4.3.1 Results of XRD analysis

Figure 4-3 shows the XRD spectra of the *p*-type GaN structure after activation with Ni film at 400, 500, and 600 ºC. The peaks related to GaN, Ni, NiO, Ni_3N and Ni_4N were clearly detected. These results indicate that the Ni film transformed to NiO, Ni_3N and Ni_4N during thermal treatment in air. In addition, the XRD analysis of Ni film on glass after annealing was also performed, as shown in Fig. 4-4. We found that the Ni film on glass only transformed to NiO in atmospheric ambient. At a high annealing temperature, the Ni film would transform to NiO film completely. Comparing Fig. 4-3 with Fig. 4-4, nickel nitride was formed from the Ni and *p*-type GaN reaction. For the 400 ºC annealing process, peaks related to Ni_3N and Ni_4N can be observed. For the temperature of 500 ºC, NiO was formed. When the temperature was increasing to 600 ºC, both NiO and Ni_3N show strong signals. The specie Ni_4N almost vanished at 600 ºC. Thus, Ni_3N and NiO show better thermal stability than Ni_4N.

By immersing the 600 ºC sample in aqua regia, the residual Ni film and certain Ni-containing compounds on surface were removed. Figure 4-5 shows the XRD result. It can be observed that the Ni and NiO were both removed while the Ni_3N remains. Thus, the Ni may diffuse and react with the *p*-type GaN and shows a chemically stable behavior.

4.3.2 Effective carrier concentrations and mobility by Hall effect measurement

Figure 4-6(a) shows the effective carrier concentrations, of the samples activated at various temperatures with and without Ni film, obtained from Hall effect measurements. The samples activated with Ni film obtain higher effective carrier concentrations than those activated without Ni film. The differences are clear, especially below 600 ºC. The highest carrier concentration of 2.5×10^{17} cm^{-3} with a mobility of 4.9 cm^2 V^{-1} s^{-1} was obtained at the activating temperature of 700 ºC with Ni film. This carrier concentration is double that of the sample without the Ni film at this activating temperature. An effective concentration of 1×10^{17} cm^{-3} was achieved after activation at 400 ºC with Ni film, and it is higher than that for conventional film activated at 600 ºC. Figure 4-6(b) shows the corresponding mobility. For the samples without Ni film, an increase in mobility as the annealing temperature increases from 500 ºC to 600 ºC can be observed. A high annealing temperature may improve the crystal quality. For the samples with Ni film, the mobility is relatively high even at a temperature less than 500 ºC. Thus, the Ni species such as Ni_3N or Ni_4N probably act as catalysts to enhance the hydrogen dissociation and improve the crystal quality. At an annealing temperature above 600 ºC, Ni in-diffusion may be occurred and thus worse crystal quality can be expected.

4.3.3 Effective carrier concentrations by *C-V* method

Figure 4-7 shows the profiles of effective carrier concentrations deduced from *C-V* measurements of samples activated at 600 ºC without and with Ni film. Flat profiles were observed for the samples activated without Ni film, indicating that the carriers were uniformly distributed. For the samples activated with Ni film, the shapes of the effective carrier concentration profiles were also obtained. The carrier concentrations decreased rapidly from $\sim10^{21}$ to $\sim10^{17}$ cm^{-3} within 60nm, suggesting a higher effective carrier concentration near the surface region. Comparing Fig. 4-6(a) with Fig. 4-7, the high carrier concentration region in

the sample surface should be related to the Ni diffusion into the Mg-doped GaN epitaxial layer.

For another research group, SIMS results showed that H concentration was reduced, a certain amount of Ni atoms seemed to penetrate into the GaN epitaxial layers, and the Mg atoms were not dragged out and accumulated in the subsurface region after activation with Ni film. [18] Figure 4-8 and 4-9 show the SIMS depth profiles of Ni and Mg, respectively. Wang *et al.* suggested that Ni atoms not only enhance hydrogen desorption but also diffuse into the Mg-doped GaN layers probably to form Ni-compound materials during activating with Ni film. [18] According to their report [18] and our results, Ni in-diffusing and Ni nitride formation may increase the number of defects and vacancies at the surface region during the high temperature activating process. These impurities (including defects, vacancies and Ni_3N) could increase the effective carrier concentrations in this study.

4.3.4 Results of photoluminescence measurement

Typical PL spectra at 15K of the samples after activating with and without Ni film are shown in Fig. 4-10. The peaks of both 3.2 and 2.9 eV were obtained, and the red-shift trend of the spectra with Ni catalyst activation is observed. The samples of lower activation temperature (below 500 ºC) have the peak near 3.2eV, indicating the existence of the Mg-H complexes. The PL peaks of the samples activated above 600 ºC shift to 2.9eV, revealing that the Mg-H complexes have been dissociated. Usually, the peak position of this emission line shifts toward lower energy as the doping concentration is increased. [19, 20] The surface decomposition during activating with Ni film can result in the degradation of the PL signal. For moderately Mg-doped GaN, strong donor-acceptor pair (DAP) emission at 3.2 eV is observed where the donor and acceptor potentials are both shallow. For the emission at around 2.8~2.9 eV of DAP, Kaufmann *et al.* suggested that the acceptor is isolated

substitutional Mg (Mg_{Ga}) while the spatially separated, deep donor is attributed to a nearest-neighbor association of an Mg_{Ga} acceptor with a nitrogen vacancy, formed by self-compensation. [19] Furthermore, Shahedipour *et al.* also explained that the deep donor defect responsible for the 2.8 eV band is attributed to a nitrogen vacancy complex. [21] Thus, we consider that nitrogen vacancies could be produced via Ni in-diffusing and Ni nitride formation during the activating process.

4.4 Conclusions

In conclusion, the influences of the reaction between Ni and *p*-type GaN have been studied. We suggest that Ni atoms not only enhance hydrogen desorption but also diffuse into Mg-doped GaN layers to form Ni-compound materials. XRD analyses indicated that Ni film on *p*-type GaN transforms to NiO and Ni_3N during thermal treatment in air. We also suggest that Ni in-diffusion occurs and Ni nitride is formed resulting in the formation of defects and vacancies during the activation process. These impurities (including Ni nitride, nitrogen vacancies and other defects) may provide an increase in the effective carrier concentrations in the vicinity of the surface. For the Ni series contact, the lower specific contact resistance may be attributed to the results of this study.

4.5 References

[1] J. K. Ho, C. S. Jong, C. C. Chiu, C. N. Huang and K. K. Shih, Appl. Phys. Lett. **74**, 1275 (1999).

[2] J. K. Ho, C. S. Jong, C. C. Chiu, C. N. Huang, K. K. Shih, L. C. Chen, F. R. Chen and J. J. Kai, J. Appl. Phys. **86**, 4491 (1999).

[3] J. S. Jang, K. H. Park, H. K. Jang, H. G. Kim and S. J. Park, J. Vac. Sci. Technol. **B16**, 3105 (1998).

[4] C. F. Chu, C. C. Yu, Y. K. Wang, J. Y. Tsai, F. I. Lai and S. C. Wang, Appl. Phys. Lett. **77**, 3423 (2000).

[5] L. C. Chen, C. Y. Hsu, W. H. Lan and S. Y. Teng, Solid-State Electron. **47**, 1843 (2003).

[6] J. O Song, K. K. Kim, S. J. Park and T. Y. Seong, Appl. Phys. Lett. **83**, 479 (2003).

[7] J. O Song, D. S. Leem and T. Y. Seong, Appl. Phys. Lett. **83**, 3513 (2003).

[8] J. O Song, D. S. Leem, J. S. Kwak, S. N. Lee, O. H. Nam, Y. Park and T. Y. Seong, Appl. Phys. Lett. **84**, 1504 (2004).

[9] J. O Song, D. S. Leem and T. Y. Seong, Appl. Phys. Lett. **84**, 4663 (2004).

[10] J. D. Guo, F. M. Pan, M. S. Feng, R. J. Guo, P. F. Chou and C. Y. Chang, J. Appl. Phys. **80**, 1623 (1996).

[11] H. S. Venugopalan, S. E. Mohney, B. P. Luther, S. D. Wolter and J. M. Redwing, J. Appl. Phys. **82**, 650 (1997).

[12] L. C. Chen, F. R. Chen, J. J. Kai, L. Chang, J. K. Ho, C. S. Jong, C. C. Chiu, C. N. Huang, C. Y. Chen and K. K. Shih, J. Appl. Phys. **86**, 3826 (1999).

[13] J. K. Kim, J. H. Je, J. L. Lee, Y. J. Park and B. T. Lee, J. Electrochem. Soc. **147**, 4645 (2000).

[14] H. W. Jang, S. Y. Kim and J. L. Lee, J. Appl. Phys. **94**, 1748 (2003).

[15] I. Waki, H. Fujioka, M. Oshima, H. Miki and A. Fukizawa, Appl. Phys. Lett. **78**, 2899

(2001).

[16] I. Waki, H. Fujioka, M. Oshima, H. Miki and M. Okuyama, J. Appl. Phys. **90**, 6500 (2001).

[17] Y. Kamii, I. Waki, H. Fujioka, M. Oshima, H. Miki and M. Okuyama, Appl. Surf. Sci. **190**, 348 (2002).

[18] S. M. Wang, C. H. Chen, S. J. Chang, Y. K. Su and B. R. Huang, Mater. Sci. Eng. **B117**, 107 (2005).

[19] U. Kaufmann, M. Kunzer, M. Maier, H. Obloh, A. Ramakrishnan and B. Santic, Appl. Phys. Lett. **72**, 1326 (1998).

[20] J. K. Sheu, Y. K. Su, G. C. Chi, B. J. Pong, C. Y. Chen, C. N. Huang and W. C. Chen, J. Appl. Phys. **84**, 4590 (1998).

[21] F. Shahedipour and B. W. Wessels, Appl. Phys. Lett. **76**, 3011 (2000).

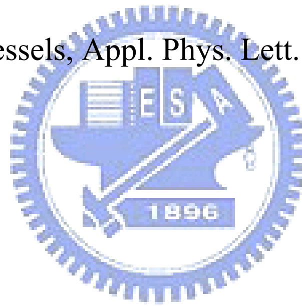

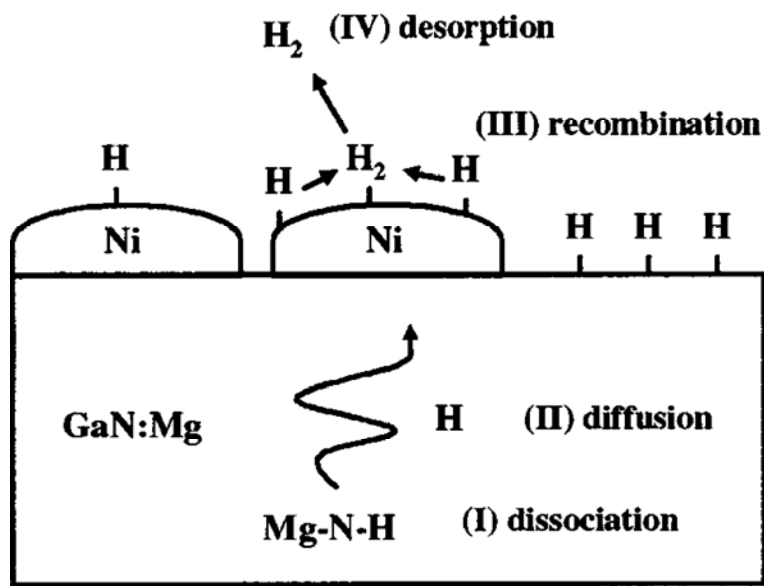

Figure 4-1 Schematic diagram of hydrogen desorption process of Mg-doped GaN with the Ni catalyst. [16]

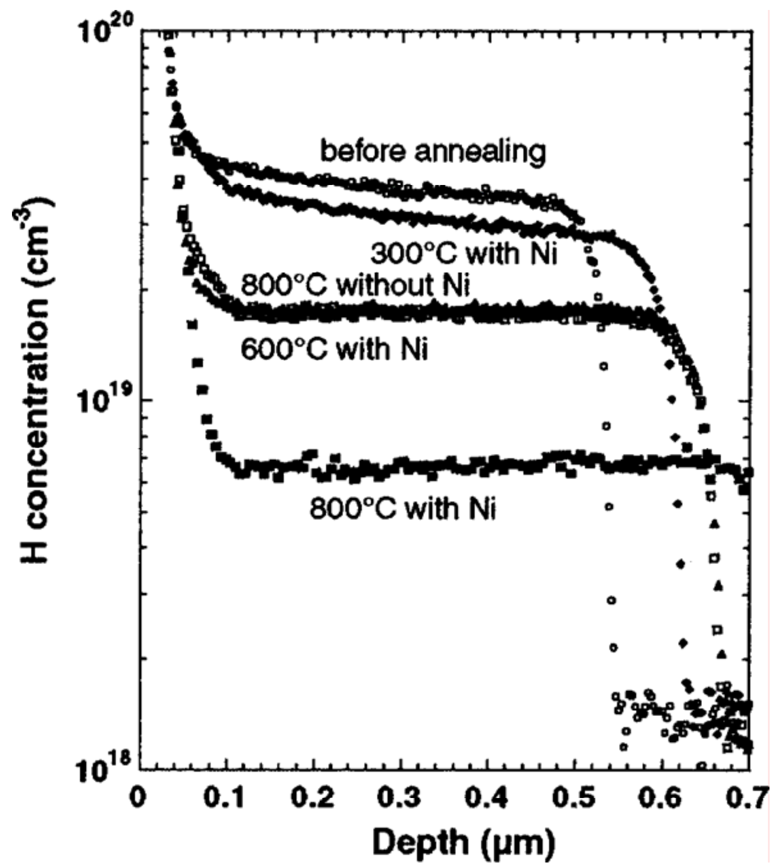

Figure 4-2 SIMS profiles of H concentration for the samples annealed at various temperatures with and without Ni film. All samples were annealed in a N_2 ambient for 10 min. [15]

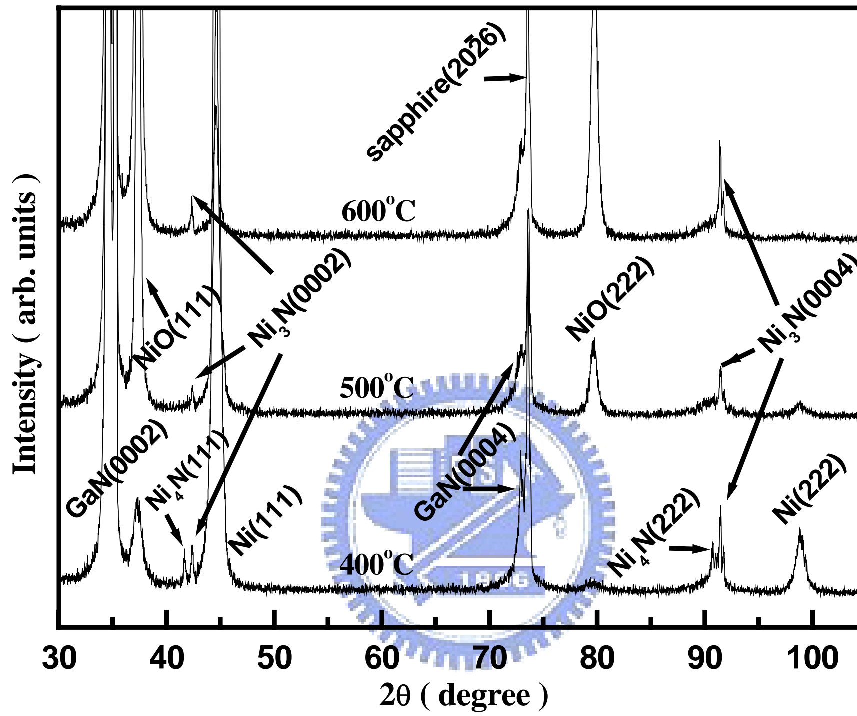

Figure 4-3 XRD spectra of Mg-doped GaN structure after activation with Ni film at 400, 500 and 600 ºC in air ambient.

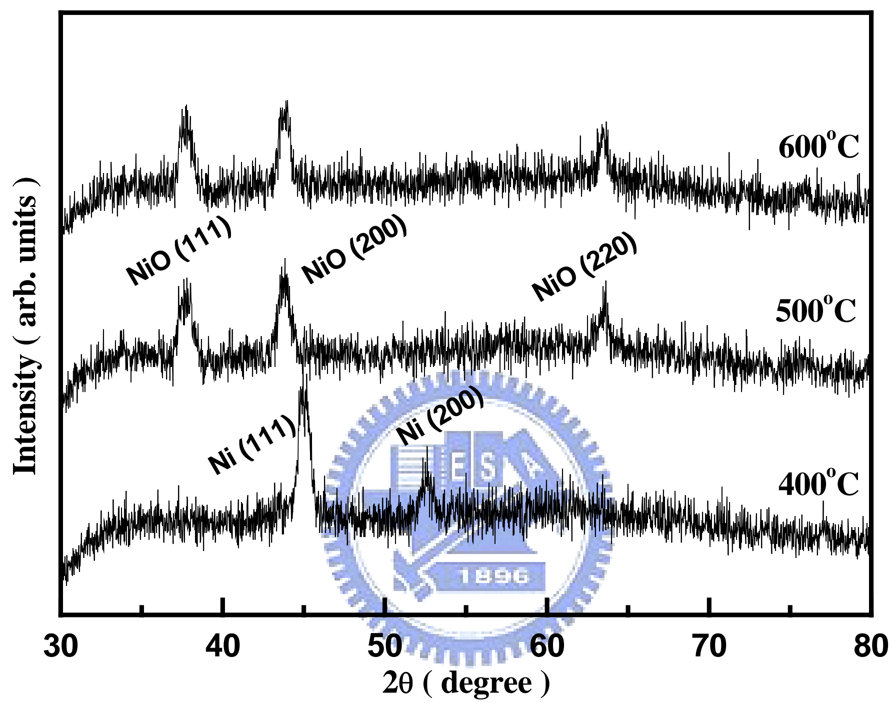

Figure 4-4 XRD spectra of Ni film on glass after annealing in air ambient.

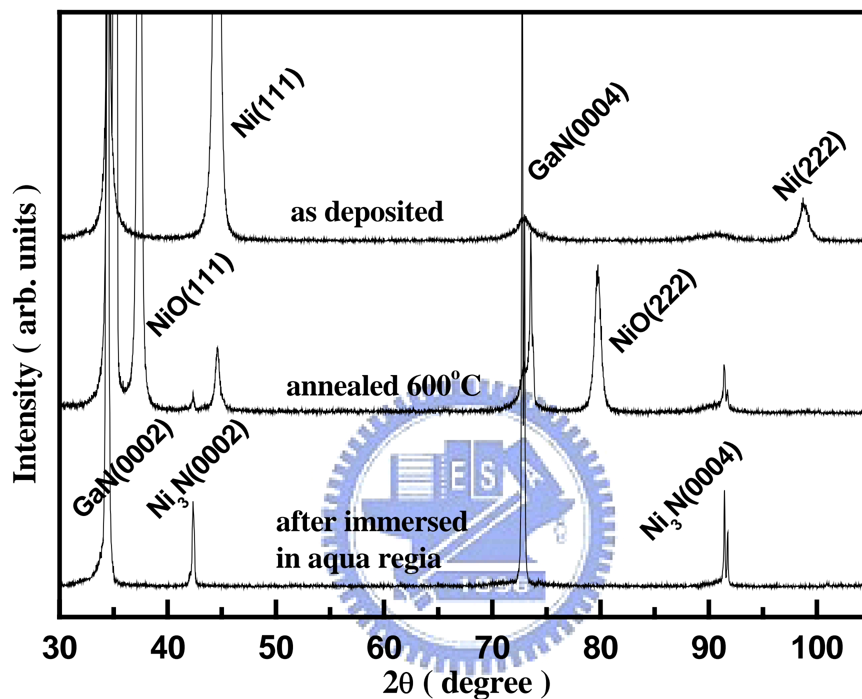

Figure 4-5 XRD spectra of Ni/Mg-doped GaN for cases of as deposited Ni film, after activation with Ni film at 600 ºC in air, and immersed in aqua regia for 30 min after activation with Ni film at 600 ºC, respectively.

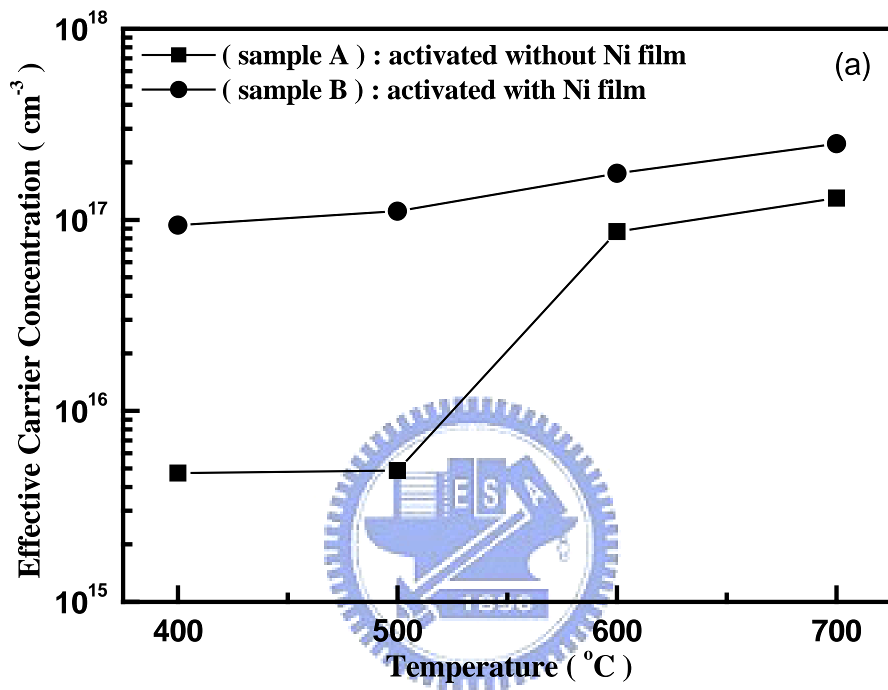

Figure 4-6 (a) Effective carrier concentrations as a function of annealing temperature for activation without and with Ni film.

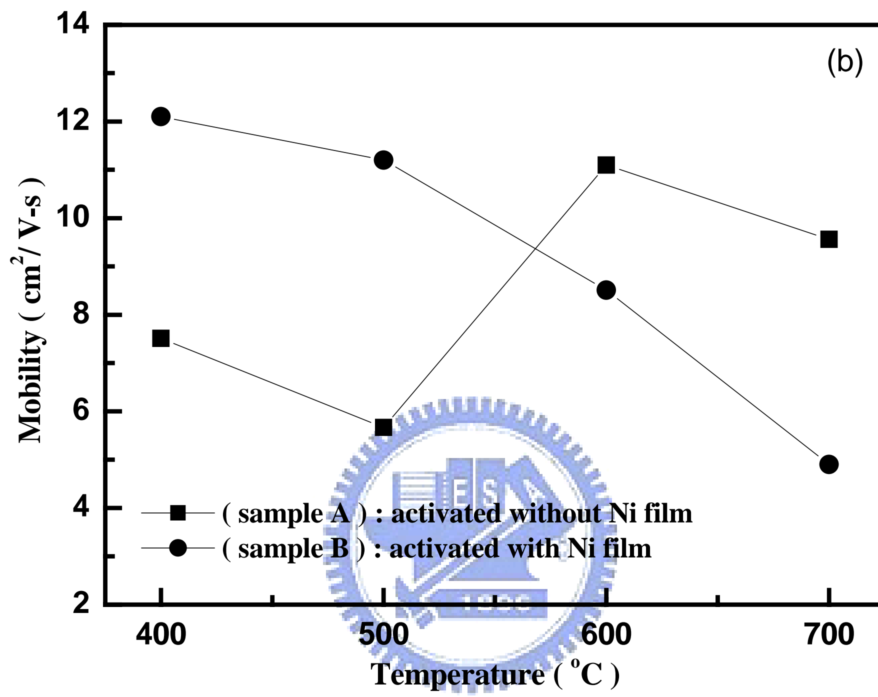

Figure 4-6 (b) Mobility as a function of annealing temperature for activation without and with Ni film.

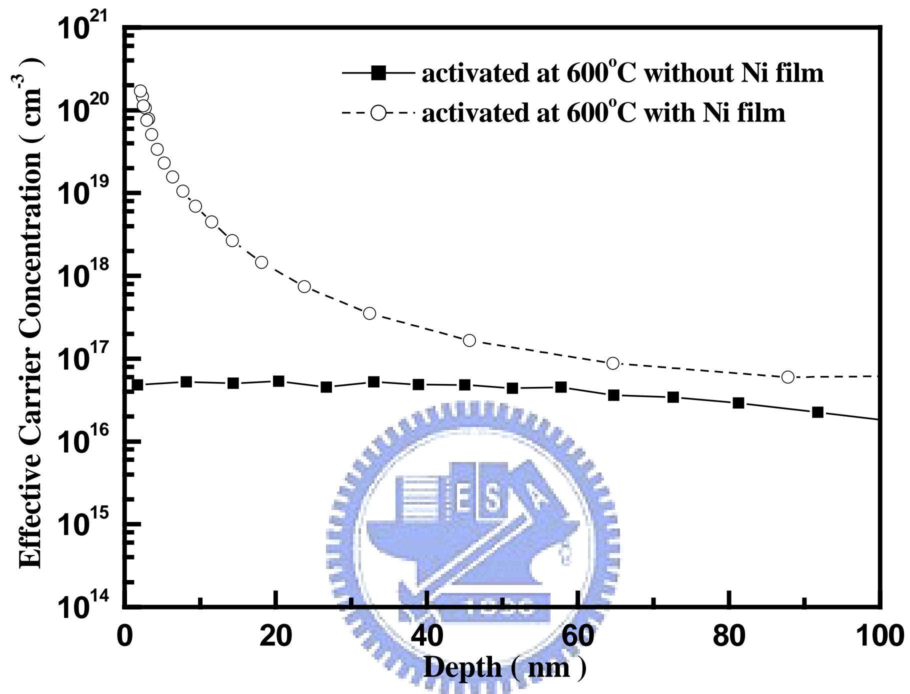

Figure 4-7 Profiles of effective carrier concentrations vs. depth from surface. Mg-doped GaN samples were activated without and with Ni film at 600 ºC.

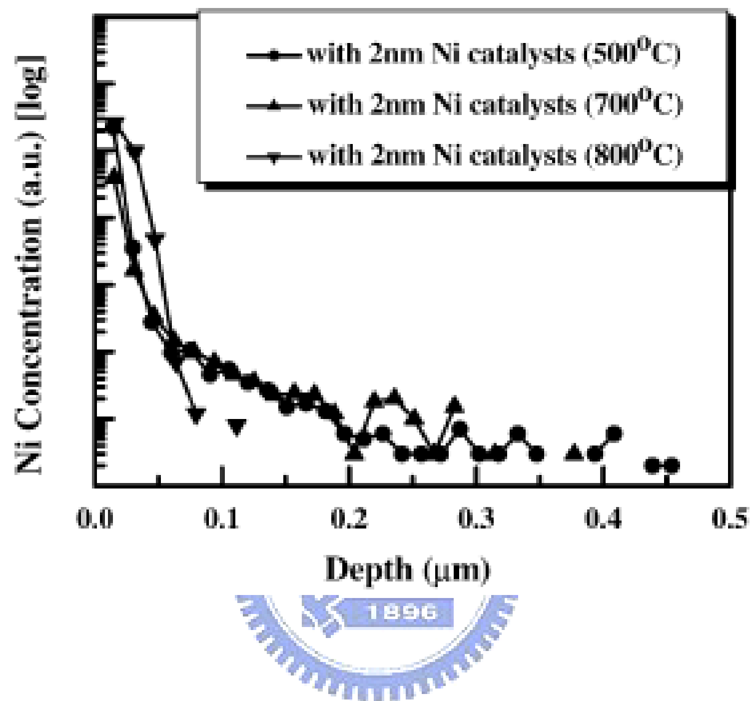

Figure 4-8 SIMS depth profiles of Ni. [18]

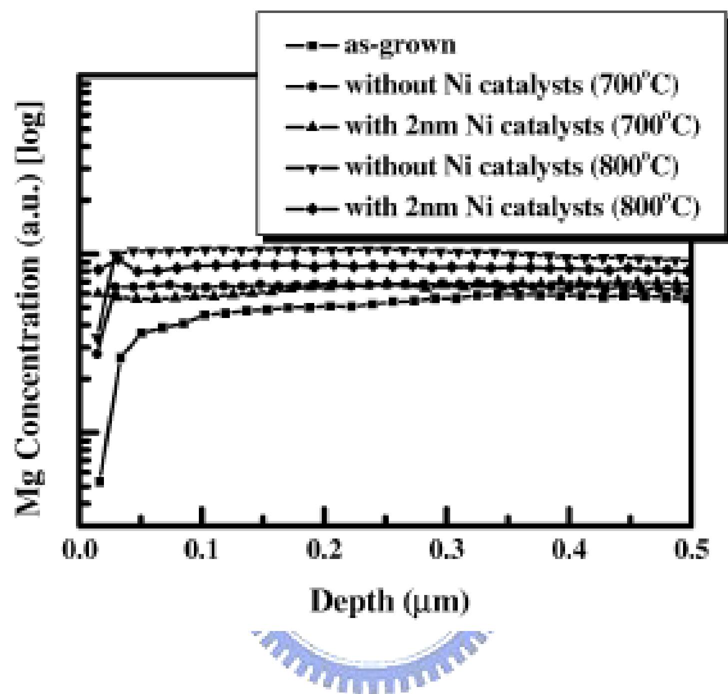

Figure 4-9 SIMS depth profiles of Mg. [18]

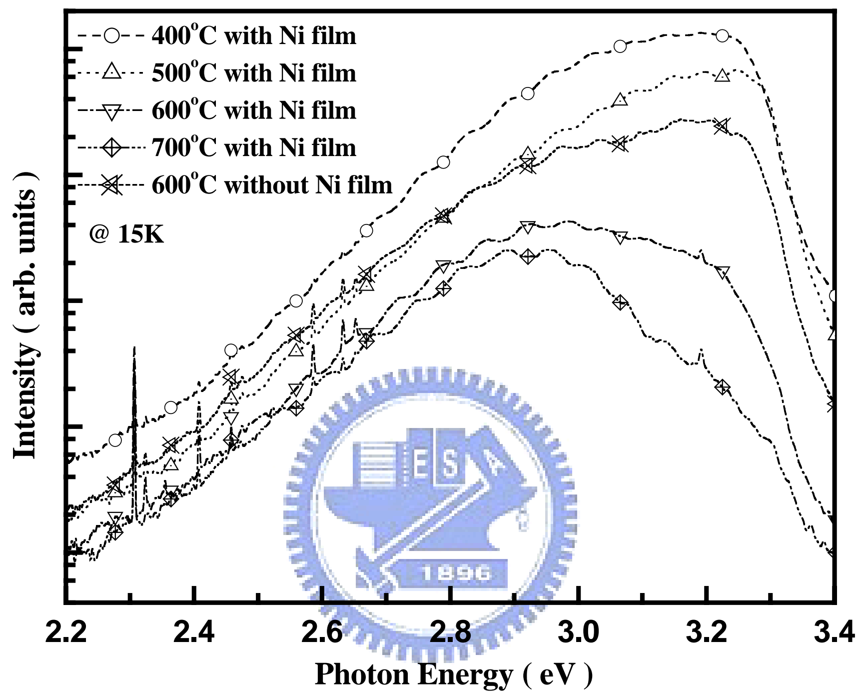

Figure 4-10 Typical PL spectra at 15K for Mg-doped GaN film after activation with and without Ni film.

CHAPTER 5

Effect of Thermal Annealing of Metals Contact on GaN Based LEDs

5.1 Introduction

GaN-based LEDs operating in the green to violet range of the visible spectrum is commercially available and got a great interest these years. In the device process step, a good ohmic contact is necessary to achieve a high performance device. Also, the thermal stability of these contacts is an important issue for device operation.

In the fabrication of ohmic contact to GaN, different metals were applied in both *n*- and *p*-type. For *n*-type GaN, low resistance ohmic contacts around 10^{-5}~10^{-8} Ω cm^2 range have been obtained using Ti/Al metals series. [1-3] For *p*-type GaN, the high work function metals such as Ni, Pd, and Pt were applied. The specific contact resistance around 10^{-2}~10^{-6} Ω cm^2 can be achieved in the Ni/Au, Pd/Au, Ni/Pt/Au, Pd/Pt/Au, and Ni/Pd/Au series. [4-7]

To enhance the output intensity of GaN-based LEDs, it is necessary to reduce the contact resistance and to enhance the transmission efficiency of the upper transparent contact layer (TCL). One possible way to achieve this is to employ indium tin oxide (ITO), instead of Ni/Au, as the *p*-contact material. ITO is a well-known transparent conducting material with a resistivity in below 10^{-4} Ω cm and with a transmittance higher than 90 % in the blue wavelength region under optimized conditions. [8] In fact, ITO has already been used in ZnSe [9] and AlInGaP-based [10] LEDs as the current-spreading layer and in AlInGaAs vertical cavity lasers (VCSEL) as the intracavity contact. [11, 12] Recently, several studies have discussed the applications of ITO contact layers in GaN-based LEDs. [13-17]

The annealing process around 400-750 ºC is necessary to achieve good ohmic properties

for both *n*- and *p*-type case. However, the heat generated by the ohmic loss in the device operation is an important reason to cause the device degradation. [18] The serious degradation in contact morphology can also be observed at higher temperature process due to the formation of new interfacial phases. [19, 20] For high-power applications such as projector and flash lamps, high-power GaN-based LEDs with ITO *p*-type contact layers have been studied. [17] Since power dissipation across the *p*-GaN/metal interface generates Joule heat.

Some literatures reported that the threading dislocation (TD) may degrade the device performance and is a non-radiative recombination center in GaN. [21, 22] The TD provided a diffusion pathway of metals and causes the leakage current in GaN-based devices. [23-25] It is also an important source of reverse leakage current in diodes and causes the poor electro-static discharge behavior in the devices. [26-28]

Thus, we know both contact metals and TDs affect the current-voltage (*I*-*V*) characteristics of the GaN-based devices. Yet, lack of direct studies about the electric properties of the contact metals and TDs. Further understanding of the thermal stability and metallurgy of metals/GaN contact is necessary to improve device operation. In this study, we fabricate the GaN-based multi quantum well (MQW) structure LEDs and study the electric properties under different thermal treatment. The surface morphology and microstructure of these LEDs with different thermal treatment have been characterized by scanning electron microscopy (SEM) and transmission electron microscopy (TEM) analyses. The energy-dispersive X-ray spectrometer (EDS) analysis has been used to observe the changes of the composition. Compared with electrical properties, the existence and influence of dislocations and defects on LEDs can be clearly characterized in this study.

5.2 Experiments

5.2.1 Growth of GaN based LED wafers

Blue GaN-based multiple-quantum-well (MQW) LED wafers were grown by metalorganic chemical vapor deposition (MOCVD) on a *c*-plane sapphire substrate. Trimethylgallium (TMGa), trimethylindium (TMIn) and ammonia (NH_3) were used as Ga, In and N precursors, respectively. The layer structure consists of a GaN buffer layer, followed by a 1.5-μm-thick undoped GaN layer, a 3-μm-thick Si-(*n*) doped GaN layer (n~1×10^{18} cm^{-3}), the active layer, a 0.12-μm-thick Mg-(*p*) doped AlGaN cladding layer (p~5×10^{17} cm^{-3}), and a 0.2-μm-thick Mg-(*p*) doped GaN contact layer (p~7×10^{17} cm^{-3}). The active region, consisting of seven 5 nm/15 nm InGaN/GaN quantum wells is embedded in the region between *p*-type and *n*-type layers.

5.2.2 Fabrication of GaN based LEDs

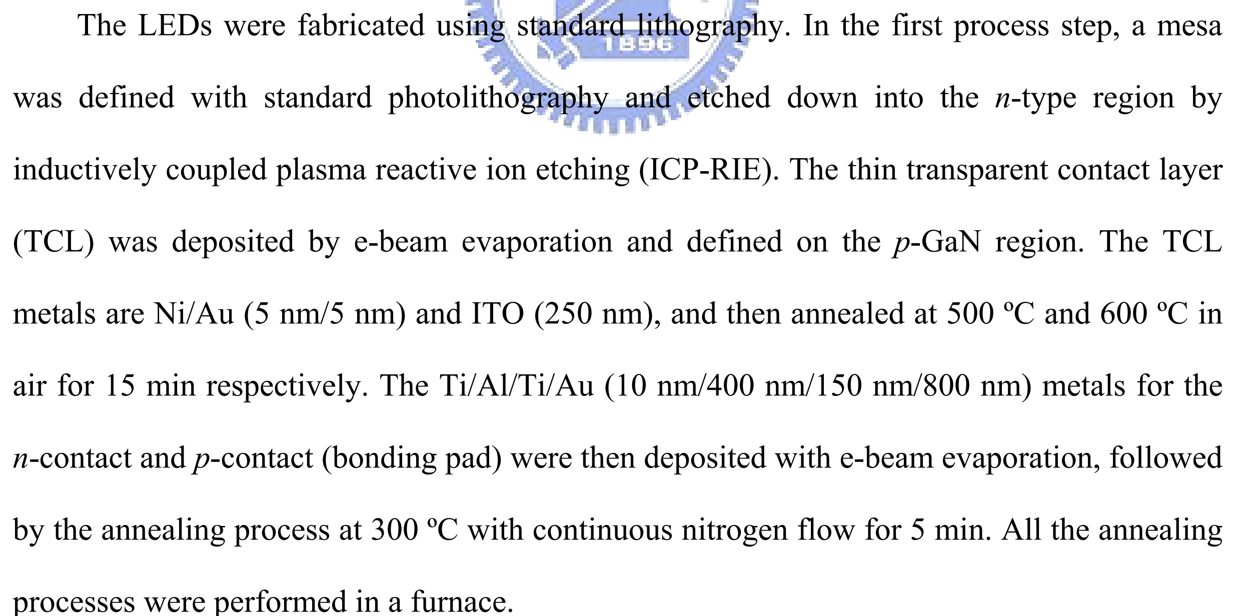

The LEDs were fabricated using standard lithography. In the first process step, a mesa was defined with standard photolithography and etched down into the *n*-type region by inductively coupled plasma reactive ion etching (ICP-RIE). The thin transparent contact layer (TCL) was deposited by e-beam evaporation and defined on the *p*-GaN region. The TCL metals are Ni/Au (5 nm/5 nm) and ITO (250 nm), and then annealed at 500 ºC and 600 ºC in air for 15 min respectively. The Ti/Al/Ti/Au (10 nm/400 nm/150 nm/800 nm) metals for the *n*-contact and *p*-contact (bonding pad) were then deposited with e-beam evaporation, followed by the annealing process at 300 ºC with continuous nitrogen flow for 5 min. All the annealing processes were performed in a furnace.

5.2.3 Measurements and analyses

The wafers were then cut into chips. These chips were then annealed with different

temperatures in a furnace with continuous nitrogen flow in ten minutes. For comparison, some LED structure wafers after activating *p*-type GaN layer at 600 °C in N_2 for 30 min were thermal treated at 500 and 700 °C in N_2 for 30 min. Then these wafers were processed to LED chips. The electrical characteristics were measured at room temperature with HP-4155 *I-V* analyzer. For TEM measurements, the specimens were carried out by JEOL JEM-2010 microscope operated at 200kV. The SEM surface images were taken with Hitachi S-4000 instrument. For SEM measurements, a thin Au film was sputtered on the sample surface to enhance the conductivity.

5.3 Results and Discussions

5.3.1 Effect of thermal annealing on GaN based LEDs with Ni/Au contact layer

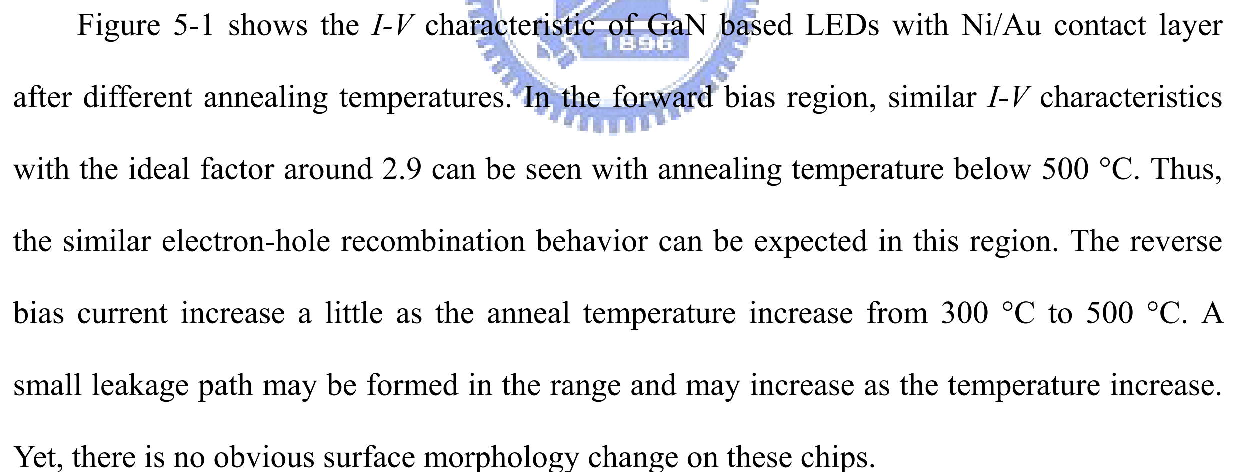

Figure 5-1 shows the *I-V* characteristic of GaN based LEDs with Ni/Au contact layer after different annealing temperatures. In the forward bias region, similar *I-V* characteristics with the ideal factor around 2.9 can be seen with annealing temperature below 500 °C. Thus, the similar electron-hole recombination behavior can be expected in this region. The reverse bias current increase a little as the anneal temperature increase from 300 °C to 500 °C. A small leakage path may be formed in the range and may increase as the temperature increase. Yet, there is no obvious surface morphology change on these chips.

While the annealing temperature higher than 700 °C, the electrical short circuit behavior can be observed and the LEDs become lightless. The short circuit resistance decreases as the annealing temperature increases. Thus, a main leakage path can be expected and increase as the annealing temperature increase from 700 °C to 900 °C.

Figure 5-2 shows the *I-V* characteristics of GaN based LEDs that LED structure wafers without thermal treated and with thermal treated at 500 and 700 °C in N_2 for 30 min. From

I-V curves of Fig. 5-2, the same *I-V* behavior with the ideality factor around 3.0 can be observed in the forward bias region. In the reverse bias region, the leakage currents (<1 μA) at -5 V were slightly different between thermal treated at 500 and 700 °C. According to the results of Fig. 5-1 and Fig. 5-2, it was revealed clearly that LED structure wafers have good thermal reliability than LED chips. The original LED wafer could resist heat at higher temperature. Thus, we suggested that the effect of heat on metals contact was an important factor in GaN-based LEDs.

Figure 5-3 shows the SEM image of thick Ni/Au contact layer on *p*-GaN surface after 900 °C annealing process. A lot of bubbles with diameter around sub-micrometer to 10 μm can be observed. These bubbles cause the surface morphology change and can be observed on the chips with the annealing temperature higher than 600 °C. These bubbles may formed from the sintering of Ni/Au to *p*-GaN and degrade the properties of the LEDs. This phenomenon, the elevated temperature chemical instability of GaN defects exposed to either metal films or free surfaces, is very general in nature and has importance for GaN-based device design. Bulk GaN has the following decomposition reaction above 800 °C: GaN → Ga(*l*) + N_2(*g*). Nevertheless, GaN films can survive higher temperatures due to the high stability of the (0001) surface. In addition, the reaction is sluggish due to kinetic difficulties recombining nitrogen atoms into N_2 molecules on the GaN surface. At locations where a dislocation exits GaN, the atomic arrangement is of lower stability and therefore triggers the decomposition of GaN (as shown in Fig. 5-4). Nitrogen atoms may diffuse into the metal, recombine into molecules and form N_2 gas. Such gas accumulates under the metal film and exerts enough pressure to cause metal film de-cohesion.

Figure 5-5(a) shows the TEM cross-sectional image after annealing at 900 °C. A hollow center of the bubble can be seen clearly in this figure. Below the metallic bubble, the straight TD can be found on $(1\bar{1}00)$ plane. In Fig. 5-5(b), the straight TD can be also observed after

annealing at 600 °C. Using the energy dispersive X-ray spectrometer (EDS), the compositions were analyzed. There are four interesting regions: the metallic bubble (EDS-1), the TD (EDS-2), the *p*-GaN layer (EDS-3) of Fig. 5-5(a), and the TD (EDS-4) of Fig. 5-5(b). Figure 5-6 shows the EDS spectra of these regions. In the EDS-1, the main compositions are Ni, Ga, and Au as shown in Fig. 5-6(a). After the EDS spectrum analysis, the phases were characterized as the Ni- and Au- containing compounds, such as Ni_4N, Ni_3N, Ga_4Ni_3, Ga_3Ni_2, GaAu and $GaAu_2$. [27] These phases may be formed due to the N and Ga out-diffusion, or Ni and Au in-diffusion in the annealing process.

The EDS spectrum of the EDS-2 was shown in Fig. 5-6(b). Compared to the EDS spectrum of the EDS-3 as shown in Fig. 5-6(c), the Ni and Au can be observed clearly in the TD region after annealing at higher temperature. Compared to the surface morphology as shown in Fig. 5-3, the Ni and Au may migrate on top of the TDs and indiffuse along the TDs in the annealing process. The in-diffusion process can only occurred with the TDs since there are no Ni and Au signals with *p*-GaN region as shown in Fig. 5-6(c). The diffusion of Ni and Au along the TD through the MQW structure may cause a short circuit current path from *p*-GaN to *n*-GaN region. Furthermore, the TD region only contains very small amount of Ni signal after annealing at 600 °C as shown in Fig. 5-6(d). Thus, the short circuit behavior as shown in Fig. 5-1 with annealing temperature higher than 600 °C can be realized. This study provides the direct evidence that metals in-diffusion along the TDs cause the degradation of the LEDs characteristics.

5.3.2 Effect of thermal annealing on GaN based LEDs with ITO contact layer

The SEM micrographs of the as-deposited and annealed 700 °C ITO contact layer on *p*-GaN have been observed as shown in Fig. 5-7(a) and Fig. 5-7(b) respectively. Small grains can be observed in both the figures. It reveals that the surface of the ITO contact layer on

p-GaN was not obviously degraded after annealing.

The *I-V* characteristics of the GaN LEDs with ITO contact layer at different thermal treatment temperatures are shown in Fig. 5-8. In this case, the leakage currents of normal LEDs and those thermally treated at 600 ºC at reverse biases of 5 V were 5.0×10^{-8} and 3.0×10^{-7} A, respectively. After annealing at 600 ºC, a small increase in the current in the reverse bias region can be observed. A leakage path may be formed in this case. In the forward bias region, the forward voltages (at an injection current of 20 mA) of normal LEDs and those thermally treated at 600 ºC were determined to be about 3.45 and 3.20 V, respectively. A slight increase in the ideality factor from 3.3 to 3.7 can be seen after 600 ºC annealing. Since higher reverse bias leakage currents can also be observed in the curve, this decay behavior may come from the reduction of device resistance with higher-temperature annealing. As the annealing temperature increases beyond 700 ºC, the *I-V* characteristics become short-circuited and a leakage path may be formed. In section 5.3.1, the migration and in-diffusion of Ni and Au along the TDs caused short circuits in the *p-n* junctions at high temperatures.

To study the short-circuit behavior, all contact metals after annealing were removed from the LEDs, and the GaN structure was etched down to the *n*-GaN region (about 500 nm deep) by ICP-RIE. Figure 5-9(a) shows a SEM image of the etched *n*-GaN surface of a device after annealing at 600 ºC. Some pinholes formed by the dislocations can be observed. It has been reported that a mixed dislocation terminates at the bottom of each etch pit. [29] Figure 5-10(a) shows the EDS spectrum of the pinhole, marked "1" in Fig. 5-9(a). The Au signal comes from the sputtering process. The main components are Ga and N. No obviously different composition can be observed in the pinhole region.

Figure 5-9(b) shows the SEM image of the etched *n*-GaN surface of a device after annealing at 700 ºC. In the pinhole region marked "2" in Fig. 5-9(b), In and Sn signals were obtained as shown in Fig. 5-10(b). Compared with the flat region, marked "3" in Fig. 5-9(b),

the main components are only Ga and N as shown in Fig. 5-10(c). According to these results, In and Sn from ITO may diffuse through MQW along the dislocations, which causes a leakage path when annealing temperatures reach 700 ºC and hence the short circuits as shown in Fig. 5-8. We suggest that surface pits and the connected dislocations in GaN-based LEDs may enhance contact metal migration along the dislocations, leading to further increases in junction leakage, and eventually to serious failure. Thus, this study provides the evidence that the diffusion of the metallic component along the dislocations is a main degradation mechanism of devices in the annealing process.

5.4 Conclusions

After annealing above 700 ºC, the electrical short circuit behavior of GaN based LEDs with Ni/Au contact layer has been observed. At annealing 900 ºC, Ni- and Au- contained metallic bubbles have been observed on the *p*-GaN surface by SEM. Both TEM and EDS analyses reveal that the core of the TD contains Ni and Au after annealing higher temperatures. These results imply direct evidences that the migration and in-diffusion of Ni and Au along the TDs cause the short circuit characteristics of the *p*-*n* junction at high temperatures.

Furthermore, the GaN based LEDs with ITO contact layer have the same phenomenon. As the annealing temperature reaches 700 ºC, the In- and Sn- containing compounds from the top ITO contact layer can be observed in the *n*-GaN region along dislocations. The diffusion of the metal-containing compounds along dislocations is the main mechanism causing the short circuits in the device in the high-temperature annealing process.

5.5 References

[1] J. S. Foresi and T. D. Moustakas, Appl. Phys. Lett. **62**, 2859 (1993).

[2] M. E. Lin, Z. Ma, F. Y. Huang, Z. F. Fan, L. H. Allen, and H. Morkoc, Appl. Phys. Lett. **64**, 1003 (1994).

[3] Z. Fan, S. Mohammad, and W. Kim, Appl. Phys. Lett. **68**, 1672 (1996).

[4] J. K. Ho, C. S. Jong, C. C. Chiu, C. N. Huang, and K. K. Shih, Appl. Phys. Lett. **74**, 1275 (1999).

[5] J. K. Kim, J. L. Lee, J. W. Lee, H. E. Shin, Y. J. Park, and T. Kim, Appl. Phys. Lett. **73**, 2953 (1998).

[6] J. S. Jang, K. H. Park, H. K. Jang, H. G. Kim, and S. J. Park, J. Vac. Sci. Technol. **B16**, 3105 (1998).

[7] C. F. Chu, C. C. Yu, Y. K. Wang, J. Y. Tsai, F. I. Lai, and S. C. Wang, Appl. Phys. Lett. **77**, 3423 (2000).

[8] J. W. Bae, H. J. Kim, J. S. Kim, N. E. Lee and G. Y. Yeom, Vacuum **56**, 77 (2000).

[9] M. Hagerott, H. Jeon, A. V. Nurmikko, W. Xie, D. C. Grille, M. Kobayashi and R. L. Gunshor, Appl. Phys. Lett. **60**, 2825 (1992).

[10] Y. H. Aliyu, D. V. Morgan, H. Thomas and S. W. Bland, Electron. Lett. **31**, 2210 (1995).

[11] M. A. Matin, A. F. Jezierski, S. A. Bashar, D. E. Lacklison, T. E. Benson, T. S. Cheng, J. S. Roberts, T. E. Sale, J. W. Orton, C. W. Foxton and A. A. Rezazadeh Electron. Lett. **30**, 318 (1994).

[12] C. L. Chua, R. L. Thornton, D. W. Treat, V. K. Yang and C. C. Dunnrowicz, IEEE Photonics Technol. Lett. **9**, 551 (1997).

[13] T. Margalith, O. Buchinsky, D. A. Cohen, A. C. Abare, M. Hansen, S. P. DenBaars and L. A. Coldren, Appl. Phys. Lett. **74**, 3930 (1999).

[14] R. H. Horng, D. S. Wuu, Y. C. Lien and W. H. Lan, Appl. Phys. Lett. **79**, 2925 (2001).

[15] S. Y. Kim, H. W. Jang and J. L. Lee, Appl. Phys. Lett. **82**, 61 (2003).

[16] C. S. Chang, S. J. Chang, Y. K. Su, Y. Z. Chiou, Y. C. Lin, Y. P. Hsu, S. C. Shei, H. M. Lo, J. C. Ke, S. C. Chen and C. H. Liu, Jpn. J. Appl. Phys. **42**, 3324 (2003).

[17] Y. C. Lin, S. J. Chang, Y. K. Su, C. S. Chang, S. C. Shei, J. C. Ke, H. M. Lo, S. C. Chen and C. W. Kuo, Solid-State Electron. **47**, 1565 (2003).

[18] S. Nakamura, M. Senoh, and T Mukai, Appl. Phys. Lett. **62**, 2390 (1993).

[19] Q. Z. Liu and S. S. Lau, Solid-State Electron. **42**, 677 (1998).

[20] M. E. Lin, Z. Ma, F.Y. Huang, Z. F. Fan, L. H. Allen, and H. Morkoc, Appl. Phys. Lett. **64**, 1003 (1994).

[21] S. J. Rosner, E. C. Carr, M. J. Ludowise, G. Girolami, and H. I. Erikson, Appl. Phys. Lett. **70**, 420 (1997).

[22] T. Sugahara, H. Sato, M. Hao, Y. Naoi, S. Kurai, S. Tottori, K. Yamashita, K. Nishino, L. T. Romano, and S. Sakai, Jpn. J. Appl. Phys. **37**, L398 (1998).

[23] C. Sasaoka, H. Sunakawa, A. Kimura, M. Nido, and A. Usui, J. Cryst. Growth **189/190**, 61 (1998).

[24] A. Osinsky, S. Gangopadhyay, R. Gaska, B. Williams, M. A. Khan, D. Kuksenkov, and H. Temkin, Appl. Phys. Lett. **71**, 2334 (1997).

[25] S. NaKamura, J. Cryst. Growth **201/202**, 290 (1999).

[26] P. Kozodoy, J. P. Ibbetson, H. Marchand, P. T. Fini, S. Keller, J. S. Speck, S. P. DenBaars, and U. K. Mishra, Appl. Phys. Lett. **73**, 975 (1998).

[27] J. K. Sheu, Y. K. Su, G. C. Chi, W. C. Chen, C. Y. Chen, C. N. Huang, J. M. Hong, Y. C. Yu, C. W. Wang, and E. K. Lin, J. Appl. Phys. **83**, 3172 (1998).

[28] J. W. P. Hsu, M. J. Manfra, D. V. Lang, S. Richter, S. N. G. Chu, A. M. Sergent, R. N. Kleiman, L. N. Pfeiffer, and R. J. Molnar, Appl. Phys. Lett. **78**, 1685 (2001).

[29] K. Shiojima, J. Vac. Sci. & Technol. B **18**, 37 (2000).

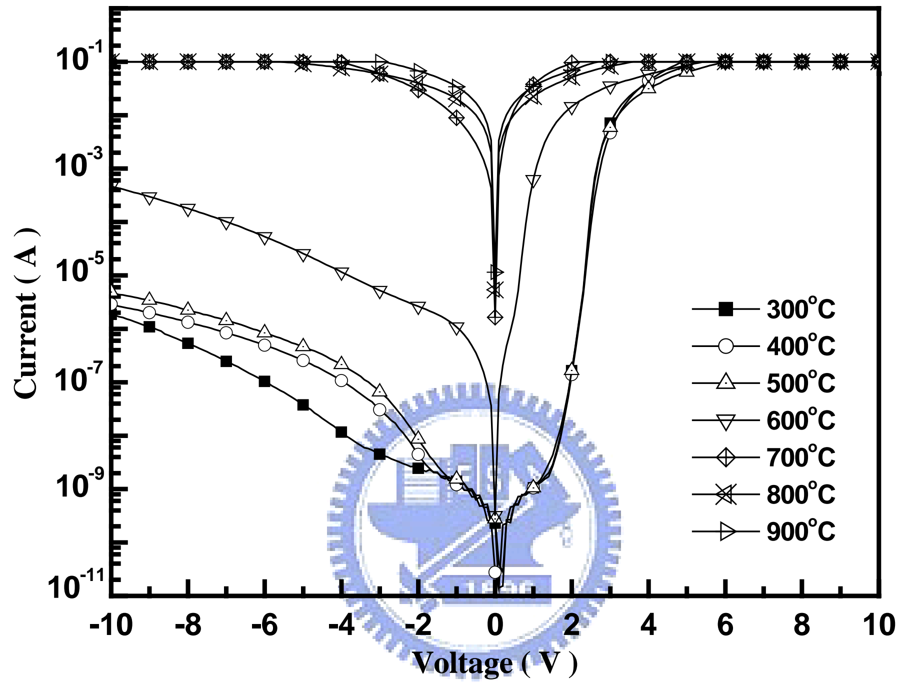

Figure 5-1 *I-V* characteristics of GaN based LEDs with Ni/Au contact layer at various annealing temperatures.

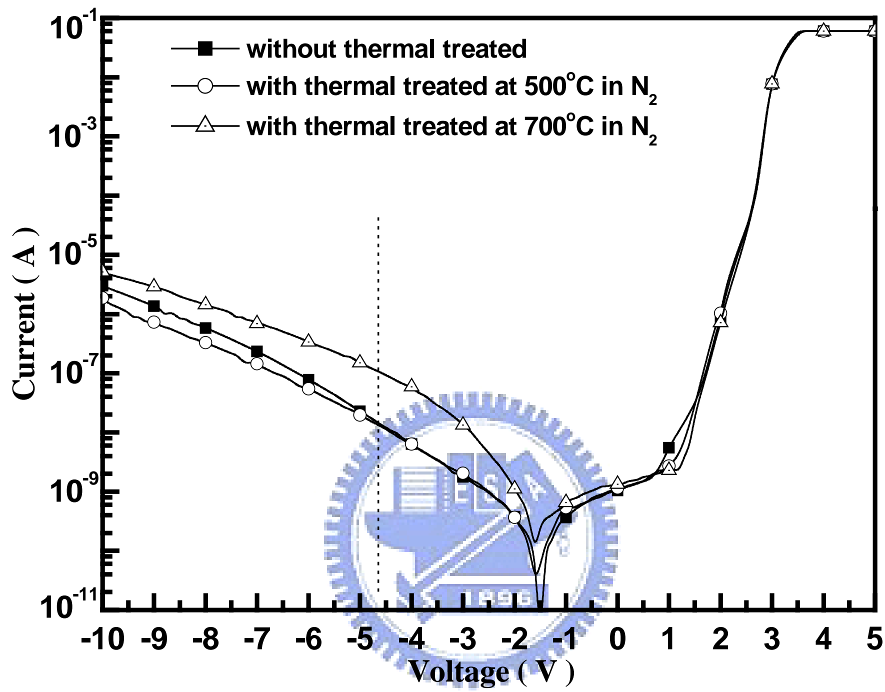

Figure 5-2 *I-V* characteristics of GaN based LEDs. The LED structure wafers without thermal treated and with thermal treated at 500 and 700 °C.

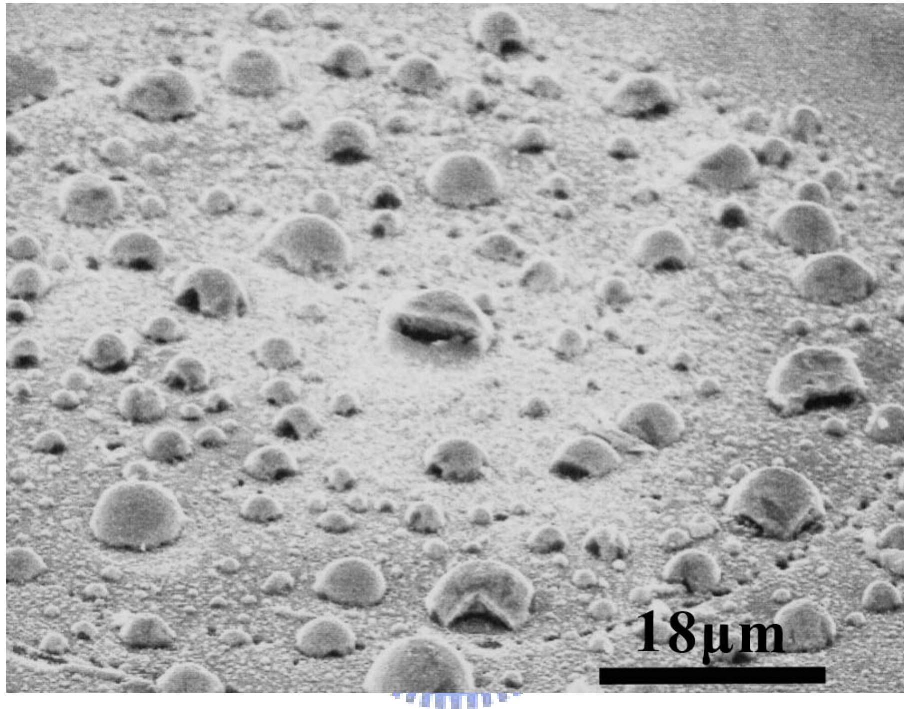

Figure 5-3 SEM image of Ni/Au on *p*-GaN contact surface after annealing at 900 °C.

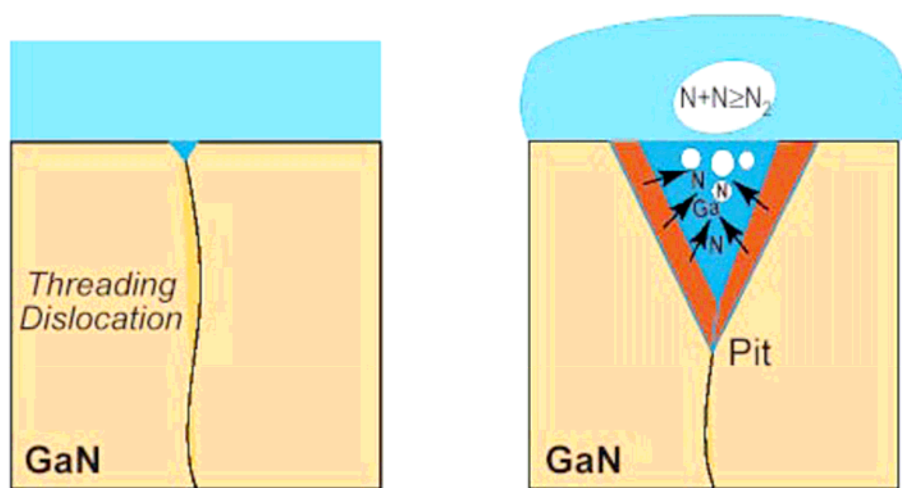

Figure 5-4 Schematic drawing illustrating decomposition of GaN along a dislocation line and resulting in the formation of N_2.

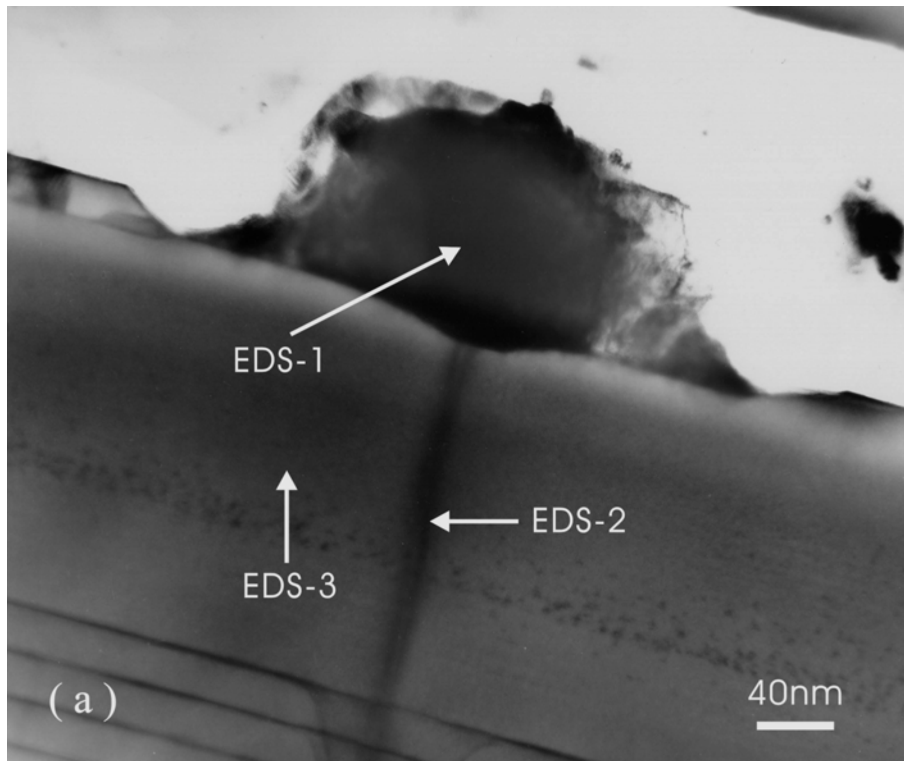

Figure 5-5(a) Cross-section bright-field TEM micrograph of the LEDs structure with Ni/Au contact layer after annealing at 900 °C.

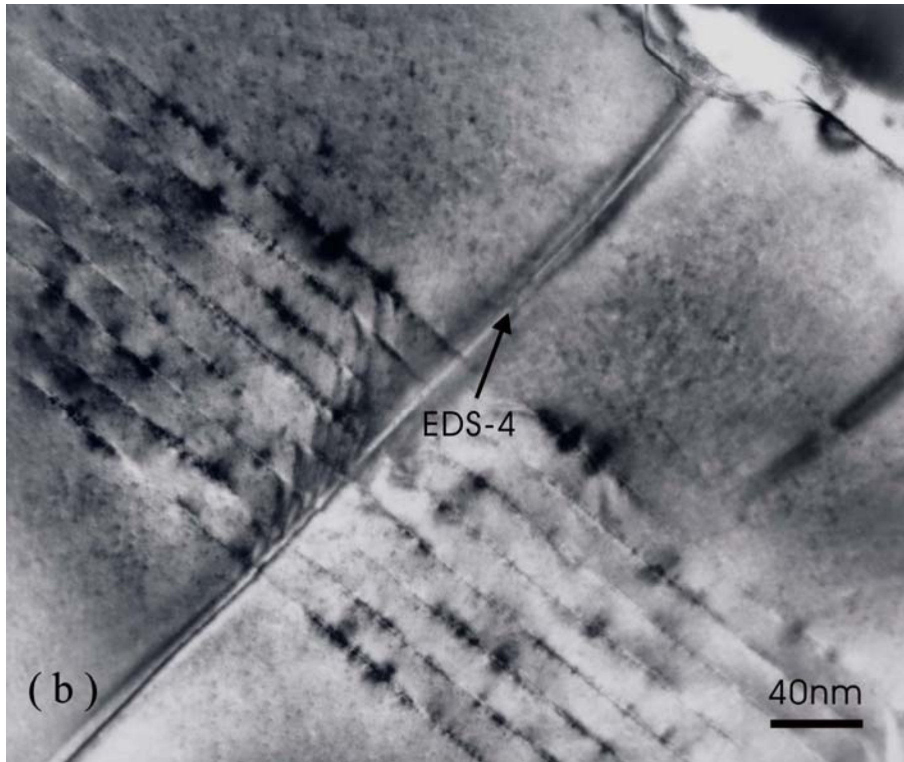

Figure 5-5(b) Cross-section bright-field TEM micrograph of the LEDs structure with Ni/Au contact layer after annealing at 600 °C.

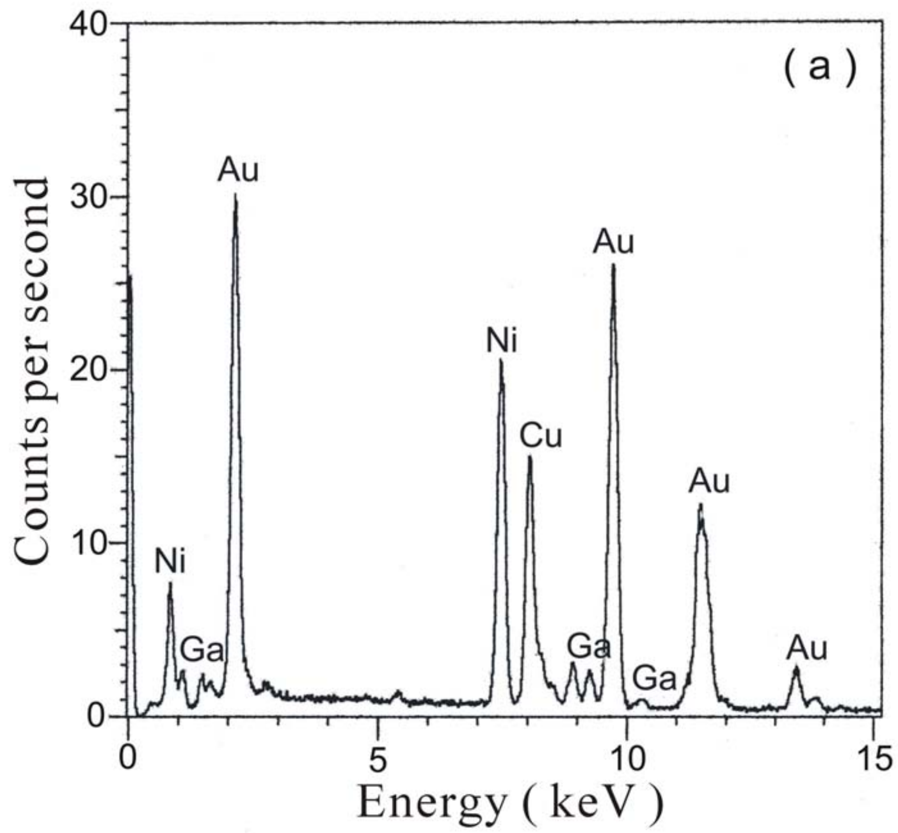

Figure 5-6(a) EDS spectrum of EDS-1 region at metallic bubble of Fig. 5-5(a).

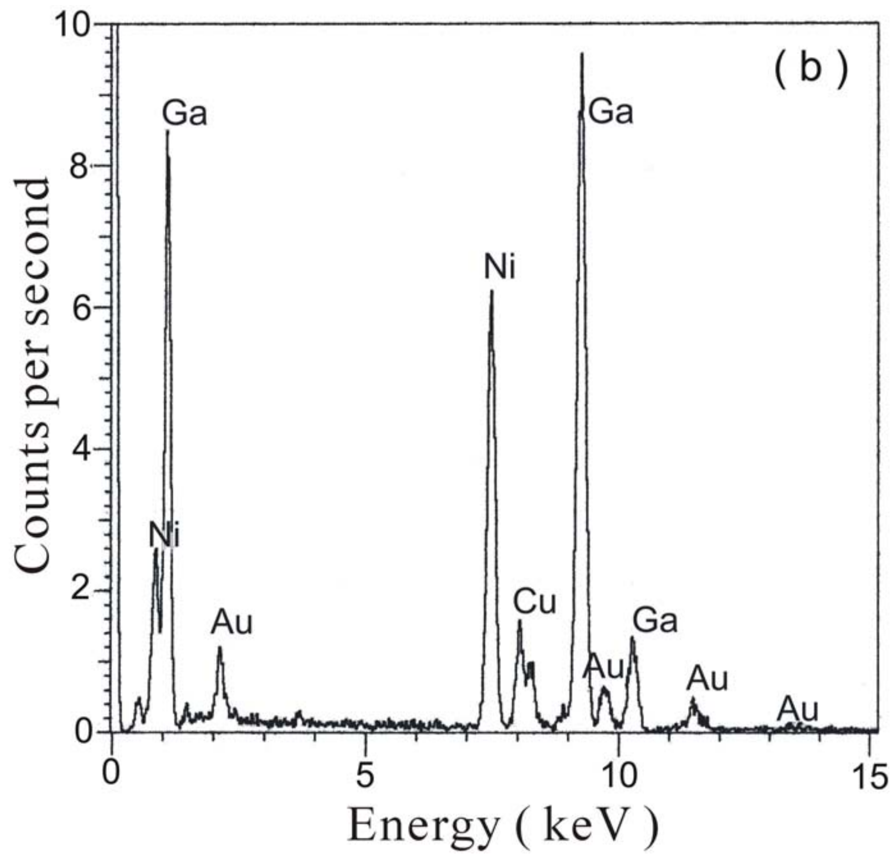

Figure 5-6(b) EDS spectrum of EDS-2 region at threading dislocation of Fig. 5-5(a).

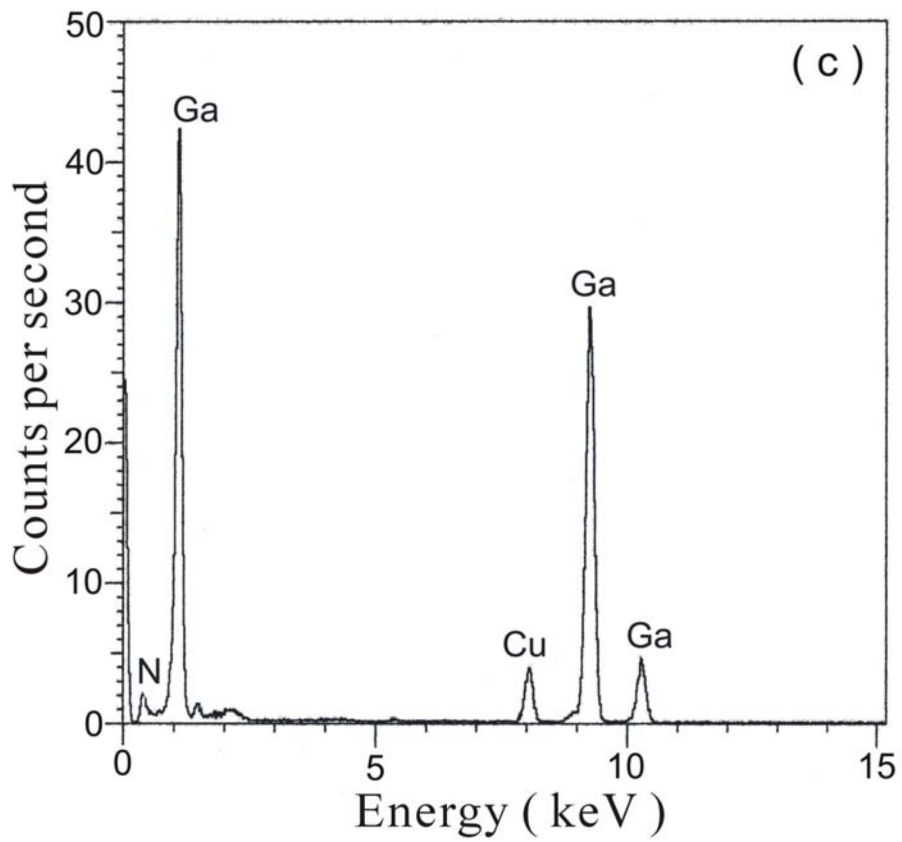

Figure 5-6(c) EDS spectrum of EDS-3 region at *p*-GaN layer of Fig. 5-5(a).

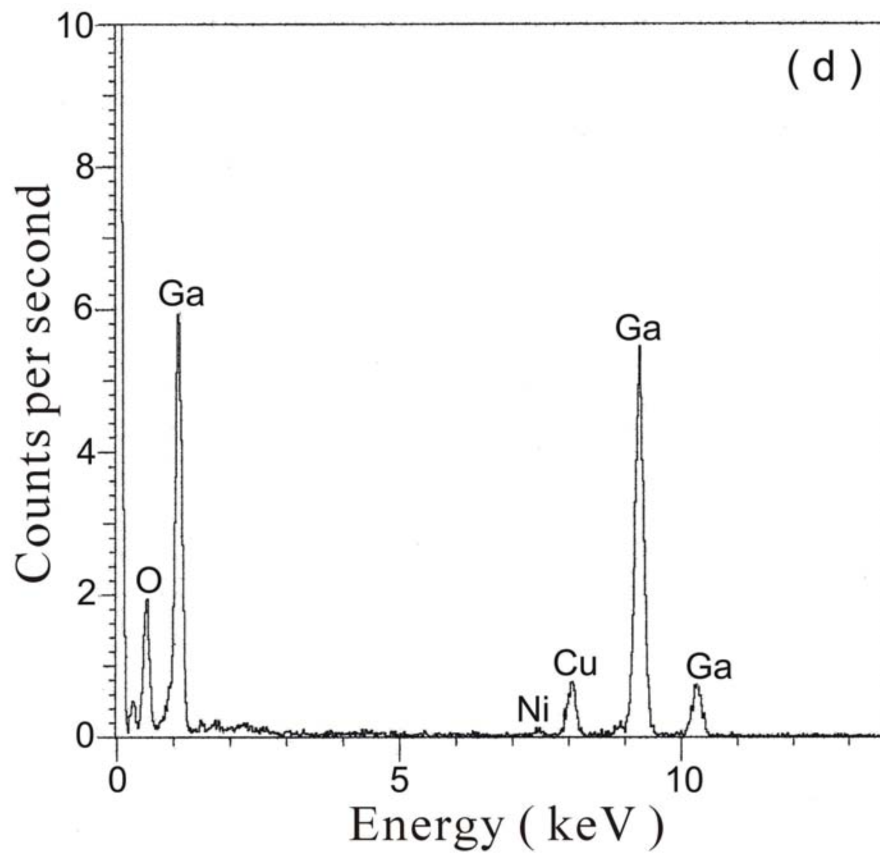

Figure 5-6(d) EDS spectrum of EDS-4 region at threading dislocation of Fig. 5-5(b).

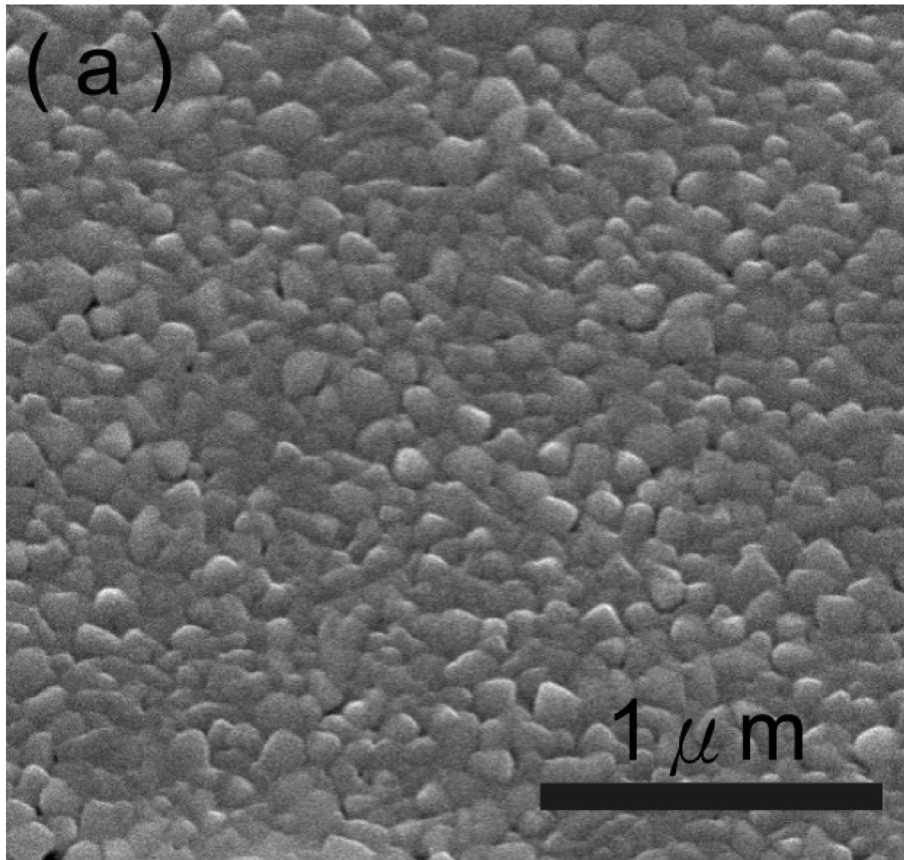

Figure 5-7(a) SEM image of as-deposited ITO contact layer on *p*-GaN.

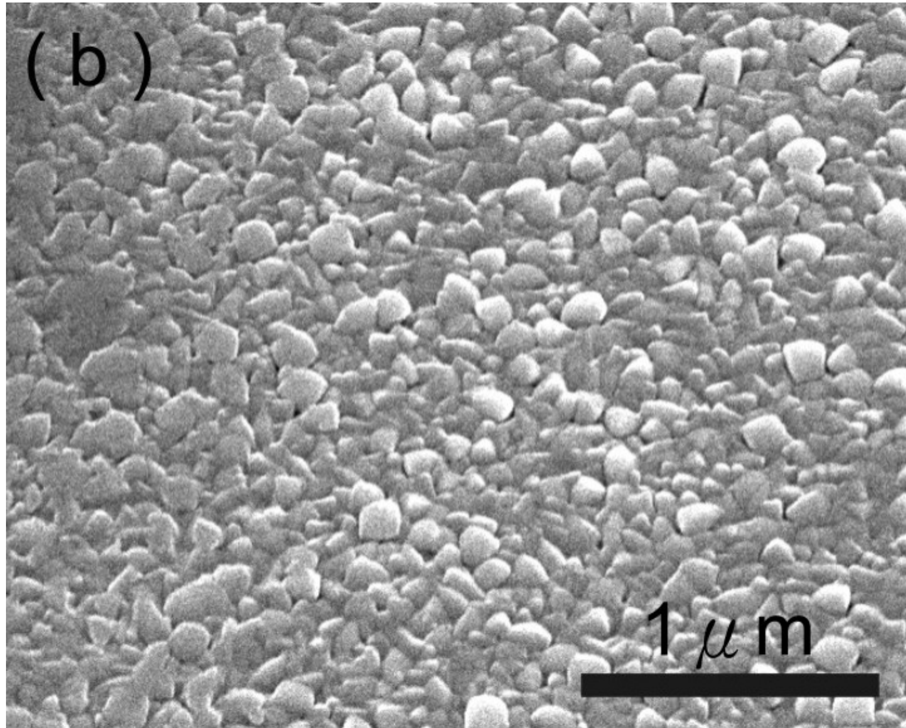

Figure 5-7(b) SEM image of the ITO contact layer on *p*-GaN after annealing at 700 °C.

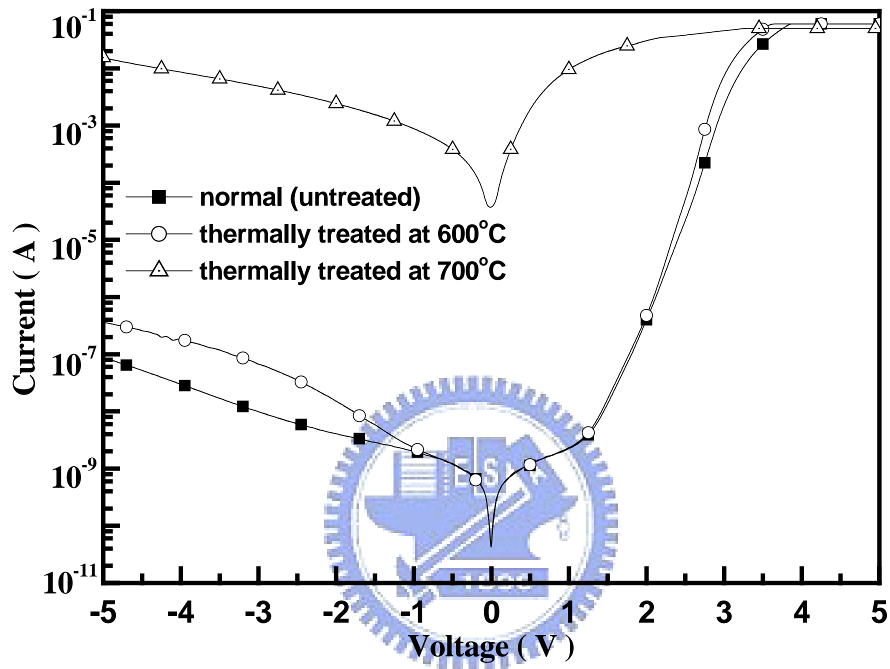

Figure 5-8 *I-V* characteristics of GaN-based LEDs with ITO contact layer after different thermal treated temperatures.

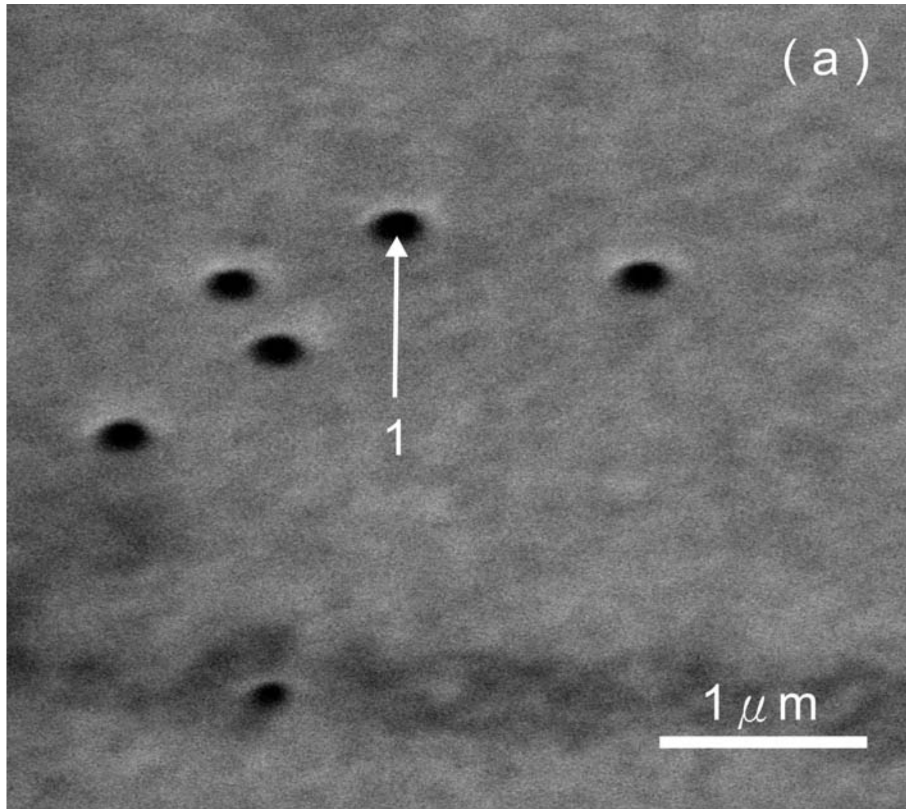

Figure 5-9(a) SEM image of etched *n*-GaN surface with device after 600 ºC annealing.

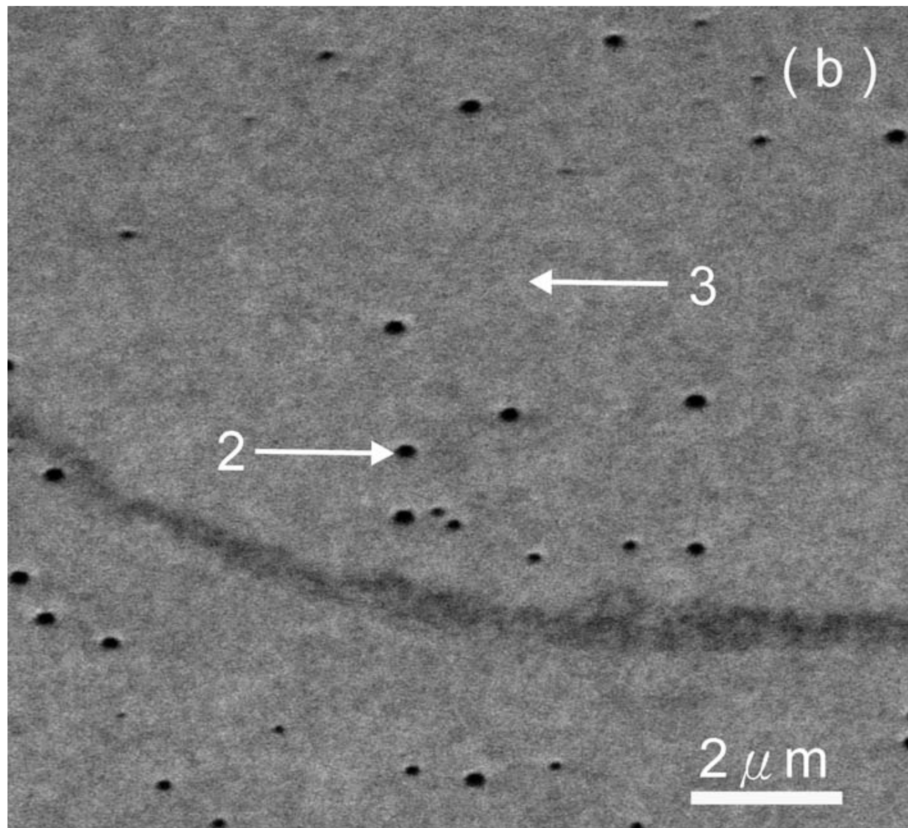

Figure 5-9(b) SEM image of etched *n*-GaN surface with device after 700 ºC annealing.

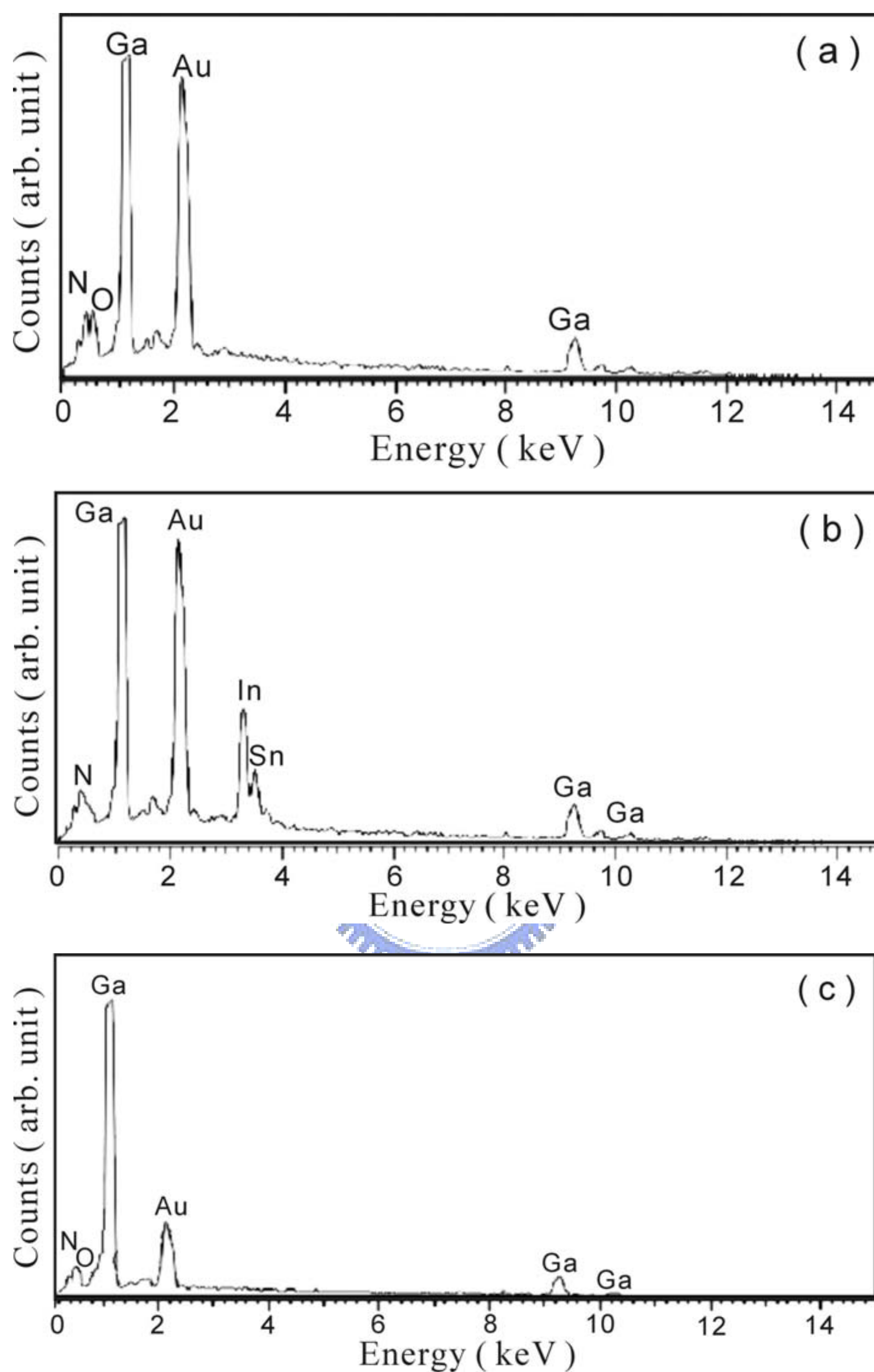

Figure 5-10 EDS spectra obtained from different regions: (a) “1” at pinhole in Fig. 5-9(a), (b) “2” at pinhole in Fig. 5-9(b), and (c) “3” at flat *n*-GaN surface in Fig. 5-9(b).

CHAPTER 6

Influences of Interfaces of Contact Metals/GaN on LED Properties

6.1 Introduction

The achievement of high-quality and reliable ohmic contacts is crucial for GaN based optoelectronic devices, such as light-emitting diodes (LEDs), photodetectors, and laser diodes (LDs). [1] For *p*-type GaN, low-resistant ohmic contacts ($<10^{-4}\ \Omega\ cm^2$) were obtained using Ni/Au, [2] Pt/Au, [3] and Ru/Ni. [4] Among these contacts, the Ni/Au bilayer contact is commonly used as a transparent ohmic contact on *p*-type GaN due to its low contact resistivity and high transparency. [2] However, the thin layer thickness of the contact (<100 Å) limits current spreading as well as thermal stability. [5] In order to enhance the output intensity of nitride-based LEDs, it is necessary to reduce the contact resistance and to enhance the transmission efficiency of the upper *p*-contact layer. Conventional InGaN/GaN LEDs use semi transparent Ni/Au as the *p*-contact material. However, the transmittance of such a semi transparent Ni/Au contact is only around 60-75 % in the 450-550 nm wavelengths. Although we could increase the transmittance by reducing the thickness of the Ni/Au metal layer, contact reliability could become an issue when the contact layer thickness becomes too small.

Indium tin oxide (ITO) is one of the promising electrodes on *p*-type GaN due to high transparency (>80 %) and good conductivity ($\sim10^4\ \Omega^{-1}\ cm^{-1}$). In general, ITO films on *p*-type GaN showed Schottky behavior even after thermal annealing due to low hole concentration. [6] While many attempts have been made to find a way to lower the contact resistivity on *p*-type GaN using ITO, the contact resistivity was still high for the *p*-electrode of GaN-based LEDs. [7] Hong *et al.* deposited Ni (10 nm) and ITO (250 nm) films on *p*-GaN ($p=2\times10^{17}$

cm^{-3}) by thermal evaporation and magnetron RF sputtering at room temperature, respectively, and found that they could achieve a low specific contact resistance (8.6×10^{-4} Ω cm^2) and a high transparency (above 80-95 % for 450-550 nm) when the deposited films were annealed at 600 ºC in atmosphere. [7] In fact, the operation voltages of nitride based LEDs with ITO *p*-contacts were reported to be too large for practical device applications. Recently, Chang *et al.* have reported the fabrication of nitride-based LEDs with an n^+-short period superlattice (SPS) tunnel contact layer [8] and an ITO transparent contact. To reduce *p*-contact resistance, Chang *et al.* have recently demonstrated nitride based LEDs incorporated with an n^+-InGaN-GaN short-period-superlattice (SPS) tunneling contact layer which have low operating voltages [9]. By growing an SPS structure on top of the *p*-GaN capping layer, one can achieve a good ohmic contact via tunneling when the n^+(InGaN-GaN)-*p*(GaN) junction is properly reverse biased. It was found that incorporating the SPS layer into the LED structure could effectively reduce the series resistance of the chip from 42 to 18 Ω. In order to increase LED output intensity, the transparent ITO as the p-contact material can replace the semitransparent Ni/Au, and ITO-based metals can contact on the n^+-InGaN-GaN (SPS) tunneling contact layer.

However, for high-power applications such as projectors and flash lamps, high-power GaN-based LEDs with an ITO *p*-type contact layer have been studied. [10] Since power dissipation across the *p*-GaN/metal interface generated Joule heat, failure of LEDs and LDs was due to indiffusion of the ohmic contact elements along dislocations in the GaN epilayers, leading to an electrical short of the *pn* junction. [11] Thus, it is essential to understand the thermal stability and metallurgy of ITO-GaN contact in addition to developing a low-resistance ohmic system.

In this study, the current-voltage (*I-V*) properties of GaN based LEDs with different TCL (ITO-based) conditions have been studied. It is essential to understand the thermal stability and metallurgy of metals/GaN contact in addition to developing low resistance ohmic system.

In this study, the specific contact resistances (ρ_c) of *p*-type GaN with different TCL (ITO-based) conditions have been studied. The surface morphology change has been characterized by scanning electron microscopy (SEM) and x-ray diffraction (XRD) analysis. We will also discuss the life tests of these LED samples at high current stress, such as leakage current and light output variation. Transmission electron microscopy (TEM) and energy dispersive X-ray spectrometer (EDS) studies have been used to observe the interface between TCL and *p*-type GaN. This study can clearly characterize the influences of the thermal stability of metal contact layers on GaN-based LEDs compared with the electrical properties and life tests.

6.2 Experiments

6.2.1 Growth of GaN based LED wafers with n^+-short period superlattice tunnel contact layer

The blue GaN-based MQW LEDs wafers were grown by metal organic chemical vapor deposition (MOCVD) on c-plane sapphire substrate. Trimethylgallium (TMGa), trimethylindium (TMIn), and ammonia (NH_3) were used as Ga, In, and N precursors respectively. The layer structure consists of a GaN buffer layer, followed by a 1.5-μm undoped GaN layer, a 3-μm Si-(*n*) doped GaN layer ($n \sim 1\times10^{18}$ cm^{-3}), the active layer, a 0.12-μm-thick Mg-(*p*) doped AlGaN cladding layer ($p \sim 5\times10^{17}$ cm^{-3}), and a Mg-(*p*) doped GaN contact layer ($p \sim 7\times10^{17}$ cm^{-3}). The active region, consisting of seven 5 nm/15 nm InGaN/GaN quantum wells is embedded in the region between *p*-type and *n*-type layers. For some samples, we subsequently deposited a Si-doped n^+-$In_{0.23}Ga_{0.77}N$-GaN (5/5 Å) SPS structure on top of the *p*-GaN layer. From Hall measurements, it was found that the average carrier concentration of this SPS structure is around $\sim 10^{19}$ cm^3.

6.2.2 Fabrication of GaN based LEDs with various TCL conditions

The LEDs were fabricated using standard lithography. In the first process step, a mesa was defined with standard photolithography and etched down into the *n*-type region by inductively coupled plasma reactive ion etching (ICP-RIE) technology. The transparent contact layer (TCL) was deposited by e-beam evaporation and defined on the *p*-GaN region, and then annealed with temperature ranging from 300 to 700 ºC in air ambient for 15 min. The various TCL conditions of the samples are given in Table 6-1, and the conditions of LED samples are shown in Table 6-2. The Ni (4 nm) and Ni/Au (4/3.5 nm) on the LED-C and D were preannealing at 550 °C in air for 15 min respectively. Then, ITO film (250 nm) was deposited by e-beam evaporation at 300 °C in O_2 atmosphere, followed by the annealing process at 600 °C in air for 15 min. For *n*-type GaN, low resistance ohmic contacts around 10^{-5}~10^{-8} Ω cm^2 range have been obtained using Ti/Al metals series. [12] The Ti/Al/Ti/Au (10 nm/400 nm/150 nm/800 nm) metals for the *n*-contact and bonding pad were then deposited with e-beam evaporation, followed by the annealing process at 300 °C with continuous nitrogen flow for 5 min. All the annealing processes were performed in a furnace.

Multiple annular patterns with interspacing of 5, 10, 20, 30, and 40 μm were used to measure the ρ_c values by a circular transmission line model method (CTLM) after evaporation, photolithography process, and alloy was carried out at temperature in the range of 300-700 °C during 15 min in air ambient.

6.2.3 Measurements and analyses

The wafers were then cut into chips, which were packaged onto TO-can. During the life testing, these chips with TO-can form were stressed by a 50 mA current injection at 25°C and

a relative humidity of 40 %. Some chips were then thermal treated with different temperatures in a furnace with continuous nitrogen flow in 15 min. The electrical characteristics were measured at room temperature with HP-4155 *I-V* analyzer. The SEM surface images were taken with Hitachi S-4000 instrument. For TEM measurements, the specimens were carried out by JEOL JEM-2010 microscope operated at 200 kV.

6.3 Results and Discussions

6.3.1 Electrical properties of GaN based LEDs with various TCL conditions after thermal treatment

Figure 6-1 shows the specific contact resistances of samples as a function of annealing temperature. The minimum specific contact resistances of the contacts are summarized in Table 6-3. The lowest specific contact resistance as low as 2.4×10^{-4} Ω cm^2 can be achieved for 250 nm-thick ITO (TCL-E) alloyed at 600 °C. The low value of 4.6×10^{-4} Ω cm^2 was also obtained for the Ni/Au contact (TCL-B) annealed at 500 °C. However, while the annealing temperature increase up to 700 °C, the specific contact resistances increase and the degradation of the contact behaviors can be observed. For TCL-A and TCL-C contacts, the higher specific contact resistances (>10^{-2} Ω cm^2) were obtained, and slight variations in specific contact resistances were observed up to annealing at 700 °C. This clearly shows that the Ni transferred to nickel oxide (NiO) was effective in enhancing thermal stability.

Figure 6-2 shows the SEM images and XRD spectra of Ni film on the GaN surface. From Fig. 6-2(a) and 6-2(b), the different surface morphology between as-deposited Ni film and after annealing at 550 °C in air can be observed. According to Fig. 6-2(c), the surface morphology change was mainly due to the Ni film being transformed to NiO. Figure 6-2(c) shows that Ni film preannealed at 550 °C in air transformed to NiO and a small amount of

nickel nitride. In previous reports [13-16], observation revealed a large percentage of GaN surface area was still in direct contact with NiO. Thus, we suggest that the TCL of LED-C consist of a NiO/ITO bilayer, and resulting in increasing contact resistance.

The *I-V* characteristics of the GaN based LEDs with various TCL conditions are plotted on a semi-logarithmic scale in Fig. 6-3. In the forward bias region, similar *I-V* characteristics with the ideality factor (n) around 3.0 can be seen under different TCL conditions. The ideality factors observed are 3.0 for LED-B, 3.3 for LED-D/E, and 3.6 for LED-C. This indicates that the injected carrier recombination current in the space charge region is a major mechanism of the current transport. [17] For comparison, the dotted line shows a slope with the ideality factor n=3 for room temperature. Thus, similar electron-hole recombination behavior can be expected in these LEDs. From *I-V* curves, the LEDs (B, D, and E) showed almost the same operating voltage of 3.2 V at a forward current of 20 mA. In the LED-C curve, an increase of the parasitic series resistance and higher operating voltage (approximated 3.6 V) was obtained, which can be attributed to degradation of the TCL ohmic contact on top of the *p*-type GaN. In the reverse bias region, the leakage currents (<1 μA) at -5 V were slightly different with various TCL conditions.

The *I-V* characteristics of the GaN LEDs at different thermal treatment temperatures are shown in Fig. 6-4. In the forward bias region, similar *I-V* characteristics with the ideality factor (n) around 3.2 can be seen for LED-B, LED-D and LED-E thermal treated at 600 °C. The LEDs (B, D, and E) thermal treated at 600 °C showed almost the same operating voltage of 3.6 V at a forward current of 20 mA. In the *I-V* curve of LED-C thermal treated at 600 °C, an increase of the parasitic series resistance and higher operating voltage (approximated 4.7 V) was obtained, which can be attributed to degradation of the TCL ohmic contact on top of the *p*-type GaN. In the reverse bias region, the leakage currents of LEDs thermal treated at 600 ºC at reverse biases of 5 V were observed within 1 μA.

While the annealing temperature at 700 ºC, the electrical short circuit behavior can be

observed for LED-B, LED-D and LED-E and these LEDs become lightless. Thus, a leakage path may be formed as the annealing temperature increase. However, the LED-C thermal treated at 700 ºC still showed normal *I-V* characteristic. In the *I-V* curve of LED-C thermal treated at 700 °C, the leakage current at -5 V was no variation, and the parasitic series resistance and operating voltage were increase higher than thermal treated at 600 °C. Thus, we suggested that Ni film preannealed at 550°C in air was transformed to NiO, and the TCL of LED-C consisted of a NiO/ITO bilayer, resulting in increasing contact resistance.

6.3.2 Life tests of GaN based LEDs with various TCL conditions by current injection

Figure 6-5 and 6-6 show the results of reliability tests by stressed at 50 mA and 25°C, conducted on LEDs of the four types shown in Table 6-1 and 6-2. The life tests of reverse leakage current variation (at -5 V), as shown in Fig. 6-5, the leakage current variation is the ratio (Ir/Ir_0) of leakage current (Ir) to initial leakage current (Ir_0). It was found that leakage current increased rapidly after 168 hours for LED-E. Small increases of leakage currents for LED-B and LED-D were obtained after life tests. In contrast, a slight increase in leakage current could be found from LED-C even with an 840-hour burn-in test. In Fig. 6-6, the life tests of light output variation (at 50 mA) were consistent with the life tests of reverse leakage current. It could be observed that the optical output power was deteriorated by 10.8% for LED-E. Figure 6-5 and 6-6 show that GaN based LEDs with ITO upper contact were unreliable after a longer burn-in test (stressed by 50 mA). Compared with only an ITO contact layer (LED-E), the NiO/ITO contact layer (LED-C) was very stable even with an 840-hour burn-in test. These results are probably due to the NiO barrier layer that will block the leakage pathway. Recently, Weidemann *et al.* have demonstrated that preferential oxidation of threading dislocations (TDs) causes selective passivation of leakage current paths. [18] From our other experiments, NiO film can be successfully prepared by annealing process. The

resistivity and sheet resistance of the NiO films are very poor (resistivity=36.6 Ω cm, sheet resistance= 6.73×10^{6} Ω/□). We suggest that nickel oxide may be similar to other oxide such as silicon oxide and gallium oxide. Thus, the NiO thin film in this case may prevent metals indiffusion along defects or dislocations.

6.3.3 Observation of interfaces between contact metals and GaN based LEDs

To further understand and confirm the influences of the contact interfaces between contact layers and the *p*-type GaN layer, we carried out TEM and EDS studies. Figure 6-7 shows the cross-sectional micrograph of the LED structure before coating contact metal (TCL). The straight threading dislocations (TDs) were definitely seen in the LED structure. It was observed clearly that the upper *p*-GaN layer was very flat and intact. The image of the LED-E structure as shown in Fig. 6-8, ITO film contact on the *p*-GaN layer was obviously exhibited. In contrast with Fig. 6-7, the interface geometry changed substantially when it was annealed at 600 °C. Numerous nanoscale dark points formed in the GaN just under the interface. It appears that the interface between the ITO layer and *p*-GaN had been transformed after annealing at 600 °C. Under higher magnification, as shown in Fig. 6-9, the interface should be observed more clearly. The chemical compositions of the exposed regions, marked as "a" in Fig. 6-9, were analyzed by EDS. The Ga, In, and Sn peaks were detected as shown in Fig. 6-10(a). In the *p*-GaN layer, marked as "b" in Fig. 6-9, only the Ga peak was observed as shown in Fig. 6-10(b). The Au and Cu signals are the background and copper ring, respectively. According to the results of EDS analyses, it clearly indicates that ITO can react with *p*-GaN not only at TDs (or V-defects) interfaces but also at other interfacial regions.

A similar phenomenon in interfacial reactions of Ti/n-GaN contacts at elevated temperature has been reported. [19] According to the above-mentioned results, we suggest that the ITO layer can react with the *p*-GaN layer to easily form an In-Ga solid solution near

the interface due to the lower eutectic temperature (15.3 °C) of the Ga-In phase system, as shown in Fig. 6-11. In contrast, Ni film on *p*-GaN was preannealed at 550°C in air to transform discontinuous NiO film. The discontinuous NiO film may prevent the ITO film from covering completely. The ITO film can also react with the *p*-GaN layer at partial interface, but the part of the TDs (or V-defects) interfaces maybe not react due to NiO protection. The schematic drawing illustrations show ITO/*p*-GaN interface and NiO/ITO/*p*-GaN interface as shown in Fig. 6-12.

Figure 6-13 shows the TEM cross-sectional image of LED-D after thermal treated at 700 °C. The straight TD can be found on $(1\bar{1}00)$ plane, and MQW structure can be also observed. Using the EDS analyses, the compositions were analyzed. There are three interesting regions: the *p*-GaN layer marked as "a" in Fig. 6-13, nanoscale dark point (V-defect) marked as "b" in Fig. 6-13, and the TD marked as "c" in Fig. 6-13. Figure 6-14 shows the EDS spectra of these regions. In "a" region of *p*-GaN layer, the main compositions are Ga and Cu as shown in Fig. 6-14(a). The Cu signal is the background of copper ring. In "b" region of V-defect, the Ga, Ni, Au, In, and Sn peaks were detected as shown in Fig. 6-14(b). In "c" region of TD, the weak signals of Ni, Au, In, and Sn can be also observed clearly in the TD region as shown in Fig. 6-14(c). According to the results of EDS analyses, it clearly indicates that metals could react with *p*-GaN layer at V-defect place and diffuse through MQW along the dislocations, which causes a leakage path when annealing temperatures reach 700 ºC and hence the short circuits as shown in Fig. 6-4.

From these results, we suggest that surface pits and the connected dislocations in GaN based LEDs may enhance contact metal migration along the dislocations, leading to further increases in junction leakage, and eventually to serious failure. Based on the results obtained in this study, we suggest that the LED-E was degraded with unstable interfaces after life tests (stressed by a 50 mA current injection). The ITO reacts with the *p*-GaN layer to form an In-Ga

solid solution near the interface, resulting in metals (In or Sn) indiffusion easily during burn-in tests. We consider that In (or Sn) would also indiffuse along the TDs during high current stress, resulting in degradation. The LED-C has good reliability due to the NiO barrier layer. The barrier layer can prevent ITO film from reacting with GaN at TDs positions and may block the metals indiffusion along dislocations. Thus, our studies provide the evidence that the diffusion of the metallic component along the dislocations is a main degradation mechanism of devices in the annealing process.

6.4 Conclusions

We have investigated the influences of contact interfaces between the ITO-based layer and GaN LEDs. The lowest specific contact resistance of 2.4×10^{-4} Ω cm^2 can be achieved for 250 nm ITO contact alloyed at 600 °C. After thermal treated at 700 °C, the electrical short circuit behavior of LEDs contact with metals has been observed. The GaN-based LED with a pure ITO contact layer had poor reliability at high current injection life tests. Furthermore, we also found that the GaN-based LED could achieve good reliability with the NiO/ITO contact layer. In-contained metallic interfaces were observed between the *p*-GaN and the pure indium tin oxide (ITO) contact layer by TEM and EDS analyses. These results imply that the ITO would react at interface or indiffuse near interface at 600°C. The indium (or Sn) would diffuse into an active region along the TDs easily during high current injection life tests. To improve the reliability of GaN-based LEDs with the ITO contact layer, a NiO layer could be used to prevent the reaction and block the leakage pathway. The Ni film transferred to nickel oxide (NiO) was effective in enhancing thermal stability. Both TEM and EDS analyses reveal that the core of the TD contains contact metals after thermal treated at 700 °C. These results imply direct evidences that the migration and in-diffusion of contact metals along the TDs cause the short circuit characteristics of the *p*-*n* junction at high temperatures. Thus, we suggested that

using a NiO layer could prevent the reaction and block the leakage pathway.

6.5 References

[1] S. Nakamura, M. Senoh, S. I. Nagahama, N. Iwasa, T. Yamada, T. Matsushita, H. Kiyoku and Y. Sugimoto, Jpn. J. Appl. Phys. **35**, L74 (1996).

[2] A. K. Fung, J. E. Borton, M. I. Nathan, J. M. Van Hove, R. Hichman II, P. P. Chow and A. M. Wowchak, J. Electron. Mater. **28**, 572 (1999).

[3] J. K. Kim and J. L. Lee, J. Electrochem. Soc. **149**, G266 (2002).

[4] H. W. Jang, W. Urbanek, M. C. Yoo and J. L. Lee, Appl. Phys. Lett. **80**, 2937 (2002).

[5] J. K. Ho, C. S. Jong, C. C. Chiu, C. N. Huang, K. K. Shih, L. C. Chen, F. R. Chen and J. J. Kai, J. Appl. Phys. **86**, 4491 (1999).

[6] J. K. Sheu, Y. K. Su, G. C. Chi, M. J. Jou, C. C. Liu and C. M. Chang, Solid-State Electron. **43**, 2081 (1999).

[7] R. H. Horng, D. S. Wuu, Y. C. Lien and W. H. Lan, Appl. Phys. Lett. **79**, 2925 (2001).

[8] S. J. Chang, M. L. Lee, J. K. Sheu, W. C. Lai, Y. K. Su, C. S. Chang, C. J. Kao, G. C. Chi and J. M. Tsai, IEEE Electron Device Lett. **24**, 212 (2003).

[9] Y. K. Su, S. J. Chang, C. H. Chen, J. F. Chen, G. C. Chi, J. K. Sheu, W. C. Lai and J. M. Tsai, IEEE Sensors J. **2**, 366 (2002).

[10] Y. C. Lin, S. J. Chang, Y. K. Su, C. S. Chang, S. C. Shei, J. C. Ke, H. M. Lo, S. C. Chen and C. W. Kuo, Solid-State Electron. **47**, 1565 (2003).

[11] S. Nakamura, M. Senoh, S. I. Nagahama, N. Iwasa, T. Yamada, T. Matsushita, Y. Sugimoto and H. Kiyoku, Jpn. J. Appl. Phys. **36**, L1059 (1997).

[12] S. N. Mohammad, J. Appl. Phys. **95**, 7940 (2004).

[13] J. K. Ho, C. S. Jong, C. C. Chiu, C. N. Huang and K. K. Shih, Appl. Phys. Lett. **74**, 1275 (1999).

[14] D. Qiao, L. S. Yu, S. S. Lau, J. Y. Lin, H. X. Jiang and T.E. Haynes, J. Appl. Phys. **88**, 4196 (2000).

[15] J. K. Ho, C. S. Jong, C. C. Chiu, C. N. Huang, K. K. Shih, L. C. Chen, F. R. Chen and J. J. Kai, J. Appl. Phys. **86** 4491 (1999).

[16] L. C. Chen, F. R. Chen, J. J. Kai, L. Chang, J. K. Ho, C. S. Jong, C. C. Chiu, C. N. Huang, C. Y. Chen and K. K. Shih, J. Appl. Phys. **86** 3826 (1999).

[17] J. M. Shah, Y. L. Li, T. Gessmann and E. F. Schubert, J. Appl. Phys. **94**, 2627 (2003).

[18] O. Weidemann, E. Monroy, E. Hahn, M. Stutzmann and M. Eickhoff, Appl. Phys. Lett. **86**, 083507 (2005).

[19] C. J. Lu, A. V. Davydov, D. Josell and L. A. Bendersky, J. Appl. Phys. **94**, 245 (2003).

Table 6-1 The various transparent contact layer conditions.

Sample	Transparent contact layer (TCL)
TCL-A	Ni (4 nm)
TCL-B	Ni/Au (4/3.5 nm)
TCL-C	Ni (4 nm) preannealed at 550 ^{o}C in air for 15 min + ITO (250 nm)
TCL-D	Ni /Au (4/3.5 nm) preannealed at 550 ^{o}C in air for 15 min + ITO (250 nm)
TCL-E	ITO (250 nm)

Table 6-2 The conditions of the LED samples.

LED sample	Transparent contact layer (TCL) condition
LED-B	TCL-B annealed at 600 ^{o}C in air for 15 min
LED-C	TCL-C annealed at 600 ^{o}C in air for 15 min
LED-D	TCL-D annealed at 600 ^{o}C in air for 15 min
LED-E	TCL-E annealed at 600 ^{o}C in air for 15 min

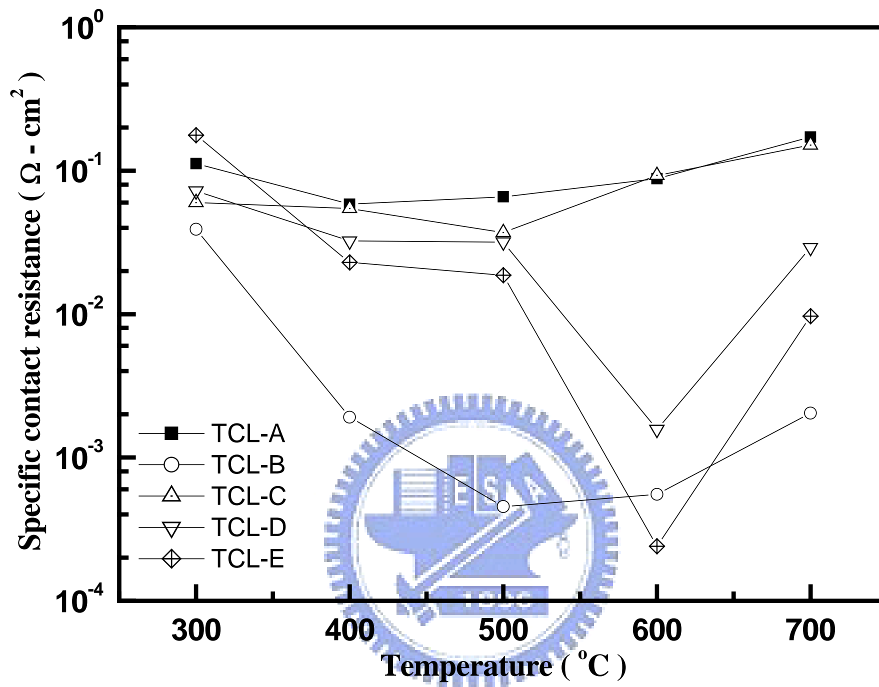

Figure 6-1 The specific contact resistances of all the samples as a function of annealing temperature.

Table 6-3 The minimum specific contact resistances of the metals contact.

Sample	Annealing temperature (^{o}C)	Specific contact resistances (Ω cm^2)
TCL-A	400	5.8×10^{-2}
TCL-B	500	4.6×10^{-4}
TCL-C	500	3.7×10^{-2}
TCL-D	600	1.6×10^{-3}
TCL-E	600	2.4×10^{-4}

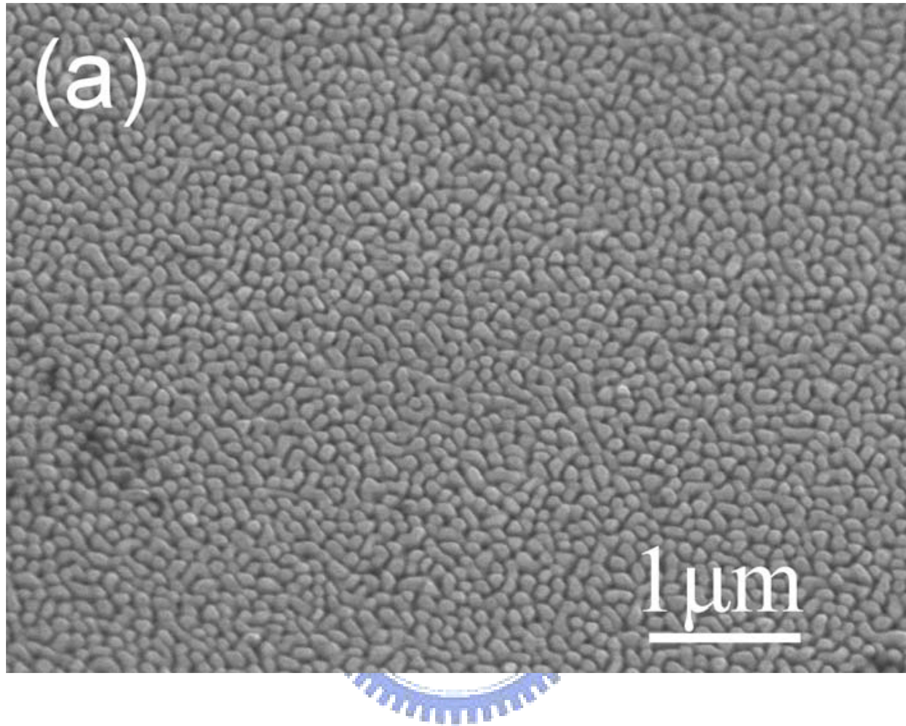

Figure 6-2(a) SEM image of as-deposited Ni film on GaN surface.

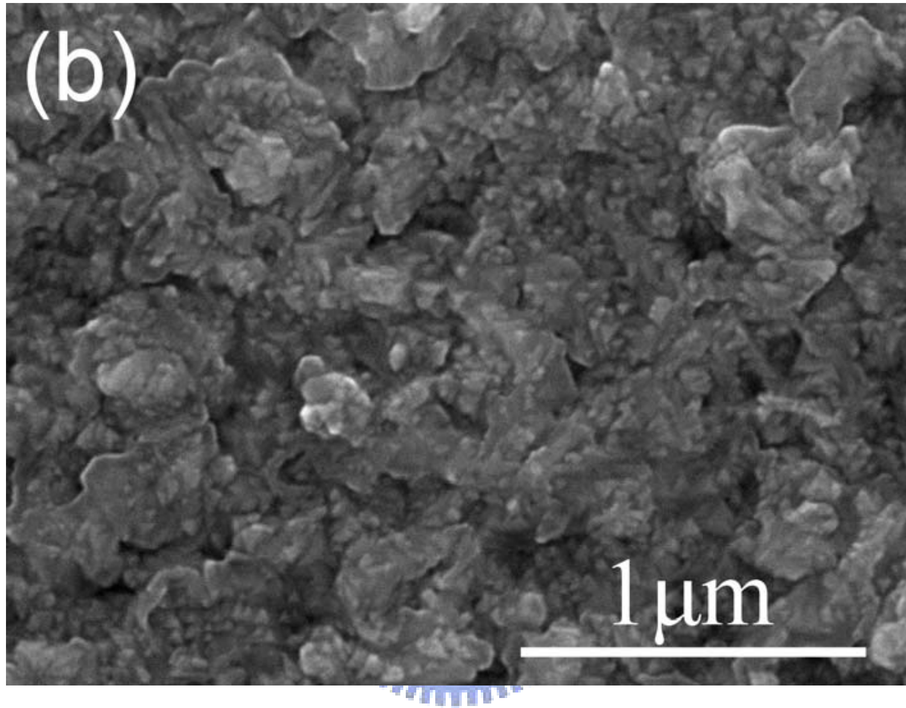

Figure 6-2(b) SEM image of Ni film on GaN surface after annealing at 550 °C in air for 15 min.

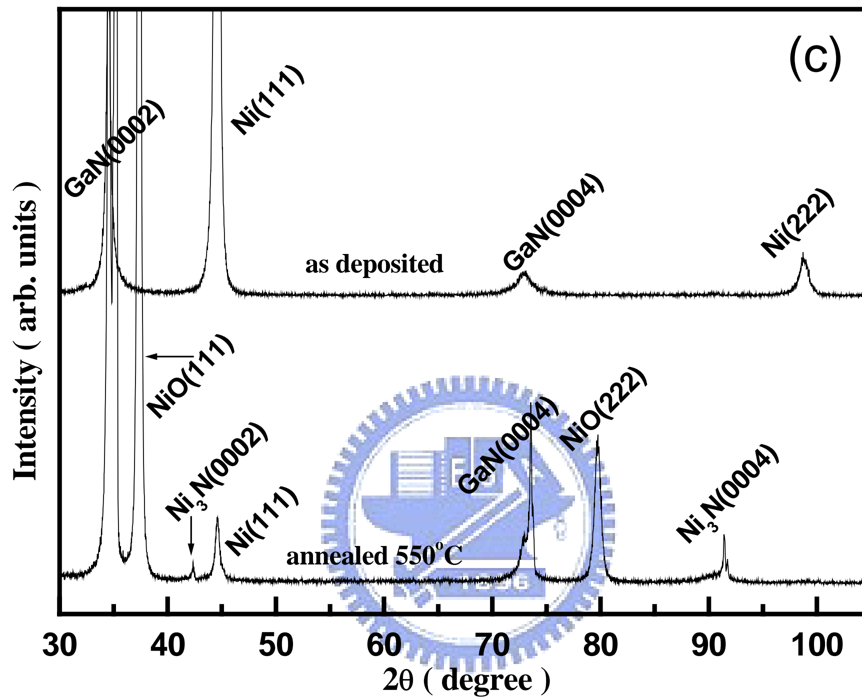

Figure 6-2(c) XRD spectra of as-deposited Ni film and after annealing at 550 °C on GaN surface respectively.

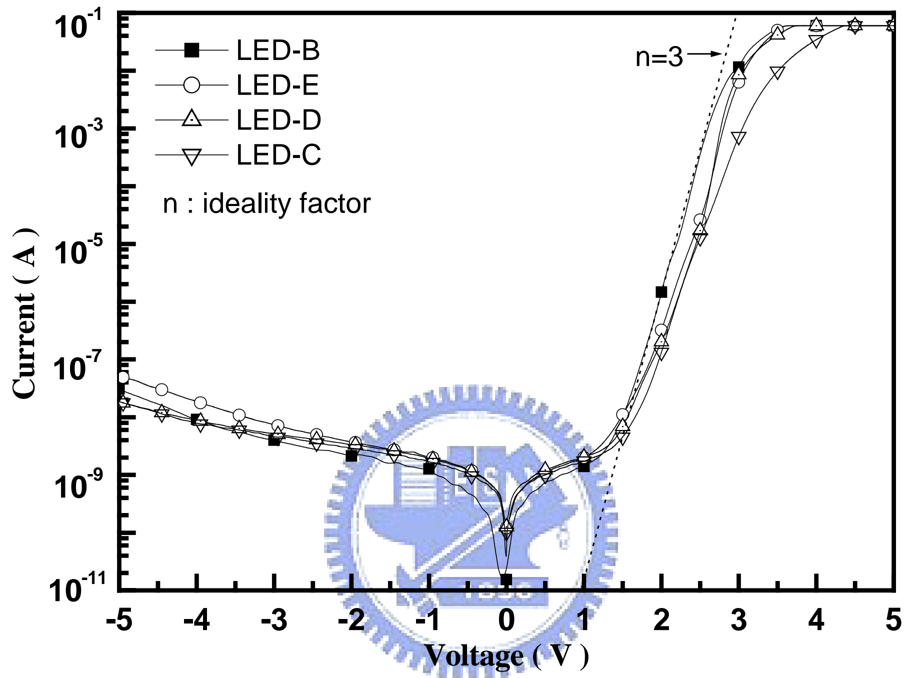

Figure 6-3 *I-V* characteristics of GaN based LEDs with various TCL conditions.

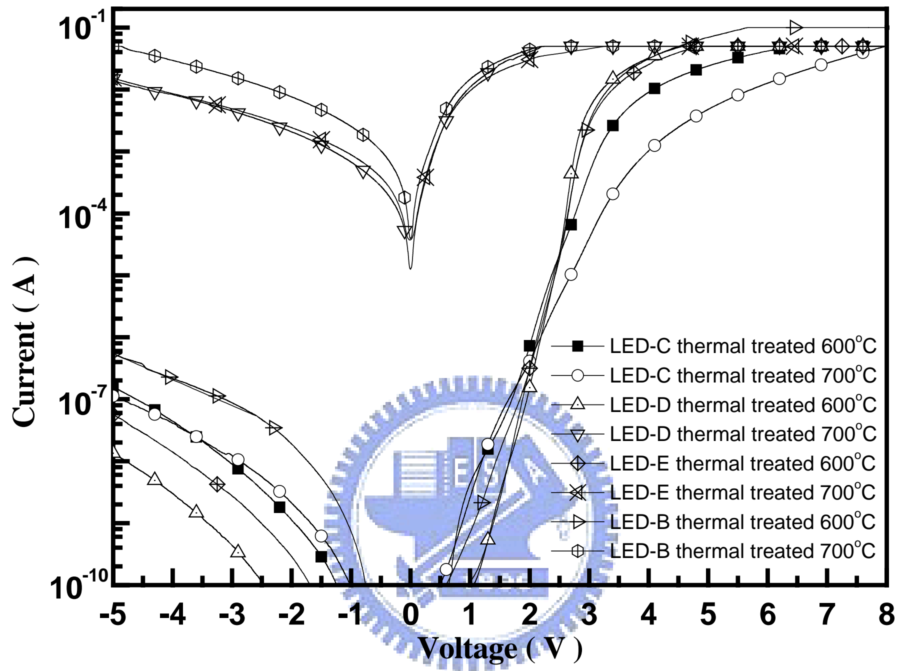

Figure 6-4 *I-V* characteristics of GaN based LEDs with various TCL conditions after thermal treated at 600 and 700 ºC.

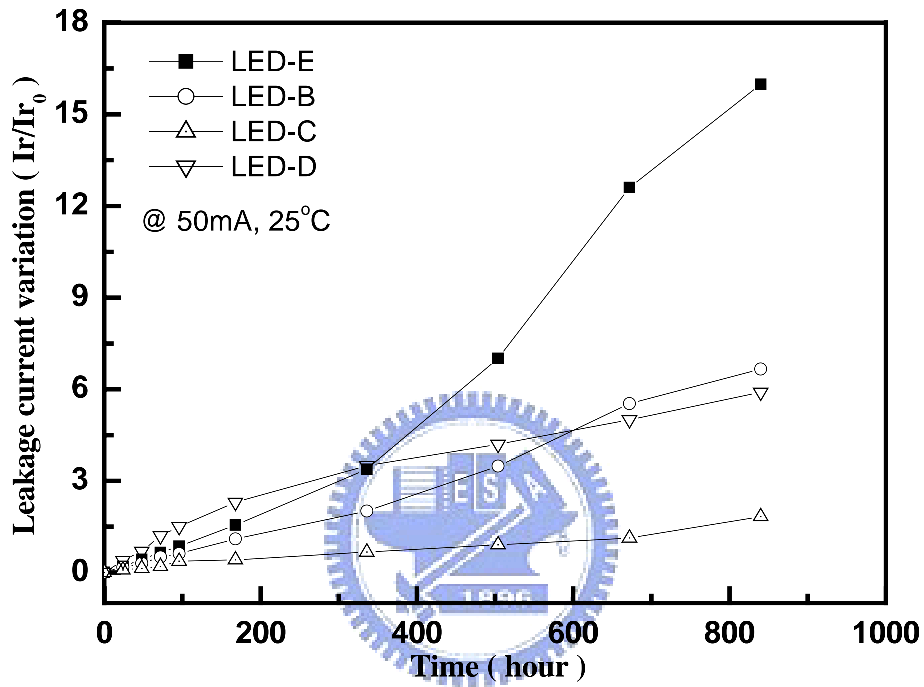

Figure 6-5 Life tests of reverse leakage current variation (at -5 V) from GaN based LEDs with various TCL conditions by stressed at 50 mA and 25 °C.

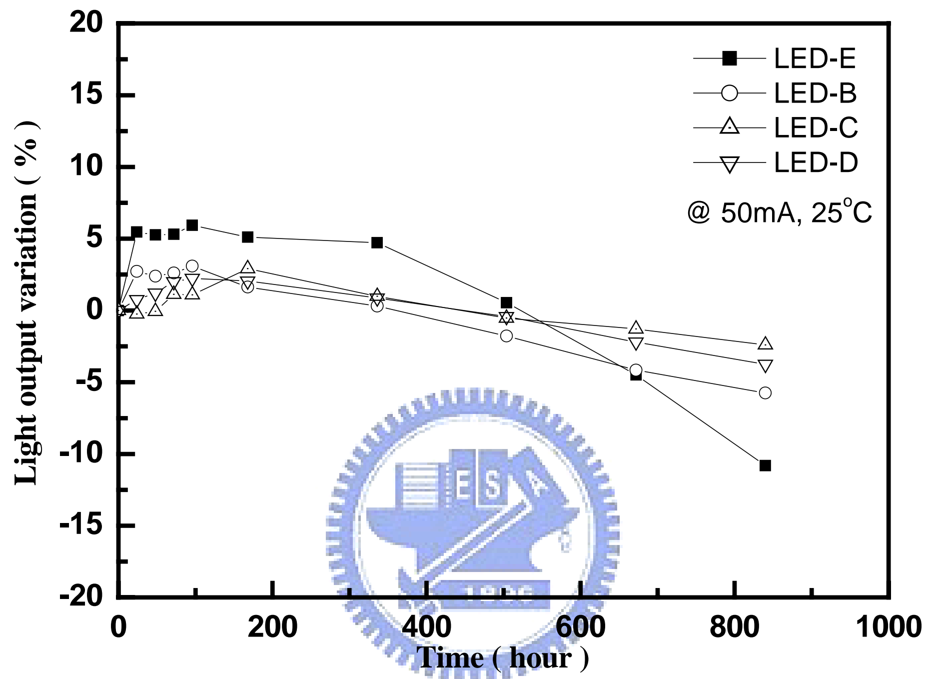

Figure 6-6 Life tests of light output variation from GaN based LEDs with various TCL conditions by stressed at 50 mA and 25 °C.

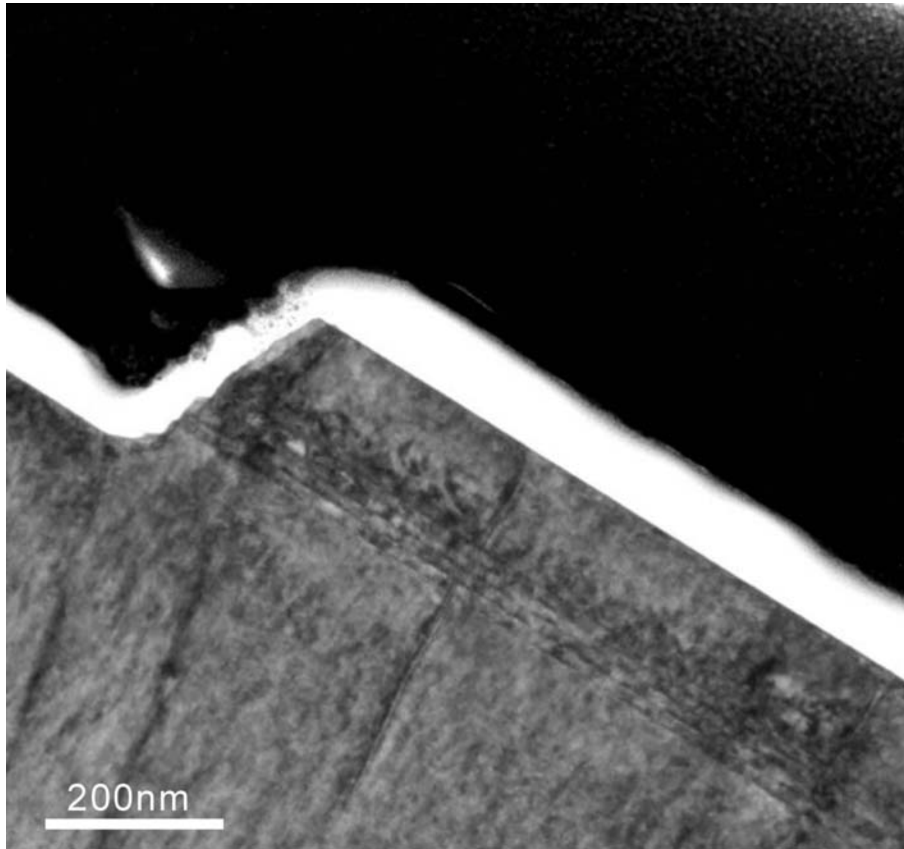

Figure 6-7 Cross-section bright-field TEM micrograph of the LED structure before coating contact metal (TCL).

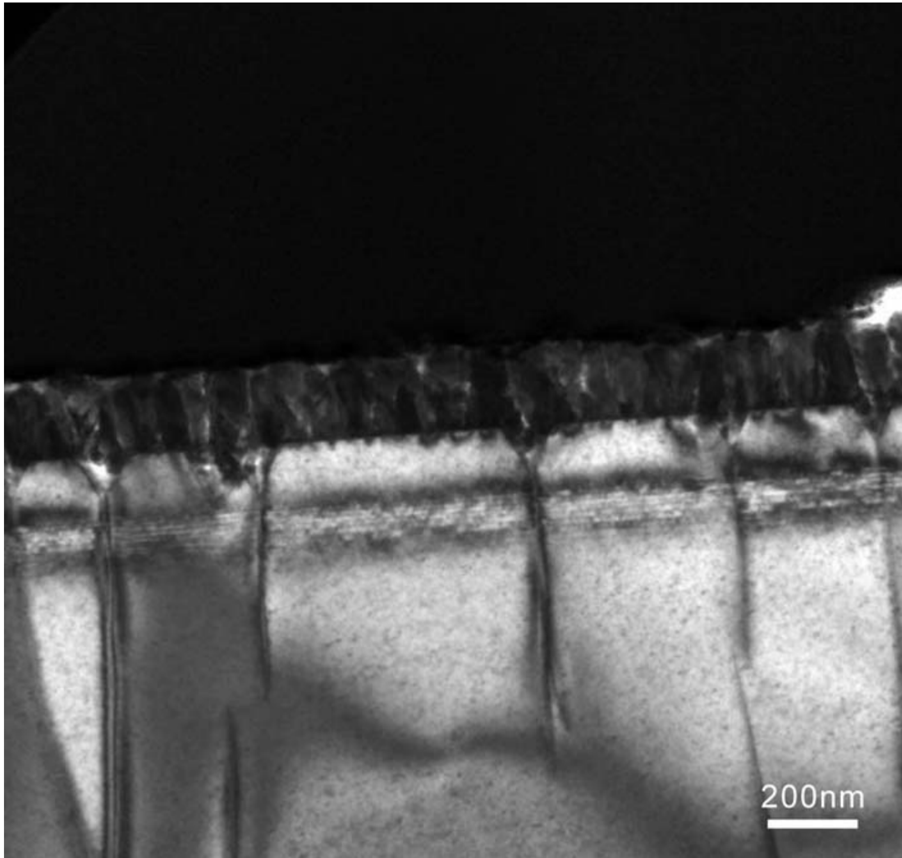

Figure 6-8 Cross-section bright-field TEM micrograph of the LED-E structure.

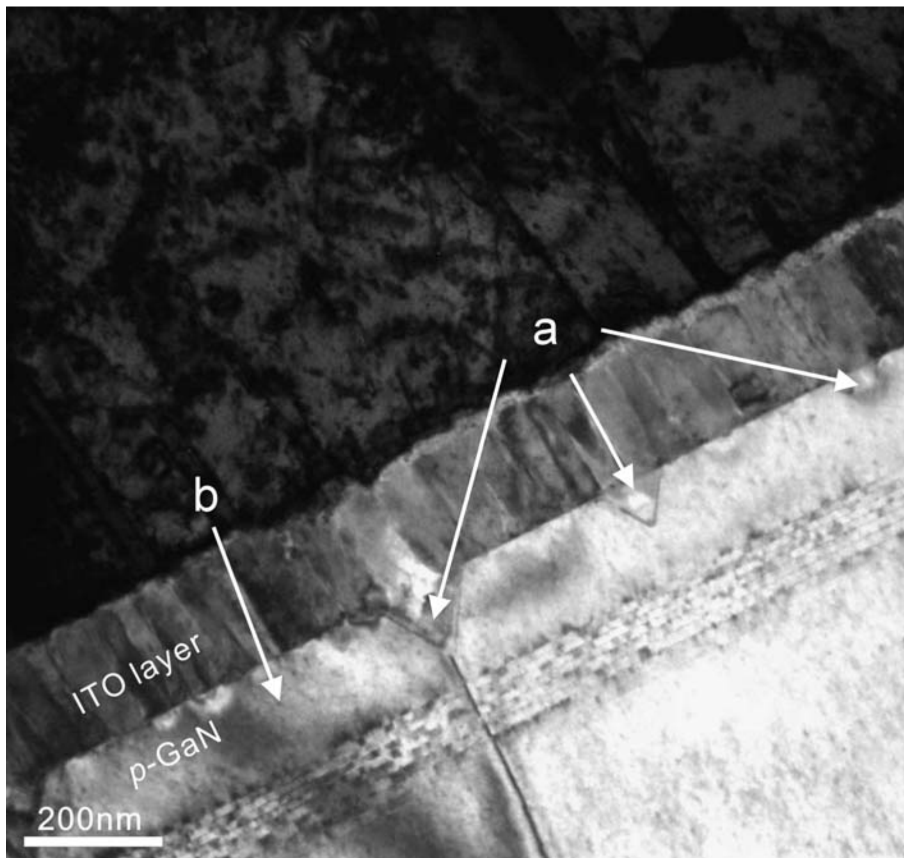

Figure 6-9 Cross-section bright-field TEM micrograph of the LED-E structure with higher magnification image.

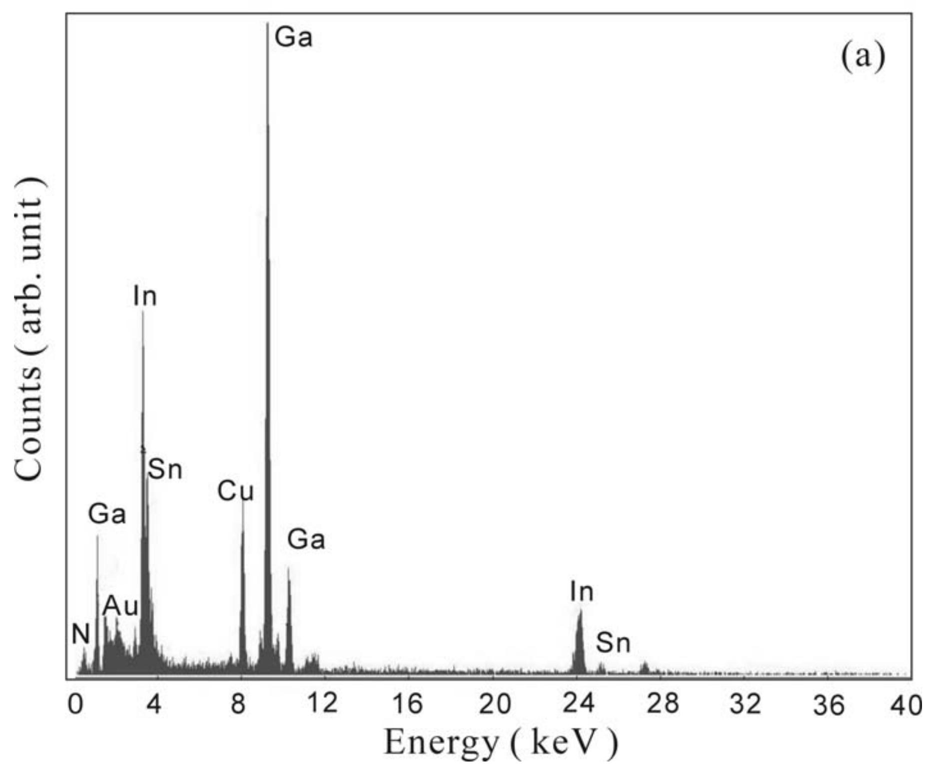

Figure 6-10(a) EDS spectrum obtained at “a” of Fig. 6-9.

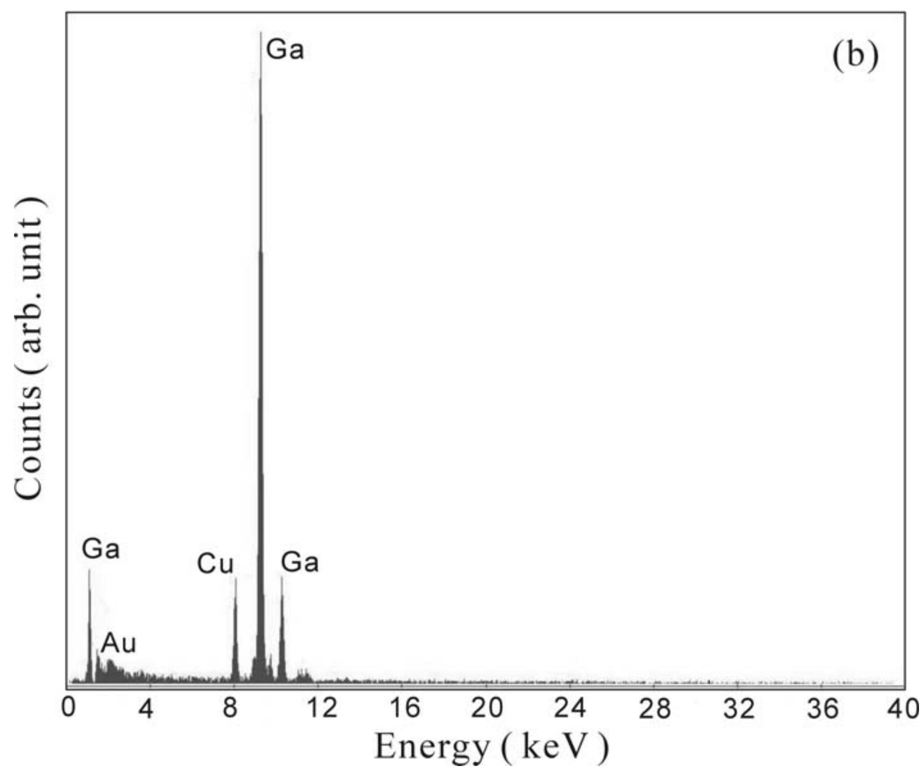

Figure 6-10(b) EDS spectrum obtained at “b” of Fig. 6-9.

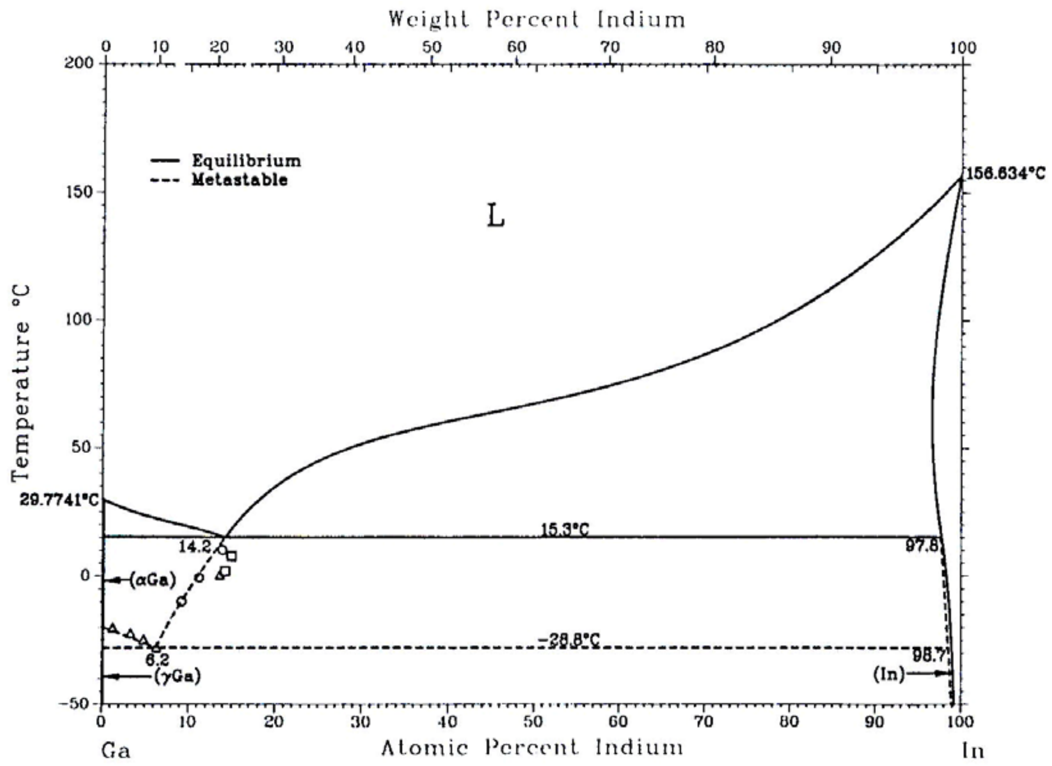

Figure 6-11 Ga-In phase system.

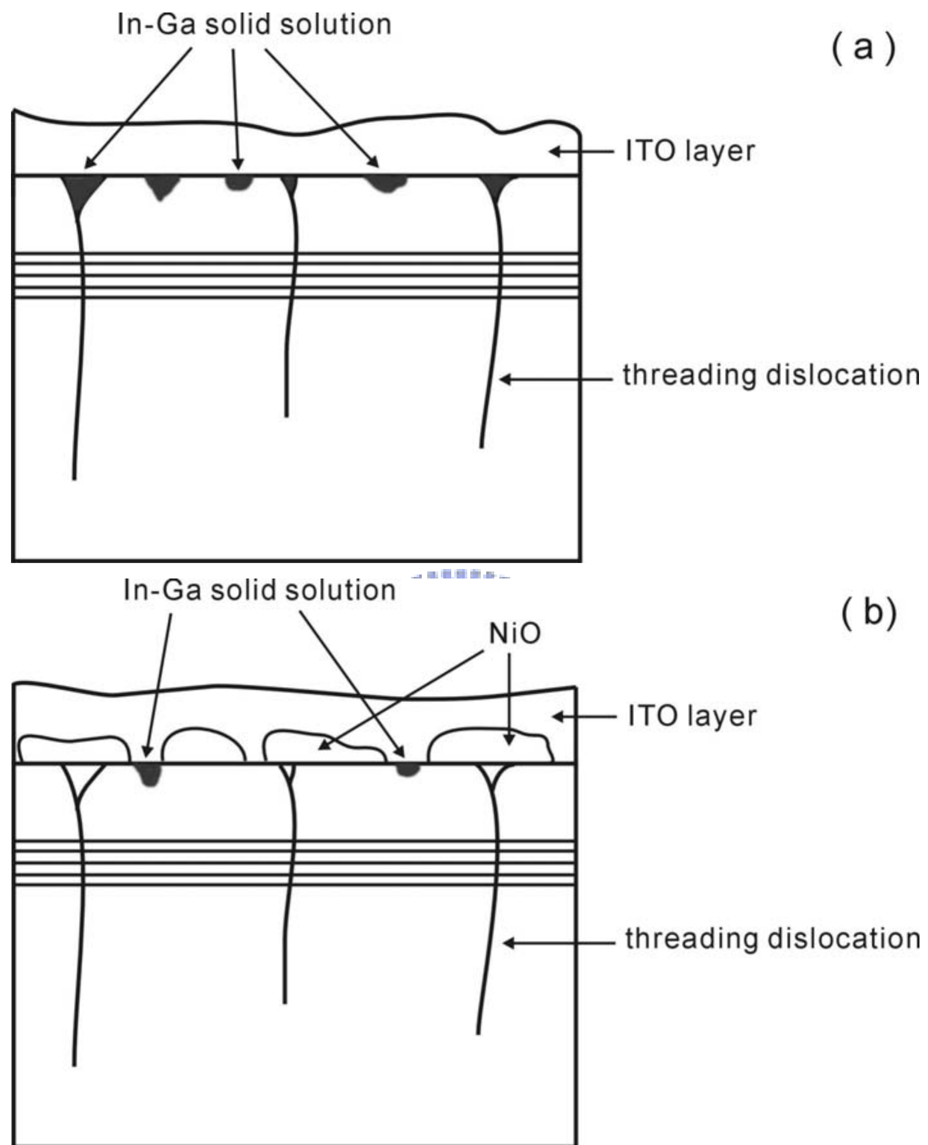

Figure 6-12 Schematic drawing illustration of (a) ITO and *p*-GaN interface and (b) NiO/ITO and *p*-GaN interface.

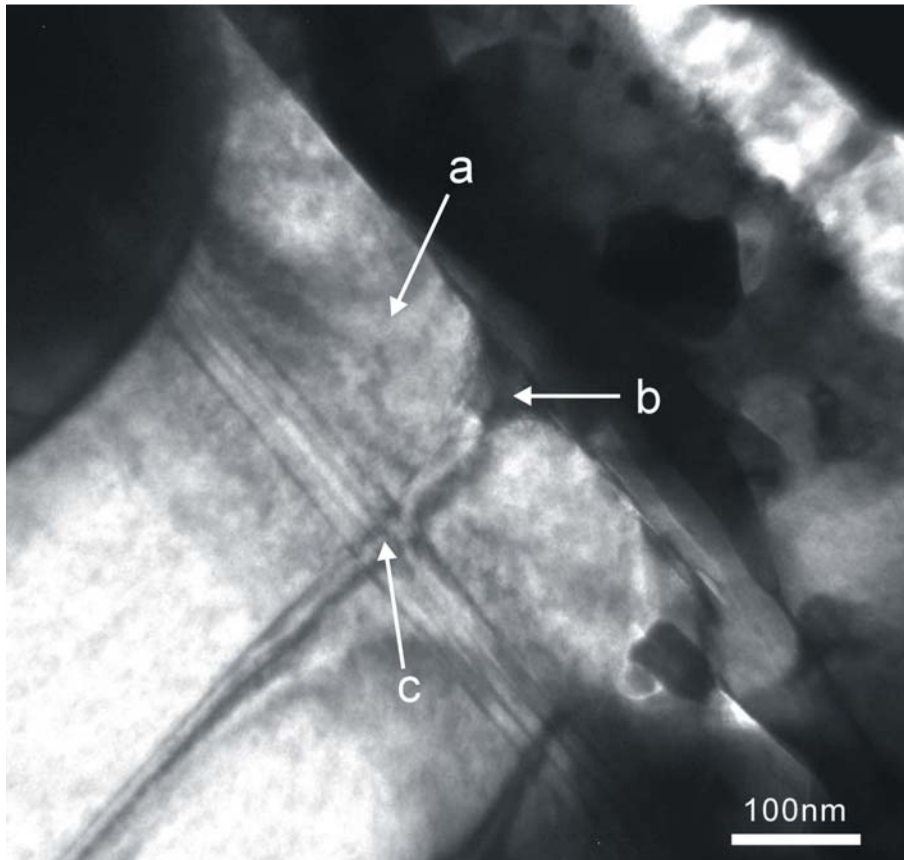

Figure 6-13 Cross-section bright-field TEM micrographs of LED-D after thermal treated at 700 °C.

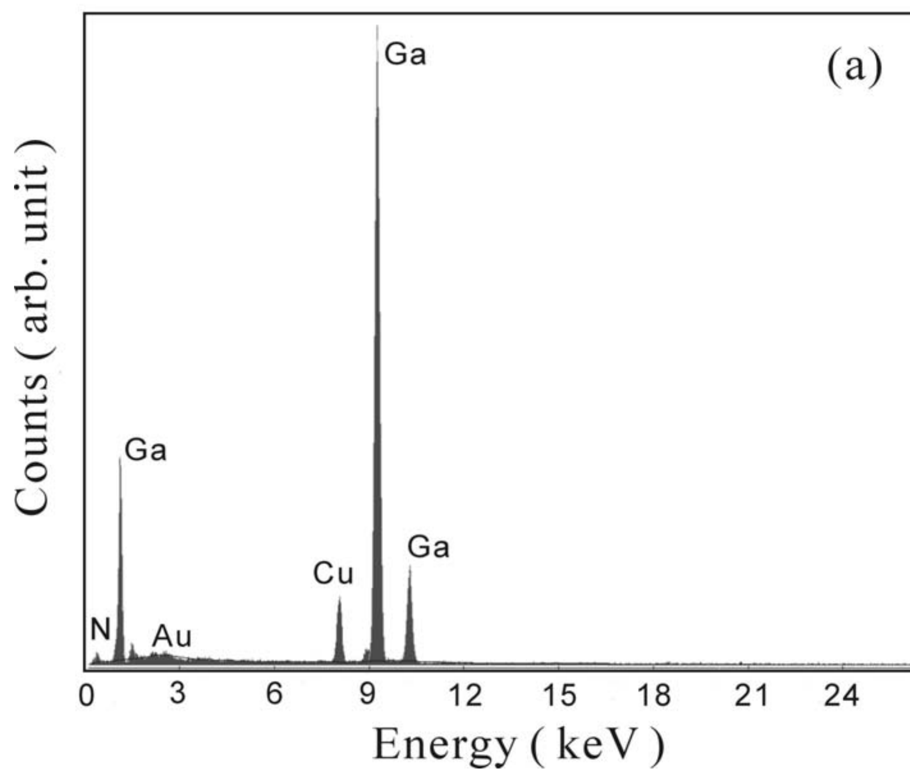

Figure 6-14(a) EDS spectrum obtained at “a” of Fig. 6-12.

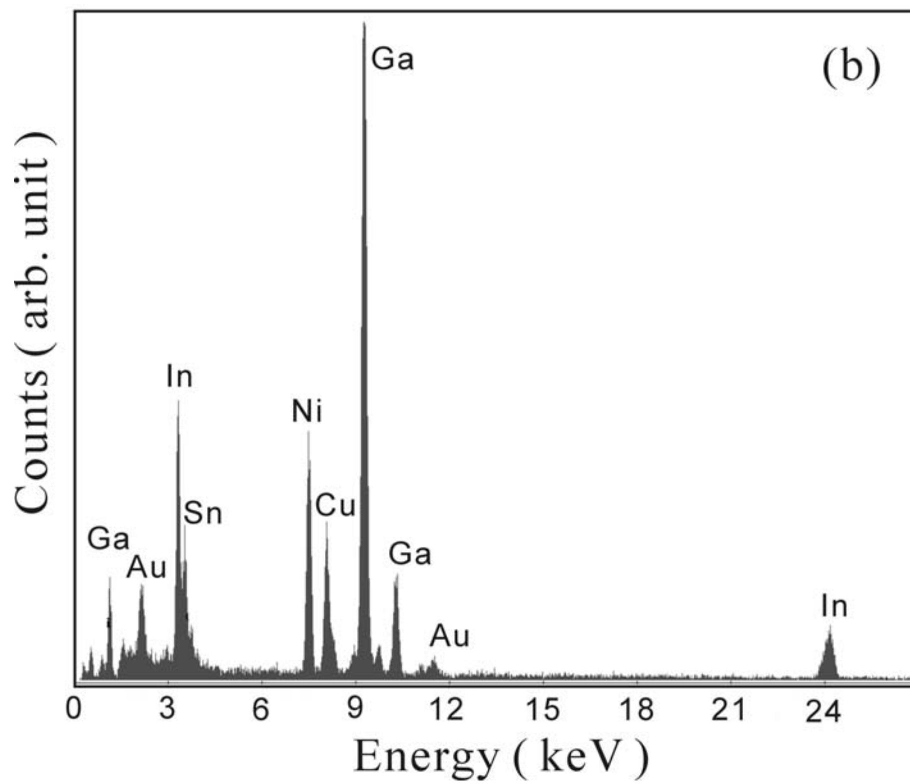

Figure 6-14(b) EDS spectrum obtained at “b” of Fig. 6-12.

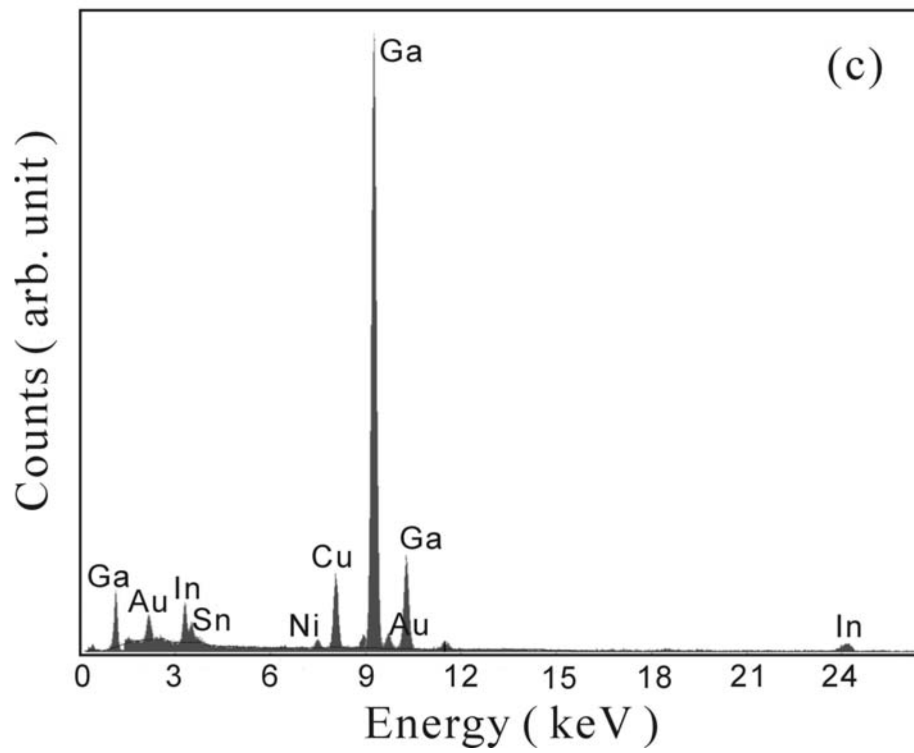

Figure 6-14(c) EDS spectrum obtained at “c” of Fig. 6-12.

CHAPTER 7

The Effect of Threading Dislocation on GaN Based LEDs with Naturally Textured Surface

7.1 Introduction

III-V nitride materials are very attractive for the fabrication of light-emitting diodes (LEDs) and laser diodes (LDs) operating in the short-wavelength part of the spectrum. Recently, as the brightness of GaN based LEDs has increased, applications such as displays, traffic signals, backlight for cell phone, exterior automotive lighting, printers, short-haul communications, and optoelectronic computer interconnects have become possible. Especially, there has been a lot of speculation about white LEDs for general illumination by using the high brightness LEDs. However, even though the brightness of LEDs continues to increase, the total light output is still low compared to that of a conventional light source in a high-flux lighting system. [1] Therefore, a better way for the light extraction through the chip and device design must be required.

In general, for a GaN based LED, the light output depends on the internal quantum efficiency of the active layer and the light extraction efficiency. The internal quantum efficiency for GaN based LEDs is smaller than 100% at room temperature due to the activation of nonradiative defects. And it is also well known that the external quantum efficiency is still much smaller than the internal quantum efficiency. The light extraction efficiency of the GaN based LED is limited mainly by the large difference in refractive index between GaN film and the surrounding air. The critical angle for photons to escape from GaN film is determined by Snell's law. For GaN based LEDs, the refractive indexes of GaN (n_{GaN}) and the air (n_{air}) are 2.5 and 1, respectively. [2] In this case, the critical angle [$\theta_c = \sin^{-1} (n_{air} /$

n_{GaN})] for the light generated in the active region to escape is about 23°. Because the light emission from the active region of a LED is a directionally isotropic and the light can escape from the chip if the angle of incidence to the chip wall is less than the critical angle, a small fraction of light generated in the active region of the LED can escape to the surrounding air. Therefore, for a conventional GaN based LED, the external quantum efficiency limits to a few percent due to the high refractive index of GaN as well as the absorption in the metal pad for current injection and free carriers, even if the internal quantum efficiency close to 100% is reached.

In order to increase light extraction efficiency from LEDs, it is very important that the photons generated into LEDs experience multiple opportunities to find the escape cone. The angular randomization of photons is achieved by surface scattering from the roughened top surface of the LEDs. There are many methods to roughen the top surface of GaN based LEDs, and one of these methods is performed by etching processes. However, the etching processes easily change the surface state of the *p*-GaN layer and thereby degrade the electrical properties of the device. [3] Methods for controlling the growth conditions to obtain rough surfaces should be superior to the etching methods. Typically, the naturally textured surface, which is most likely due to the surface termination of threading dislocations, originating from the low temperature growth condition during the growth of *p*-GaN topmost contact layer, is a well known approach. [4] In other words, the low temperature growth condition could result in many pits on the *p*-GaN surface to increase the escape probability of internal light and hence an enhancement of light extraction efficiency. Recently, Su *et al.* have reported a method to obtain rough surface. [5, 6] Their experimental results indicated that GaN based LED with the truncated pyramids on the surface exhibited an enhancement in output power of 66 % at 20 mA.

Furthermore, to enhance the output intensity of GaN based LEDs, it is necessary to reduce the contact resistance and to enhance the transmission efficiency of the upper

transparent contact layer (TCL). One possible way to achieve this is to employ indium tin oxide (ITO), instead of Ni/Au, as the *p*-contact material. Recently, several studies have discussed the applications of ITO contact layers in GaN based LEDs. [7-11]

However, for high-power applications such as projectors and flash lamps, high-power GaN based LEDs with an ITO *p*-type contact layer have been studied. [12] Since power dissipation across the *p*-GaN/metal interface generated Joule heat, failure of LEDs and LDs was due to indiffusion of the ohmic contact elements along dislocations in the GaN epilayers, leading to an electrical short of the *pn* junction. [13] Thus, it is essential to understand the effect of threading dislocation (TD) on GaN based LEDs with naturally textured surface.

In this study, we fabricate the InGaN/GaN multiple quantum well (MQW) LEDs with naturally textured surface, and compare the electrical characteristics with conventional GaN based LEDs after annealing. The surface morphology and microstructure of these LEDs with and without naturally textured surface have been characterized by scanning electron microscopy (SEM) and transmission electron microscopy (TEM) analysis. This work can clearly characterize the influences of the dislocations on GaN based LEDs with naturally textured surface compared with the electrical properties and life tests.

7.2 Experiments

7.2.1 Growth of GaN based LED wafers with naturally textured surface

The blue GaN based MQW LEDs wafers were grown by metal organic chemical vapor deposition (MOCVD) on c-plane sapphire substrate. Trimethylgallium (TMGa), trimethylindium (TMIn), and ammonia (NH_3) were used as Ga, In and N precursors respectively. During growth, biscyclopentadienyl magnesium (CP_2Mg) and disilane (Si_2H_6) were used as the *p* and *n* type doping sources, respectively. The conventional layer structure

consists of a GaN buffer layer, followed by a 1.5-μm undoped GaN layer, a 3-μm Si-(*n*) doped GaN layer (n~1×10^{18} cm^{-3}), the active layer, a 0.12-μm-thick Mg-(*p*) doped AlGaN cladding layer (p~5×10^{17} cm^{-3}), and a Mg-(*p*) doped GaN contact layer (p~7×10^{17} cm^{-3}). The active region, consisting of nine 5 nm/15 nm InGaN/GaN quantum wells is embedded in the region between *p*-type and *n*-type layers. After the growth of these layers, a growth-interruption step, stopping the TMGa flow while maintaining CP_2Mg flow, was performed at the first *p*-GaN contact layer for a short period of time (~5 min). The process is called "Mg treatment". [6] A second *p*-GaN contact layer was then grown again after this Mg treatment process. Finally, a heavily Si doped short-period superlattice (SPS) was grown on the *p*-GaN contact layer to improve the Ohmic contact of the *p*-electrode. Figure 7-1 shows a schematic layer structure of the GaN based LED with textured surface. [6]

7.2.2 Fabrication of GaN based LEDs with naturally textured surface

The LEDs were fabricated using standard lithography. In the first process step, a mesa was defined with standard photolithography and etched down into the *n*-type region by inductively coupled plasma reactive ion etching (ICP-RIE). The ITO film (250 nm) as the TCL was deposited by e-beam evaporation, defined on the *p*-GaN region, and then annealed at 600 ºC in air for 15 min. The Cr/Pt/Au (20 nm/20 nm/2000 nm) metals for the *n*-contact and *p*-contact (bonding pad) were then deposited with e-beam evaporation, followed by the annealing process at 300 ºC with continuous nitrogen flow for 15 min. All the annealing processes were performed in a furnace. The specific contact resistances (ρ_c) of *p*-type GaN with and without naturally textured surface were measured by circular transmission line model method (CTLM) after evaporation, photolithography process, and alloy was carried out at temperature in the range of 300-900 °C during 15 min in air ambient. For comparison, samples without the aforementioned Mg treatment process were also prepared. The LEDs

without and with Mg treatment *p*-GaN layer are labeled as LED-conv and LED-Mg, respectively.

7.2.3 Measurements and analyses

The wafers were then cut into chips. These chips were thermal treated at 300 and 900 ºC in a furnace under continuous nitrogen flow for 15 min. The current-voltage (*I-V*) characteristics were measured at room temperature with HP-4155 *I-V* analyzer. Room temperature electroluminescence (EL) characteristics were then measured by injecting different amount of DC currents into the fabricated LED chips with package onto TO-can. During the life testing, a part of unannealing chips with TO-can form were stressed by a 50 mA current injection at 25 °C and a relative humidity of 40 %. The SEM surface images were taken with Hitachi S-4000 instrument. For TEM measurements, the specimens were carried out by JEOL JEM-2010 microscope operated at 200 kV.

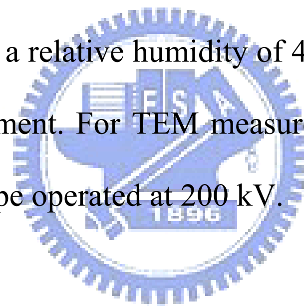

7.3 Results and Discussions

7.3.1 Electrical properties of GaN based LEDs with naturally textured surface after thermal treatment

Figure 7-2 shows the specific contact resistances of samples as a function of annealing temperature. Obviously, an appropriate annealing temperature can reduce the specific contact resistance effectively. Among these data, the ITO contact on *p*-GaN without naturally textured surface present minimum contact resistance of 2.4×10^{-4} Ω cm^2 for the sample annealed at 600 °C. For the ITO contact on *p*-GaN with naturally textured surface, the minimum contact resistance was obtained 1.7×10^{-4} Ω cm^2 after annealed at 500 °C. This

difference for optimum annealing temperature could be attributed to the fact that more surfaces (interfaces) for *p*-GaN with naturally textured surface contact to ITO layer. Figure 7-3 shows the specific contact resistances of Cr/Pt/Au (20 nm/20 nm/2000 nm) contact on *n*-GaN with and without naturally textured surface as a function of annealing temperature. The behavior of both the samples with and without naturally textured surface is very similar up to 800 °C. After annealing above 500 °C, the specific contact resistances were gradual increase. According to results of Fig. 7-2 and 7-3, we found that metals in this case contact on GaN surfaces were thermal unstable not only with naturally textured surface but also without it after annealing above 500 °C. The results show that the new interphases could be formed in the interface between metals and GaN surfaces after annealing higher temperature, and resulted in the contact degradation.

The *I-V* characteristics of the LED-conv and LED-Mg chips after annealing are plotted on a semi-logarithmic scale in Fig. 7-4. In the forward bias region, similar *I-V* characteristics with the ideality factor (n) around 3.1 can be seen for LED-conv and LED-Mg without annealing. In the *I-V* curve of LED-Mg after annealing at 800 and 900 °C, the increases of the parasitic series resistance and higher operating voltage (> 4.6 V) were obtained, which can be attributed to degradation of the TCL ohmic contact on top of the *p*-type GaN. In the reverse bias region, the leakage currents of LED-Mg at reverse biases of 5 V were observed within 1 μA. While the annealing temperature at 800 and 900 ºC, the electrical short circuit behavior can be observed for LED-conv and these LEDs become lightless. Thus, a leakage path may be formed as the annealing temperature increase. However, the LED-Mg annealing at 800 and 900 ºC still showed normal *I-V* characteristic. In the *I-V* curve of LED-Mg annealing at 800 and 900 ºC, the leakage current at -5 V was no variation, and the parasitic series resistance and operating voltage were increase higher than unannealing LEDs. Thus, we considered that the leakage path may be blocked with some barrier.

7.3.2 Electroluminescence characteristics of GaN based LEDs with naturally textured surface after thermal treatment

Figure 7-5 and 7-6 show intensity-current (*L-I*) characteristics of LED-conv and LED-Mg after different annealing temperatures. At low injection currents, it can be seen that the output intensity of these two LEDs increased linearly with the injection current. However, LED output intensities seem to saturate slightly for both devices when the injection current is further increased. According to Fig. 7-5 and 7-6, we also found that LED-Mg (with naturally textured surface) chips can achieve higher saturated current injection (at 350 mA) and LED-conv (without naturally textured surface) chips achieve saturated current injection at 300 mA. Furthermore, LED-Mg can enhance the output intensity by about 30 % than LED-conv at the same current injection. This enhancement can be attributed to the many truncated pyramids on the surface resulting in a wider range of critical angle for internal reflection, and it strongly depends on the surface area occupied by the pyramids.

After thermal treatment, the output intensities were degenerated with increasing annealing temperature. As the temperature increase, the internal quantum efficiency decreases because of reduction of the radiative recombination coefficient and because of the resultant increased overflow of injected carriers from the active layer. These phenomena rapidly decrease the external power efficiency and therefore the output power. The temperature dependence of current-light output power characteristic is determined by several mechanisms. The overflow of the injected carrier is dominant at room temperature and the Auger recombination and intraband absorption are dominant at higher temperatures. The Auger recombination tends to be intensified as the bandgap energy of the active layer decreases. In addition, we also believe that output intensity decay could be attributed to degenerate the hole concentration in *p*-GaN layer after thermal treatment. It is well known that high series resistance in an LED can cause a severe heating effect, giving rise to carrier leakage from the

InGaN active region especially under high current operation. This heating effect will accelerate degradation of electrodes and thereby influence device reliability.

7.3.3 Life tests of GaN based LEDs with naturally textured surface by current injection

Figure 7-7 shows the life tests of reverse leakage current variation (at -5 V) by stressed at 50 mA and 25 °C. The leakage current variation is the ratio (Ir/Ir_0) of leakage current (Ir) to initial leakage current (Ir_0). The initial leakage currents observed from LED-conv and LED-Mg were the same approximately. It was found that leakage current increased rapidly after 168 hours for LED-conv. Small increases of leakage currents for LED-Mg was also obtained after life tests even with a 1008-hour burn-in test. Fig. 7-4 and Fig. 7-7 show that GaN based LEDs without Mg treatment process was unreliable after annealing and a longer burn-in test (stressed by 50 mA). In Fig. 7-8, the life tests of light output variation (at 50 mA) were consistent with the life tests of reverse leakage current. It could be observed that the optical output power was deteriorated by 24.5 % for LED-conv. For LED-Mg, the light output was not obvious variation even with 1000-hour burn-in test.

7.3.4 Microstructure of GaN based LEDs with naturally textured surface

To further understand and confirm the influences of the LED structure, we carried out SEM and TEM studies. Figure 7-9 shows the SEM images of the samples with Mg treatment process (LED-Mg). In Fig. 7-9(a), the LED-Mg exhibits a plurality of truncated pyramids on the surface. Su *et al.* have speculated a possible growth mechanism of the truncated pyramids. [6] In Fig. 7-9(b), the microroughening of *p*-GaN surface was covered with ITO and pad metals completely. After contact metals depositing, the naturally textured surface was still remained to enhance output power.

Figure 7-10 shows the cross-sectional micrograph of the LED structures after annealing at 800 ºC. In Fig. 7-10(a), the structure of the LED with Mg treatment *p*-GaN layer (LED-Mg) was observed clearly, consists of MQW, first *p*-GaN layer, second *p*-GaN layer, and ITO layer (TCL). It was also displayed the structure of truncated pyramid and straight TD. Under higher magnification, as shown in Fig. 7-10(b), the straight TDs should be observed more clearly. In Fig. 7-10(b), there were V-defects present after the MQW growth and these defects were subsequently filled in with first *p*-GaN layer. The V-defects were connected with the TDs from the thick GaN layer at the bottom. In the conventional LED structure (LED-conv), as shown in Fig. 7-10(c), the straight TDs propagates to the free surface. The V-defects are filled with *p*-GaN and direct contact with ITO layer. Compare Fig. 7-10(b) with Fig. 7-10(c), it is clearly indicated that the straight TDs of the LED with Mg treatment *p*-GaN layer can't extend to top surface during growth of the second *p*-GaN layer. Thus, the second *p*-GaN layer prevents the TDs to contact metals layer. In Chapter 6, the NiO layer is used to block the leakage pathway and prevent metals indiffusion along defects or dislocations. According to these results, LED-Mg has good reliability due to the second *p*-GaN layer (the naturally textured surface) prevent the TDs to direct contact metals layer such as the NiO barrier layer.

7.4 Conclusions

The influences of TDs on electrical properties of GaN based LEDs with naturally textured surface have been investigated. For the ITO contact on *p*-GaN with naturally textured surface, the minimum contact resistance was obtained 1.7×10^{-4} Ω cm^2 after annealed at 500 °C. After annealing above 800 ºC, the normal *I-V* characteristic of the LED-Mg still has been observed. The LED-Mg can enhance the output intensity by about 30 % than LED-conv at the same current injection, and achieve higher saturated current injection (at 350 mA). The GaN based LED with Mg treatment *p*-GaN layer (LED-Mg) can achieve good reliability at high

current injection life tests. Both SEM and TEM analyses reveal the structure of truncated pyramid on LED with Mg treatment *p*-GaN layer (LED-Mg) obviously. The TEM images are clearly indicated that the straight TDs of the LED with Mg treatment *p*-GaN layer can't extend to top surface during growth of the second *p*-GaN layer. These results imply evidences that the second *p*-GaN layer (the naturally textured surface) block the leakage pathway and prevent metals indiffusion along defects or dislocations.

7.5 References

[1] J. J. Wierer, D. A. Steigerwald, M. R. Krames, J. J. O'Shea, M. J. Ludowise, G. Christenson, Y. C. Shen, C. Lowery, P. S. Martin, S. Subramanya, W. Gotz, N. F. Gardner, R. S. Kern and S. A. Stockman, Appl. Phys. Lett. **78**, 3379 (2001).

[2] J. V. Smith, "Geometrical and Structural Crystallography", John Wiley & Sons. Inc., (1982).

[3] R. J. Shul, L. Zhang, A. G. Baca, C. G.Willison, J. Han, S. J. Pearton, F. Ren, J. C. Zolper and L. F. Lester, Proc. Material Research Society Symp. **573**, 271(1999).

[4] L. W. Wu, S. J. Chang, Y. K. Su, R. W. Chuang, Y. P. Hsu, C. H. Kuo, W. C. Lai, T. C. Wen, J. M. Tsai and J. K. Sheu, Solid-State Electron. **47**, 2027 (2003).

[5] L. W. Wu, S. J. Chang, Y. K. Su, R. W. Chuang, Y. P. Hsu, C. H. Kuo, W. C. Lai, T. C. Wen, J. M. Tsai and J. K. Sheu, Solid-State Electron. **47**, 2027 (2003).

[6] C. M. Tsai, J. K. Sheu, W. C. Lai, Y. P. Hsu, P. T. Wang, C. T. Kuo, C. W. Kuo, S. J. Chang and Y. K. Su, IEEE Electron Device Lett. **26**, 464 (2005).

[7] T. Margalith, O. Buchinsky, D. A. Cohen, A. C. Abare, M. Hansen, S. P. DenBaars and L. A. Coldren, Appl. Phys. Lett. **74**, 3930 (1999).

[8] R. H. Horng, D. S. Wuu, Y. C. Lien and W. H. Lan, Appl. Phys. Lett. **79**, 2925 (2001).

[9] S. Y. Kim, H. W. Jang and J. L. Lee, Appl. Phys. Lett. **82**, 61 (2003).

[10] C. S. Chang, S. J. Chang, Y. K. Su, Y. Z. Chiou, Y. C. Lin, Y. P. Hsu, S. C. Shei, H. M. Lo, J. C. Ke, S. C. Chen and C. H. Liu, Jpn. J. Appl. Phys. **42**, 3324 (2003).

[11] Y. C. Lin, S. J. Chang, Y. K. Su, C. S. Chang, S. C. Shei, J. C. Ke, H. M. Lo, S. C. Chen and C. W. Kuo, Solid-State Electron. **47**, 1565 (2003).

[12] Y. C. Lin, S. J. Chang, Y. K. Su, C. S. Chang, S. C. Shei, J. C. Ke, H. M. Lo, S. C. Chen, and C. W. Kuo, Solid-State Electron. **47**, 1565 (2003).

[13] S. Nakamura, M. Senoh, S. I. Nagahama, N. Iwasa, T. Yamada, T. Matsushita, Y.

Sugimoto, and H. Kiyoku, Jpn. J. Appl. Phys. **36**, L1059 (1997).

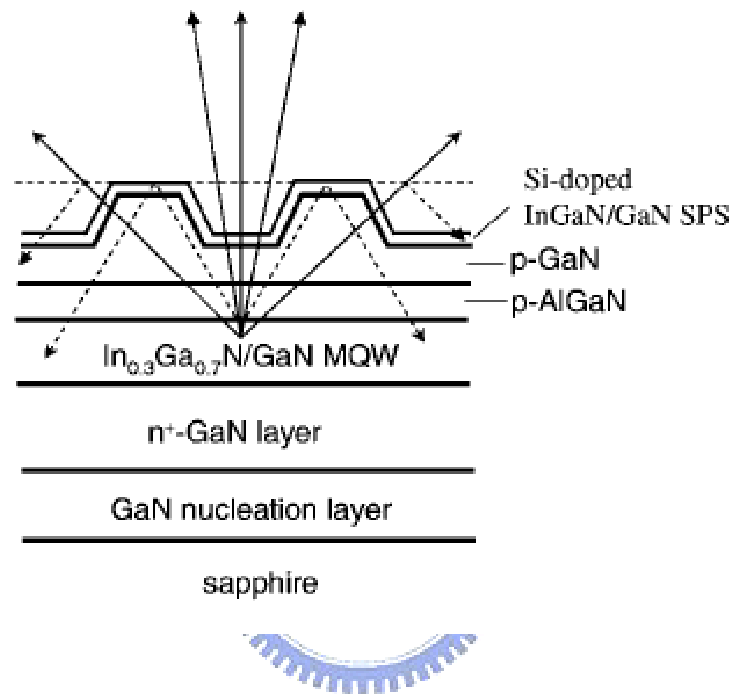

Figure 7-1 Schematic cross-section view of GaN based LEDs with truncated pyramids on the surface. [6]

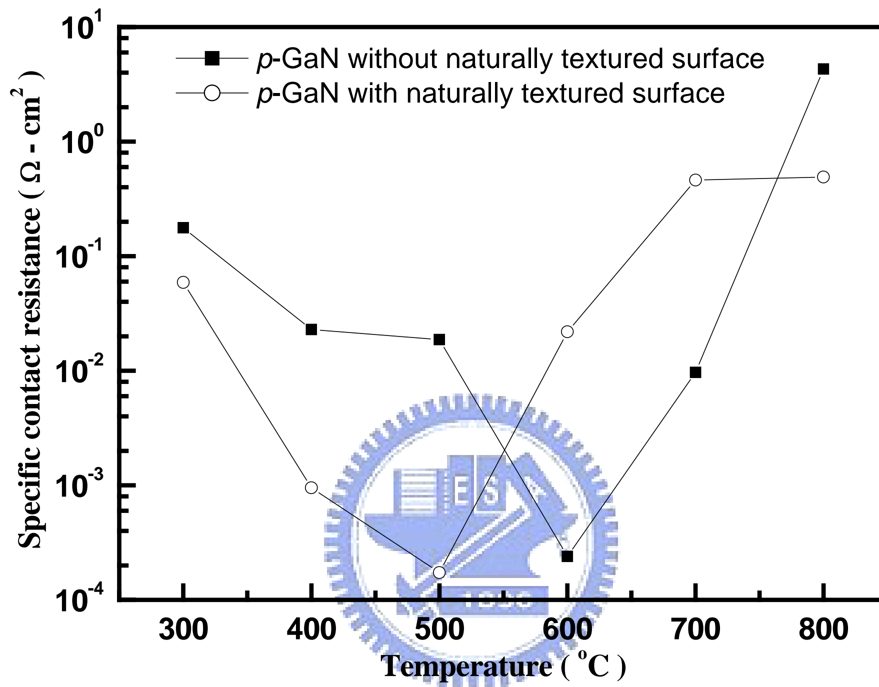

Figure 7-2 The specific contact resistances of *p*-GaN with and without naturally textured surface as a function of annealing temperature.

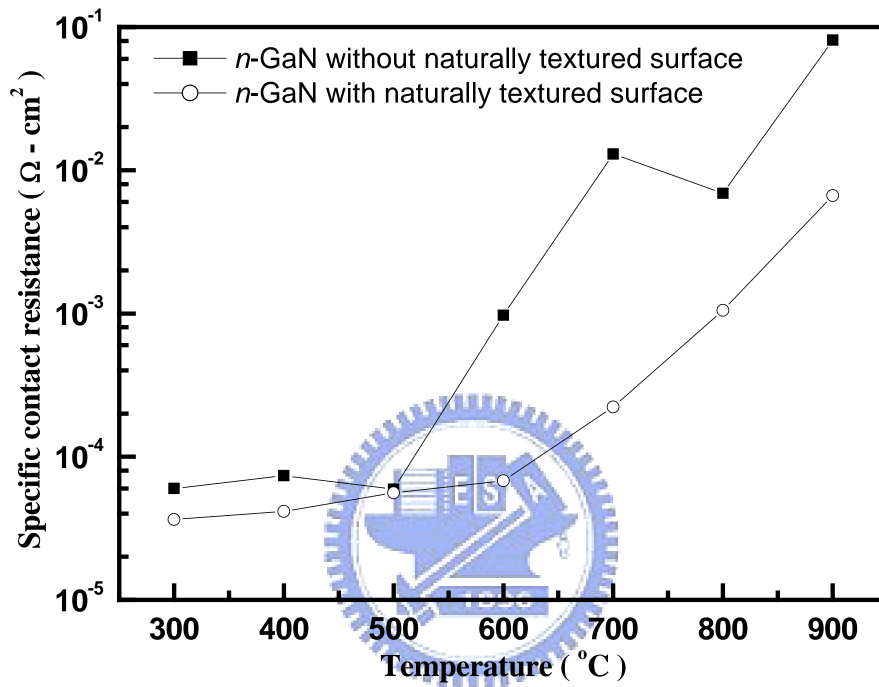

Figure 7-3 The specific contact resistances of *n*-GaN with and without naturally textured surface as a function of annealing temperature.

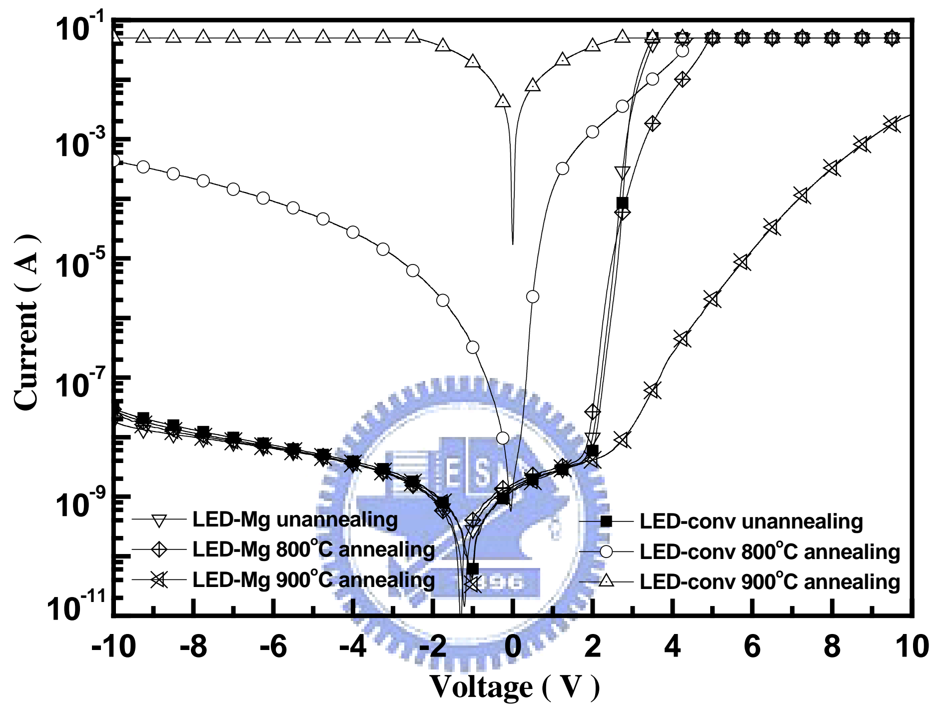

Figure 7-4 The *I-V* characteristics of the LED-conv and LED-Mg chips with different annealing temperatures.

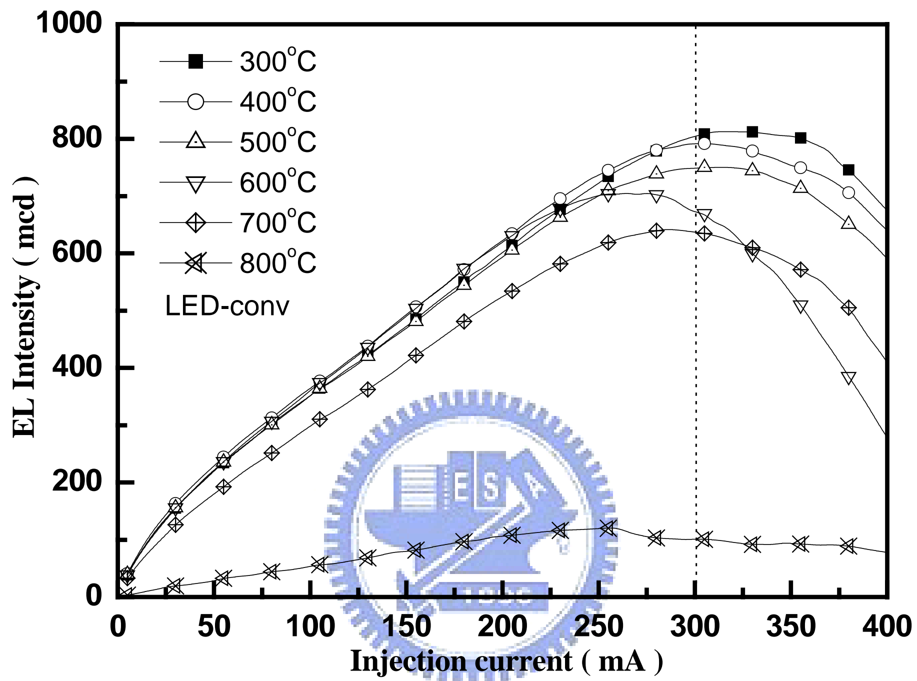

Figure 7-5 *L-I* characteristics of GaN based LEDs without naturally textured surface (LED-conv) after different annealing temperatures.

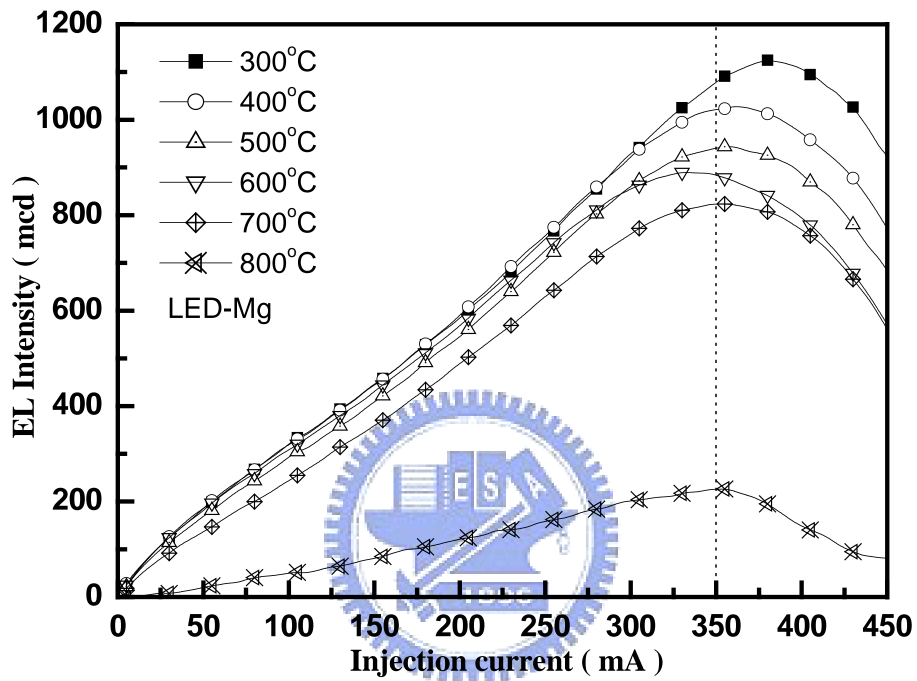

Figure 7-6 *L-I* characteristics of GaN based LEDs with naturally textured surface (LED-Mg) after different annealing temperatures.

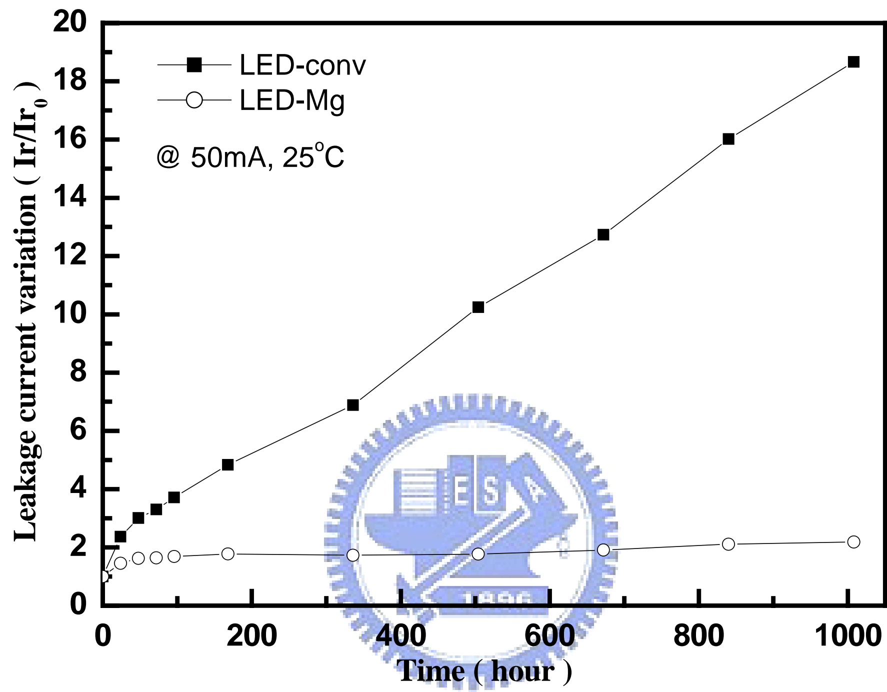

Figure 7-7 Life tests of reverse leakage current variation (at -5 V) by stressed at 50 mA and 25 °C.

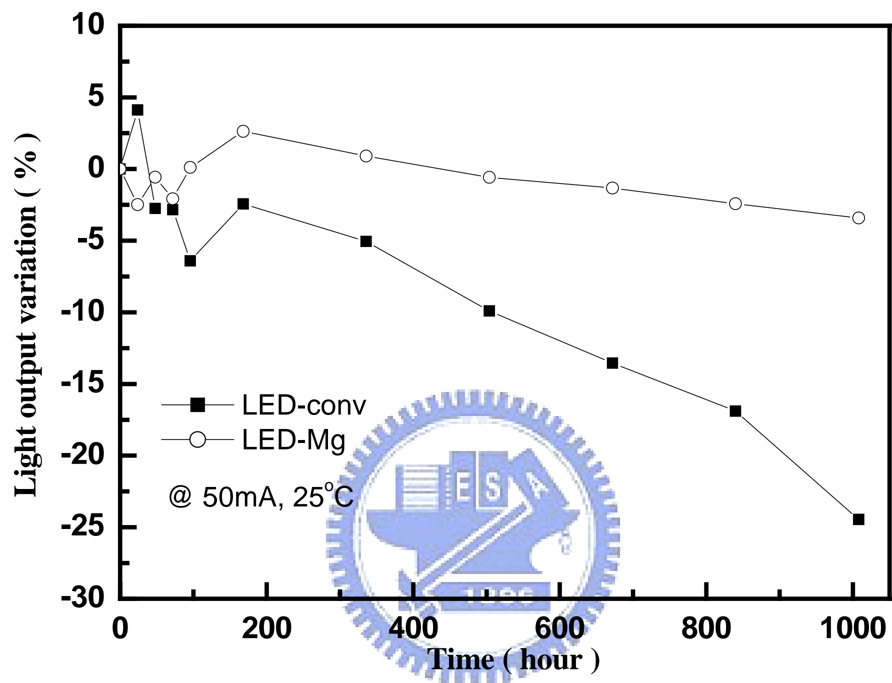

Figure 7-8 Life tests of light output variation by stressed at 50 mA and 25 °C.

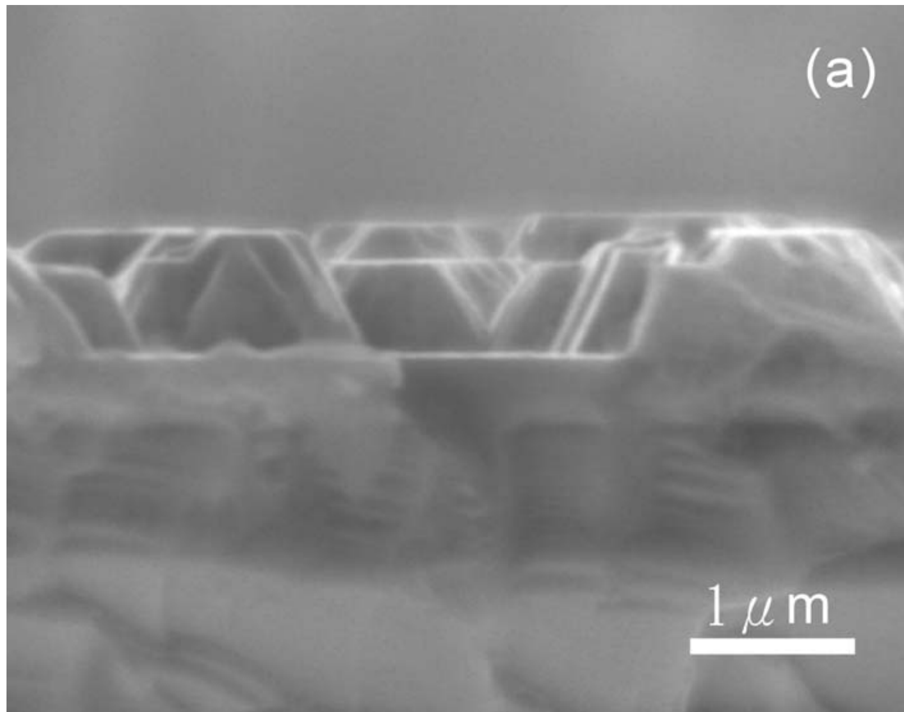

Figure 7-9(a) SEM image of LED-Mg before metals deposition (cross-section).

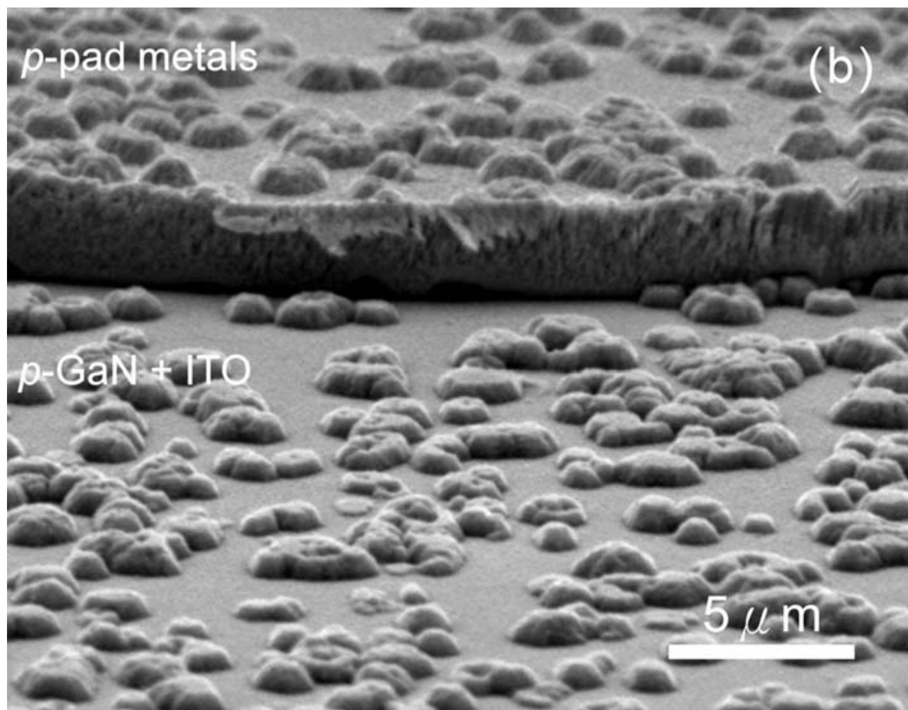

Figure 7-9(b) SEM image of LED-Mg after metals deposition (tilted).

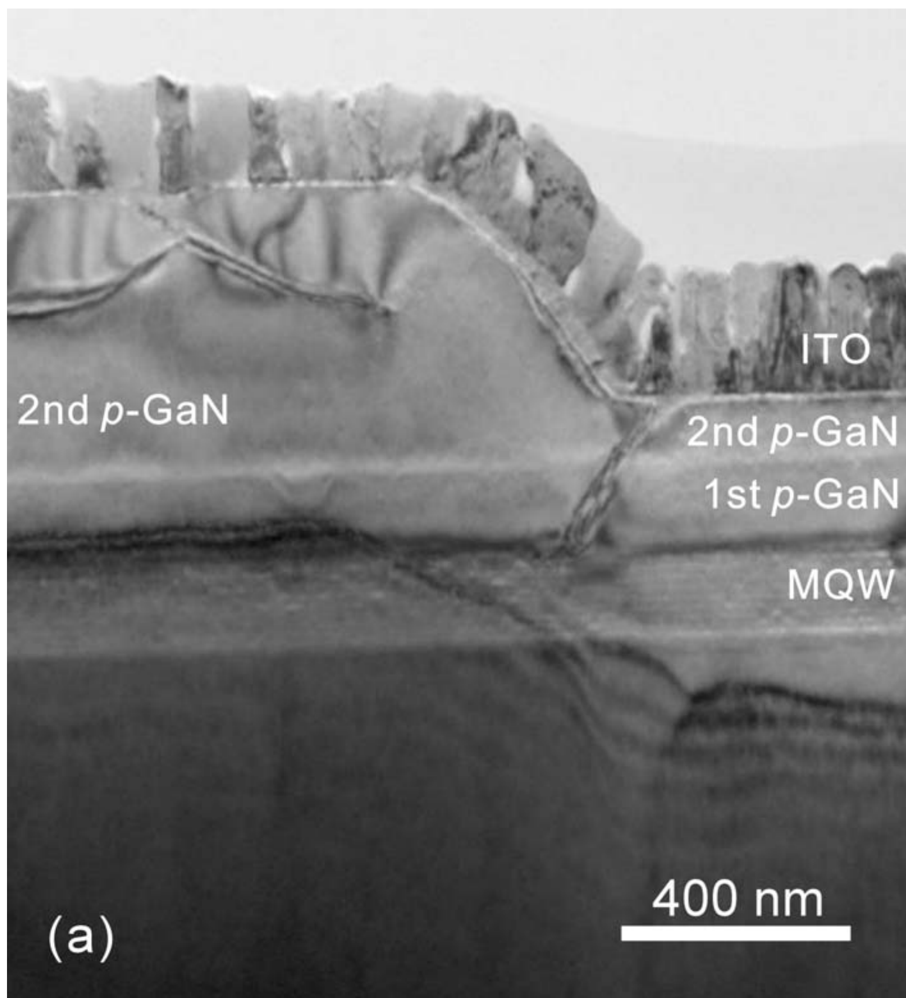

Figure 7-10(a) Cross-section bright-field TEM micrograph of the LED-Mg structure with low magnification image.

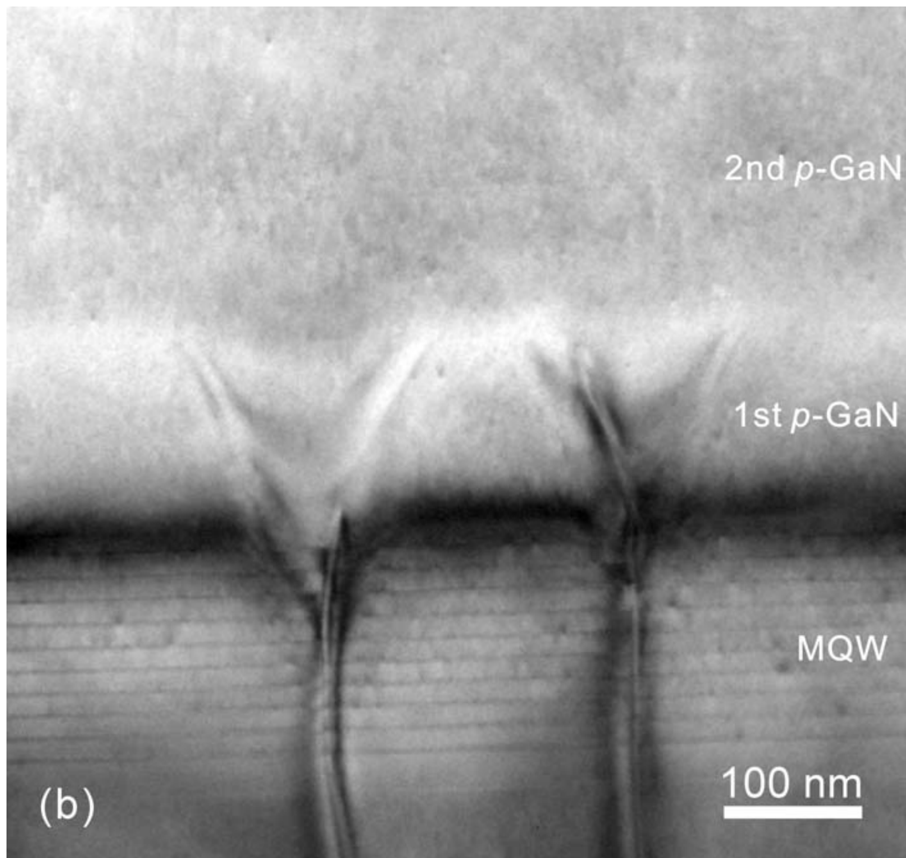

Figure 7-10(b) Cross-section bright-field TEM micrograph of the LED-Mg structure with higher magnification image.

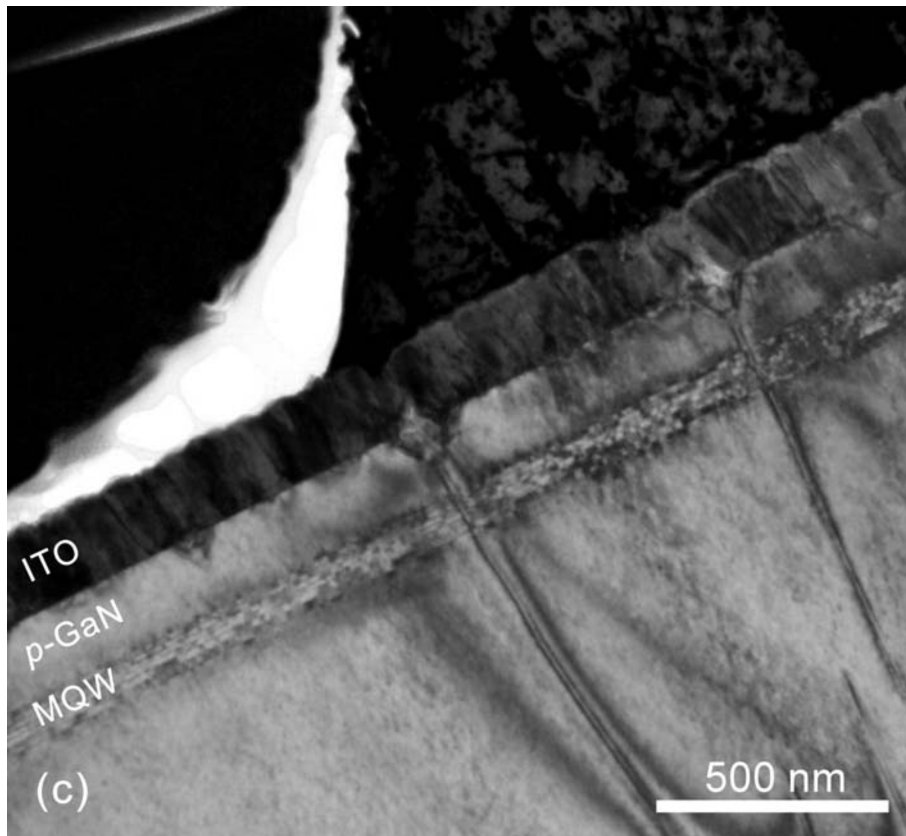

Figure 7-10(c) Cross-section bright-field TEM micrograph of the LED-conv structure.

CHAPTER 8

Conclusions and Future Works

8.1 Conclusions

In this dissertation, we have studied defects and optoelectronic characteristics on GaN based LEDs. The influences of thermal annealing between Ni and *p*-type GaN have been investigated. The samples activated with Ni film obtained higher effective carrier concentrations than activated without Ni film. The effective carrier concentrations as 5×10^{15} cm^{-3} and 1×10^{17} cm^{-3} were achieved at the activating temperature of 400 ºC without and with Ni film. The Ni film may react as a catalyst for activation of Mg-doped GaN with temperature less than 500 ºC. With temperature higher than 600 ºC, the Ni film may react with Mg-doped GaN. The XRD analyses indicated that Ni film on Mg-doped GaN transform to nickel oxide (NiO) and nickel nitride (Ni_3N) during thermal annealing in air. The PL spectra at 15K of the samples activated at 600 ºC with and without Ni film were observed at around 3.2 and 2.9 eV. At high annealing temperature, the impurities such as Ni nitride, nitrogen vacancies or other defects may reduce the hole mobility and provide the increase of the effective carrier concentrations.

The effect of thermal annealing on *I-V* properties of GaN based LEDs with Ni/Au and ITO *p*-type layer have been studied. At annealing temperatures above 700 ºC, the *p-n* junction of the diodes became very leaky and Ga-contained metallic bubbles were observed on the surface of Ni/Au *p*-ohmic contact. TEM and EDS studies revealed that these metallic bubbles resided directly on top of the threading dislocations (TDs) in GaN and both Ni and Au were diffused into the LED structure along the cores of the TDs. According to SEM and EDS analyses, it was also found that indium (In) diffused into the LED structure with defects such

as threading dislocations (TDs) or V-pits. The defects provide leakage paths to cause short circuits in *p-n* junctions at high annealing temperatures. The conducting paths formed by the metal containing dislocation cores are believed to be the cause for the observed short circuit behavior of *p-n* junctions at high annealing temperatures.

We also fabricated GaN based LEDs using transparent ITO-based *p* contacts. The lowest specific contact resistance can be achieved 2.4×10^{-4} Ω cm^2 for 250 nm ITO contact annealing at 600 °C. LED life tests showed that a pure ITO contact layer had poor reliability at high current stress. We also found that the GaN based LED could achieve good reliability with a NiO/ITO contact layer. Using TEM and EDS analyses, we observed In-contained metallic interface between the *p*-GaN layer and the pure ITO contact layer after annealing at 600 °C. It revealed that ITO would react at interface or indiffuse near interface at 600 °C. The LED was degraded with unstable interfaces after life tests (stressed by a 50 mA current injection). While thermal treated at 700 ºC, the LEDs contact with metals became very leaky, and even electrical short circuits have been observed. The original LED wafer could resist heat at higher temperature. From TEM and EDS analyses, metallic V-defect and dislocation core were found after thermal treated at 700 ºC. We suggest that the effect of heat on metals contact is an important factor in GaN-based LEDs, and the defect or dislocation provide leakage paths to cause short circuits in *p-n* junctions at high annealing temperatures. To improve the reliability of GaN-based LEDs with the ITO contact layer, we suggest that the NiO layer be used to prevent the reaction and block the leakage pathway.

GaN based LEDs with naturally textured surface have been grown by metal organic chemical vapor deposition (MOCVD) on c-plane sapphire substrate. We found that the GaN based LED with naturally textured surface could keep normal *I-V* characteristic after high temperature annealing and achieve good reliability at high current injection. Using TEM and SEM analyses, we observed the structure of truncated pyramid on LED with Mg treatment *p*-GaN layer obviously. It is clearly indicated that the straight threading dislocations (TDs) of

the LED with naturally textured surface can't extend to top surface during growth of the second *p*-GaN layer. These results imply evidences that the second *p*-GaN layer (the naturally textured surface) block the leakage pathway and prevent metals indiffusion along defects or dislocations. To improve the reliability and enhance the output intensity of GaN based LEDs, we suggest that the GaN based LEDs can be fabricated with naturally textured surface.

8.2 Future Works

InGaN/GaN based LEDs grown heteroepitaxially on sapphire or SiC substrates contain a high density of threading dislocations (~10^8-10^{10} cm^{-2}) due to large lattice and thermal expansion mismatch between the substrate and III nitrides. It has been found that the high density of dislocations has limited adverse effects on the optical performance of the LEDs, especially at blue and green wavelengths, due to strong carrier localization effects in InGaN alloys. However, the dislocations, particularly those threading through the active region, may have a pronounced influence on the electrical characteristics of the LEDs by enhancing carrier tunneling, dopant diffusion, and contact metal migration. Anomalously high leakage currents are generally observed in commercially available GaN based LEDs, which in many cases are grown on sapphire substrates. The high junction leakage raises concerns about device reliability, particularly under high power operation conditions.

The threading dislocations can be largely eliminated by growing LEDs homoepitaxially on a low defect bulk GaN substrate. As a direct result of better material quality, the LEDs on GaN are expected to exhibit improved electrical characteristics and reliability. The homoepitaxially grown LEDs also benefit from the relatively high thermal conductivity of GaN and simple vertical device geometry, and therefore are suitable for high current operation.

In addition, selective electrical passivation of threading dislocation for the improvement

of contact metals on GaN based LEDs is therefore highly desirable. Passivation techniques suggested so far are based on electrochemical oxidation processes. In our studies (such as chapter 6), the oxide layer can be used to prevent the reaction and block the leakage pathway. Thus, we consider that the passivation technique may provide an efficient improvement to prevent device failure by threading dislocations.